



Gerald Reif, BSc

Model-Based Design of a Vibro-Fluidized Powder Feeder

MASTER'S THESIS

to achieve the university degree of

Diplom-Ingenieur

Master's degree programme: Chemical and Process Engineering

submitted to

Graz University of Technology

Supervisor

Univ.-Prof. Dipl.-Ing. Dr.techn. Johannes Khinast

Ass.Prof. Dipl.-Ing. Dr.techn. Stefan Radl

Institute of Process and Particle Engineering

Graz, December 2014

EIDESSTATTLICHE ERKLÄRUNG

AFFIDAVIT

Ich erkläre an Eides statt, dass ich die vorliegende Arbeit selbstständig verfasst, andere als die angegebenen Quellen/Hilfsmittel nicht benutzt, und die den benutzten Quellen wörtlich und inhaltlich entnommenen Stellen als solche kenntlich gemacht habe. Das in TUGRAZonline hochgeladene Textdokument ist mit der vorliegenden Masterarbeit identisch.

I declare that I have authored this thesis independently, that I have not used other than the declared sources/resources, and that I have explicitly indicated all material which has been quoted either literally or by content from the sources used. The text document uploaded to TUGRAZonline is identical to the present master's thesis.

Datum / Date

Unterschrift / Signature

Copyright © 2014 by Gerald Reif

All rights reserved. No part of the material protected by this copyright notice may be reproduced or utilized in any form or by any means, electronically or mechanically, including photocopying, recording or by any information storage and retrieval system without written permission from the author.

Kurzfassung

Diese Arbeit beschäftigt sich mit den Grundlagen der Pulverdosierung, um die Entwicklung eines neuartigen Dosiergerätes zu ermöglichen. Das Grundkonzept des Dosiergerätes besteht in der Fluidisierung des Pulvers bzw. der Partikel durch Vibrationen. Dadurch soll das Pulver in einen flüssigkeitsähnlichen Zustand versetzt und der Dosiervorgang vereinfacht werden. Die Anwendung von Gesetzen aus dem Bereich der Flüssigkeitsströmungen soll schließlich die Vorhersage bzw. Kontrolle der Ausflussrate ermöglichen. Hierfür, und für diverse andere Untersuchungen wurden Simulationen und Experimente durchgeführt.

Die Untersuchungen werden durch Partikelsimulationen mittels der DEM (Discrete Element Method) durchgeführt, um die Einflüsse wichtiger Simulationsparameter aufzuzeigen, und um die Fluidisierung des Partikelbetts mittels unterschiedlicher Behälterdesigns zu optimieren. Zunächst wurde eine Funktion entwickelt, mit der es möglich ist, die maximale Überlappung, eine wichtige Größe in DEM-Simulationen, in Abhängigkeit von Steifigkeit der Partikel und Vibrationsparametern, vorab zu berechnen. Weiters zeigte sich, dass die Steifigkeit der Partikel, welche die Kontaktzeit der Partikelkollisionen bestimmt und somit im Endeffekt die Simulationsdauer beeinflusst, ein limitierender Faktor bei der Durchführung realitätsnaher Simulationen ist. Substanzielle Einflüsse und Eigenschaften des vibrierten Partikelsystems können aber qualitativ auch mit geringeren Steifigkeiten der Partikel gezeigt werden. So ergaben die Simulationen, dass Behälter mit gezackten Wänden, die das Partikelbett in seichtere, leichter zu fluidisierende Einheiten unterteilen, vorteilhaft sind. Allerdings können bereits kleine Änderungen im Behälterdesign, zum Beispiel im Auslaufbereich, zu Änderungen des Fluidisierungszustands führen. Durch Verminderung der Wandreibung im Behälter kann die Fluidisierung ebenfalls gesteigert werden.

Durch Experimente wurden die Simulationsergebnisse überprüft bzw. komplettiert. Im Wesentlichen wurden mit den Experimenten der Einfluss der Vibrationsbedingungen auf das Ausflussverhalten in Abhängigkeit von der Füllstandshöhe untersucht. Mithilfe einer neudefinierten dimensionslosen Kenngröße *Tor*, wurde anschließend das Ausflussverhalten analysiert. Die Ergebnisse zeigen, dass das Partikelbett während eines Experimentes verschiedene Regimezustände durchlaufen kann, welche die Ausflussrate sprunghaft verändern können. Stabile Ausflussraten können nur für gewisse Füllstandsbereiche unter bestimmten Vibrationsbedingungen erreicht werden. Der Vergleich zwischen den Experimenten und den Simulationen zeigt einmal mehr die Wichtigkeit der Partikelsteifigkeit in den Simulationen auf.

Abstract

This thesis focusses on powder dosing methods in order to lay the foundation for the development of a novel powder dosage device. The concept of the dosing device is the vibro-fluidization of particles or powders to gain fluid like behavior. Investigations using simulations and experiments have been carried out to analyze the discharge rate as a function of the particle filling height and vibration parameters. The effect of the bin design has been studied as well.

By performing particle simulations using the DEM (Discrete Element Method), the effect of important simulation parameters and the possibility of improving the fluidization of the particle bed by making changes in the bin design were investigated. First, a function for predicting the overlap, an important measurement for in DEM simulations, was developed. Furthermore, the particle stiffness, which critically impacts the simulation time, was revealed as a key parameter that affects the discharge behavior. Thus, only qualitative interpretations of the dynamics of the vibrated particle bed could be made by using comparably soft particles. Regarding the bin design, simulations revealed that a bin with jagged walls, i.e., a bin which divides the particle bed into a series of shallow particle compartments, has a positive effect on fluidization. However, even small changes in the outlet geometry can lead to completely different fluidization behavior. A reduction of the particle-wall friction coefficient would also have a positive effect on fluidization.

Experimental investigations focused on the influence of shaking parameters on the fluidization and discharge behavior as a function of the filling height. By analyzing the discharge rates using a dimensionless number, called Tor , different regimes of particle discharge were identified. The results indicate that the particle bed can experience several regime transitions during discharge. These transitions also lead to changes in the discharge rate. Stable, fluid-like discharge rates (i.e., which would be expected for a fluid) are only observed for a limited range of filling height and under specific vibration conditions. Finally, the comparison of experiments and simulations reveals once more the importance of particle stiffness in the simulations.

Acknowledgment

First I would like to thank my supervisors Ass.Prof. Dipl.-Ing. Dr.techn. Stefan Radl and Univ.-Prof. Dipl.-Ing. Dr.techn. Johannes Khinast for giving me the chance to perform such a complex master thesis and for their invaluable guidance throughout this project.

Next, I gratefully acknowledge the support from NAWI Graz by providing access to dcluster.tugraz.at.

In addition, I would like to thank all of my friends and people from the Institute of Particle and Process Engineering who helped me in any respects during the completion of this thesis.

Finally, I am deeply grateful to my parents, my sister and my girlfriend, who have been supporting me for years.

Table of Content

1	Introduction	1
1.1	Goals.....	2
1.2	Outline.....	3
2	Background	4
2.1	Classical Granular Flow Regimes	4
2.2	Vibrated Particle Systems	5
2.2.1	Dimensionless Numbers	5
2.2.2	Regimes of Vibro-Fluidization	6
2.2.3	Deep Beds	7
2.3	Discharge Behaviour of Granular Materials from a Bin.....	10
2.3.1	The Beverloo Correlation	10
2.3.2	Mechanistic Insight	10
2.3.3	Lateral Discharge.....	11
2.3.4	Effect of Vibrations.....	12
3	Theoretical Analysis	13
4	Discrete Element Simulations	15
4.1	Simulation Setup	15
4.2	Effect of Simulation Parameters	16
4.2.1	Stiffness Effect on the Maximum Overlap	16
4.2.2	Stiffness Effect on Discharge Behaviour.....	19
4.2.3	Influence of Wall Friction.....	22
4.3	Segregation.....	23
4.4	Effect of the Orifice.....	24
4.5	Effect of Bin Design	29
4.6	Summary	31
5	Experiments	32

5.1	Setup.....	32
5.2	Experiment I: Orifice at the Bin Bottom.....	32
5.3	Experiment II: Orifice located at $h/d_p \approx 37$	42
5.4	Summary	45
6	Comparison of Simulations and Experiments	46
7	Conclusions and Outlook	48
8	References	51
9	Appendix A - Simulation	54
9.1	Discrete Element Method (DEM) [39,45]	54
9.2	LIGGGHTS Setup.....	56
9.3	Post Processing with Matlab.....	61
10	Appendix B – Experiment.....	77
10.1	Particles	77
10.2	Bin Design	79
10.3	Shaker, Accelerometer and Scales.....	79
10.4	LabVIEW Program.....	84
10.5	Height Measurement.....	87
10.6	Setup and Performing Experiments	87
10.7	Post Processing of Experimental Data.....	88

List of Figures

Figure 1: Phase diagram, a) $r = 2$ [mm], b) $r = 4$ [mm] performed in a quasi-2D container (container length: 101 [mm]) [22].	6
Figure 2: Granular temperature in x (horizontal) and y (vertical) directions plotted over V_b [21].	8
Figure 3: Granular temperature in x (horizontal) and y (vertical) directions plotted over Γ [21].	8
Figure 4: Variation of initial filling height H and observing the expansion height H_E , the height of convection region H_C , the solid layer height H_s and convection strength J under fixed vibration conditions of $f = 40$ [Hz] and $\Gamma = 16$ [26].	9
Figure 5: Qualitative behavior of pressure depending on filling height of in liquids and granular materials [33].	11
Figure 6: Pressure fields during discharge of silo; left: $\mu = 0.32$, middle: $\mu = 0.1$, right: normalized viscosity $\eta = 0.01$.	11
Figure 7: Qualitative plot of different discharge behavior for an inviscid fluid (i.e., “Torricelli-like”), a viscous fluid, as well as granular materials (i.e., “Beverloo-like”).	14
Figure 8: Sketch of the vibrating bin with main dimensions and initial filling height (dimensions are in [mm]).	15
Figure 9: Time averaged maximum overlap over Froude number.	17
Figure 10: Dimensionless overlap over Fr' .	19
Figure 11: Effect of the particle stiffness on the simulation results: Time evolution of a) the total particle mass in the bin (normalized with the total particle mass at $t = 0$), b) the bed height (normalized starting bed height), c) the mass flow (normalized with time-averaged mass flow), d) Tor as a function of bed height, e) the time-averaged pressure (averaging was performed over the first second).	21
Figure 12: Time-averaged pressure profile (averaged of 5 [s]) with and without wall friction (both systems were vibrated at $\Gamma = 5$ and 25 [Hz]).	23
Figure 13: Mean vertical distance of large and small particles (case77: $Y = 7 \cdot 10^8$ [Pa], 25 [Hz], $\Gamma = 5$; case87: $Y = 7 \cdot 10^8$ [Pa], 100 [Hz], $\Gamma = 16$).	24
Figure 14: 5 [s] Averaged pressure profiles plotted over the scaled particle bed height: bin with orifice (61, 62, 63) and without orifice (76, 77, 78).	25

Figure 15: Snapshots of DEM-based simulations (a thin slice near the center of the bin is shown, particles are colored according their force; v^* indicates the current shaking velocity normalized with the maximum velocity, the shaking direction is indicated by the arrow)	26
Figure 16: Snapshots of DEM-based simulations: volume fractions plotted over height in accordance to Figure 15	27
Figure 17: Pressure profiles for bins with (cases 62 and 63) and without (cases 77 and 78) averaged over 0.16 [s].	28
Figure 18: Bin designs used in DEM-based simulations.	29
Figure 19: 5[s] averaged pressure profiles over particle bed height for different bin designs.....	30
Figure 20: Results for experiment I and a vibration frequency of $f = 25$ [Hz].	34
Figure 21: Maximum detachment of the particle bed near the bottom of the bin (left panel), as well as a diffuse top layers (right panel) for two different accelerations and $f = 25$ [Hz] in initial filled bin.	35
Figure 22: Comparison of selected experimental data with fluid-like and Beverloo-like discharge behavior (the dashed line indicates granular behavior, i.e., $Tor \propto 1/\sqrt{h^*}$; the solid line indicates viscous behavior, i.e., $Tor \propto \sqrt{h^*}$).	36
Figure 23: Results for experiment I and a vibration frequency of $f = 50$ [Hz].	37
Figure 24: Results for experiment I and a vibration frequency of $f = 75$ [Hz].	38
Figure 25: Results for experiment I and a vibration frequency of $f = 100$ [Hz].	39
Figure 26: Comparison of the discharge mass (left panel) and bed height (right panel) for a granular material and a fluid (i.e., Torricelli's law).....	40
Figure 27: Overview of the mean dimensionless discharge rates \overline{Tor} , as well as its mean relative error for $0.2 < b^* < 0.9$	41
Figure 28: Bed expansion Δb^* as a function of the dimensionless shaking amplitude r^* for experiment I.	42
Figure 29: Comparison of data from experiments with different orifice position at $f = 25$ [Hz].	43
Figure 30: Comparison of data from experiments with different orifice position at $f = 100$ [Hz].	44

Figure 31: Comparison of results for experiment I with simulation data ($f = 25$ [Hz] and $\Gamma = 5$).	46
Figure 32: Raw height data curves of experiment and simulations: $f=25$ [Hz], $\Gamma = 5$	47
Figure 33: Different bin designs for simulations	56
Figure 34: Particle volume distribution of SiLiBeads S d=1 to 1.3 mm	77
Figure 35: Design drawing of the bin without (left panel) and with (right panel) mounted front and orifice.....	79
Figure 36: a) Shaker with accelerometer mounted to base plate; b) Assembled scales including load cell, RJ50 connector and casing.....	80
Figure 37: Electronic Schematic.....	80
Figure 38: Data sheet TIRA 511120 (http://www.tira-gmbh.de/schwing/_bilder/produkte/schw_er/9n_440n/system_tv_51120_eng.pdf , 2014.05.03)	81
Figure 39: Data sheet accelerometer BDK 100 (http://www.seika.de/english/pdf_e/BD_e.pdf , 2014.03.12)	82
Figure 40: Data sheet load cell PW22C3 (http://www.hbm.com/fileadmin/mediapool/hbmdoc/technical/b1558.pdf , 2014.07.07).....	83
Figure 41: Block Diagram LabVIEW Program	84
Figure 42: Control Terminal of LabVIEW Program for Controlling of the Experiment.....	86
Figure 43: Experimental setup.....	87
Figure 44: Raw data of experiment 8 [g] 50 [Hz]: a) mass data, b) height data.....	94

List of Tables

Table 1: Basic parameters of simulation	16
Table 2: Stiffness investigation: full run simulation parameters	19
Table 3: Simulation settings for the investigation of the effects due to particle stiffness and orifice design.	24
Table 4: Overview of shaking parameters used in experimental runs I with $m_0 = 0.250$ [kg].	33
Table 5: measured particle size distribution and definition of 5 classes for simulations	78

List of Symbols

Latin Symbols

A	area	$[\text{m}^2]$
a	acceleration	$[\text{m s}^{-2}]$
C	constant	$[-]$
d_p	particle diameter	$[\text{m}]$
D	orifice diameter	$[\text{m}]$
f	frequency	$[\text{s}^{-1}]$
F	number of particle layers	$[-]$
Fr	Froude number	$[-]$
Fr'	Froude number describing overlap	$[-]$
g	gravitational acceleration	$[\text{m s}^{-2}]$
h	height	$[\text{m}]$
k	stiffness	$[\text{N/m}]$
l	characteristic length	$[\text{m}]$
\dot{m}	mass rate	$[\text{kg/s}]$
r	amplitude	$[\text{m}]$
S	shaking strength	$[-]$
t	time	$[\text{s}]$
Tor	mass flow rate scaled with Torricelli like mass flow rate	$[-]$
v	velocity	$[\text{m/s}]$
V_b	velocity amplitude	$[-]$
w	bin wall thickness	$[\text{m}]$
Y	Young's modulus	$[\text{Pa}]$

Greek Letters

δ	overlap	$[-]$
Γ	dimensionless acceleration	$[-]$
ρ	density	$[\text{kg/m}^3]$
θ_r	angle of repose	$[\text{°}]$
ϕ	volume fraction	$[-]$
ω	radial frequency	$[\text{s}^{-1}]$

Sub- and Superscripts

<i>b</i>	bulk
<i>c</i>	contact
<i>char</i>	characteristic
<i>DEM</i>	regarding simulation model
<i>h</i>	hydraulic
<i>hydro</i>	hydrostatic
<i>max</i>	maximum
<i>osc</i>	oscillation
<i>p</i>	particle
<i>sim</i>	in simulation
<i>t</i>	time
<i>0</i>	start or standard
*	dimensionless
⊥	cross section of the orifice

1 Introduction

Many industrial applications require the handling of particles and powders. An important and critical step in powder handling operations is powder dosing, especially in the pharmaceutical industry. Exact and reproducible dosage of powder is of major importance, since the potency of active ingredients in pills, or the homogeneity of suspensions like in infusions, is impacted. This is especially true for continuously operated processes [1,2], where inaccurate dosing leads to significant product loss.

Powder dosing devices are based on either volumetric or gravimetric dosing. Volumetric feeders work either with a defined volume (e.g., like in chamber feeders), or a defined particle layer (e.g., on a conveyer belt). Gravimetric feeders are based on measuring the weight with a load cell. Examples of the latter feeder type are ‘loss in weight’-feeders equipped with screws, which measure the incremental change of the powder weight in a bin. In general, gravitational feeders are more expensive due to additional construction costs compared to volumetric feeders, but have a higher dosing accuracy [3].

Clearly, variations in the bulk density of the powder, or undefined flow behaviour (e.g., incomplete filling of the dosing chamber) will lead to an incorrect dosage in case of volumetric feeders. Gravimetric dosage devices correct for these variations in powder properties and flow. However, in extreme situations (e.g., cohesive powder and very small feeding rates) the dosing accuracy of gravimetric feeders can also be unsatisfactory or requires special control strategies [4,5]. Consequently, a more controlled powder density and flow behaviour would positively influence the ability to dose powders in general.

The flow of powder and granular material is distinctively different from that of a fluid: while Torricelli’s equation describes an increasing outflow rate with increasing bin height for fluids [6], Beverloo’s correlation predicts a filling-height independent discharge rate [7]. With respect to the latter, recent studies still debate on the origin of filling-height independent outflow behaviour. Specifically, literature suggests either that (i) the formation of a “free fall hemisphere” [8], or (ii) a change in the local pressure distribution near the orifice [9] leads to this effect. Consequently, the fundamental question: “How can we induce fluid-like discharge behaviour for granular materials?” is still unanswered.

In this work the effect of vibrations on the discharge behaviour of granular material is considered. Specifically, a vibrating powder feeder with lateral (i.e., horizontal) exit is analysed, using both computer simulations and experiments. Our approach is based on vibrations to

fluidize the particles (i.e., to generate a vibro-fluidized bed) in a narrow bin. In general, fluidized particles have a fluid-like behaviour, i.e., the bulk density and the resistance to flow (i.e., the granular viscosity) is expected to be uniform within the bin. Also, a hydrostatic pressure gradient develops in a fluidized particle bed, since wall friction can be significantly reduced. As a consequence, the powder's discharge behaviour is expected to shift to that of a fluid, and the powder dosing operations can be much simplified: for example, Torricelli's relationship for predicting the fluid (or particle) velocity when discharged from a container at a certain distance below the free surface can be used as a design equation. Given a fixed discharge area and bulk density, one could then measure the rate of discharged powder mass by detecting the height of the powder bed above the discharge point.

Despite the simplicity of such an approach, we could not find conclusive data in literature that detail on such an operation principle. Also, we could not find prior work that has analysed the effect of vibrations on the discharge behaviour for our bin design.

1.1 Goals

The design of the vibro-fluidized powder feeder investigated in this work relies on the idea of a known relationship between the powder height and the rate of mass discharge from a bin. The key challenge is, however, to induce fluid-like behaviour of the powder by means of vibrations, as well as to ensure a constant bulk density directly at the powder outlet. Hence, our first goal is to quantitatively understand how vibrations influence the stress distribution in a powder and its flowability. We approach this challenge by performing soft-sphere simulations using the discrete element method (DEM). These simulations allow us to measure the stress and particle volume fraction distribution in the bin which is used as the dosing device. Also, we aim on critically assessing the effect of finite particle stiffness, i.e., we search for a relationship between the dimensionless overlap of particles and the simulation parameters.

The second goal is to support our simulation data with corresponding experimental data. Specifically, we have measured the rate of mass discharge under various vibration conditions. The challenge is to measure the discharge rate in a time-resolved manner, for which we have designed a novel system consisting of a balance and dedicated post processing software.

Our third goal is to identify optimal process conditions in which the powder behaves like a fluid, i.e., its discharge velocity depends only on the filling height. In order to discriminate

between constant outflow behaviour (typical for granular materials) and the desired fluid-like discharge behaviour, results were normalized with the (hypothetical) Torricelli discharge rate.

1.2 Outline

In Chapter 2 we discuss recent studies dealing with flow regimes and discharge behaviour specific for vibrated granular matter. Chapter 3 describes the definition of the dimensionless number Tor , used for the characterisation of different discharge behaviours of granular material. Chapter 4 deals with the DEM-based simulations with a focus on the effect of the particles' stiffness, friction coefficient and investigations on the bin design. In Chapter 5 experimental results are presented: the discharge rates and the corresponding height of the powder bed are measured as a function of the vibration settings and bin design. Also, the dilatation of the powder bed is examined, and conditions under which a sufficient fluidization of the powder bed are identified. Finally, simulation and experimental results are compared in Chapter 6, and conclusions are summarized in Chapter 7.

2 Background

2.1 Classical Granular Flow Regimes

The flow behaviour of granular materials, unlike that of fluids, depends on (i) the particle characteristics (e.g., size or shape), (ii) the state of fluidization (with a gas or vibrations), and (iii) the size of the container the particles are in. With respect to the latter, the typical relative size (compared to the particle diameter) is the key parameter that determines the system behaviour, e.g., the scattering pattern of a granular jet [14]. Another key difference to fluids is that granular materials are able to develop a shear stress at zero flow. Because of this, the quantitative description of the rheology of granular material is significantly more involved, and only recently regime maps (for simple shear flow) have been proposed [10,11]. Chialvo et al. [12], for example, differentiate an inertial (i.e., gas-like), an intermediate (i.e., liquid like), and a quasi-static (i.e., solid-like) regime by using a dimensionless shear rate and the particle volume fraction. This description is compatible with earlier work that was based on an inertial number [13].

In the case of silo or bin discharge, all three granular flow regimes occur [15], and DEM-based simulations have been used in the past to describe these flows [16]. The effect of the interstitial gas becomes important for particles with a diameter of less than ca. 500 μm , and can be quantified using a characteristic Stokes number (see our discussion in Section 2.3). In the current work we have not analyzed effects due to the interstitial gas, and have also not explored the possibility to fluidize the particles in the bin by means of a continuous or pulsated air stream [17]. Despite the latter has been successfully employed to induce the formation of regular fluidization patterns [18], segregation and elutriation of fines will prohibit the use of fluidized beds for powder dosing devices.

We now focus on vibro-fluidization in the following paragraphs. In vibrated systems energy is injected into the granular material such that its granular temperature increases, i.e., the system is “thermalized”. Thus, one expects that this leads to a shift in the flow regime to that of a liquid or a gas. However, vibrations may lead to phenomena like spontaneous heaping and pattern formation, which are difficult to predict quantitatively [19]. Next, we review findings of relevant phenomena, and how they have been described in the past.

2.2 Vibrated Particle Systems

A number of investigations on vibrated granular matter have been performed, most of them focusing on a particular phenomenon. Segregation due to different particle size is one of them, and might play a role in polydisperse systems as reviewed by Kudrolli [20]. In this study we focus on systems with a narrow size distribution, and hence are only concerned with monodisperse (or slightly polydisperse) materials. This greatly simplifies the description of vibrated particle systems, for which we now introduce the key dimensionless quantities.

2.2.1 Dimensionless Numbers

Vibrations can be described in general by their frequency f and their amplitude r . Hence, a (dimensional) acceleration a and radial frequency ω can be calculated from [21]:

$$\omega = 2\pi f \quad 2.1$$

$$a = r\omega^2. \quad 2.2$$

For the investigation of vibrated particle beds, a Froude Number, i.e., the ratio of the kinetic energy injected into the system and the potential energy due to a typical displacement l of the particles, has been used [22]:

$$Fr = \frac{r^2\omega^2}{gl}. \quad 2.3$$

For mild vibrations the particles follow the movement of the shaker. It is then appropriate to choose the amplitude r as a typical displacement length l . The Froude number is then denoted as dimensionless acceleration Γ , which can be interpreted as the ratio of the applied shaker acceleration a and the gravitational acceleration [21,22]:

$$\Gamma = \frac{a}{g}. \quad 2.4$$

Since it is rather difficult to find a representative value for the displacement l for higher vibrational strengths, one can use the particle diameter d_p as typical displacement length. The resulting dimensionless number is then denoted as the shaking strength S [22]:

$$S = \frac{r^2 \omega^2}{g d_p} \quad 2.5$$

Often, the square root of S is used, which can be interpreted as the ratio of a maximum oscillation velocity ($r\omega$) and a characteristic particle velocity $(g d_p)^{1/2}$. This quantity is denoted as the dimensionless velocity amplitude V_b : [21]

$$V_b = \sqrt{S} = \frac{r\omega}{\sqrt{g d_p}} \quad 2.6$$

2.2.2 Regimes of Vibro-Fluidization

In vibrated particle beds different regimes occur which can be classified with the dimensionless numbers described in the last section. In the present work, the focus is on systems with particles having a diameter larger than 1 [mm], i.e., effects due to the interstitial gas (i.e., air) are absent [20].

Depending on the vibrational motion (characterized with Γ or S) and the dimensionless bed height F (i.e., the bed height divided by the particle diameter), Eshuis et al. [22] observed a variety of regime transitions in a quasi 2D particle bed (see Figure 1).

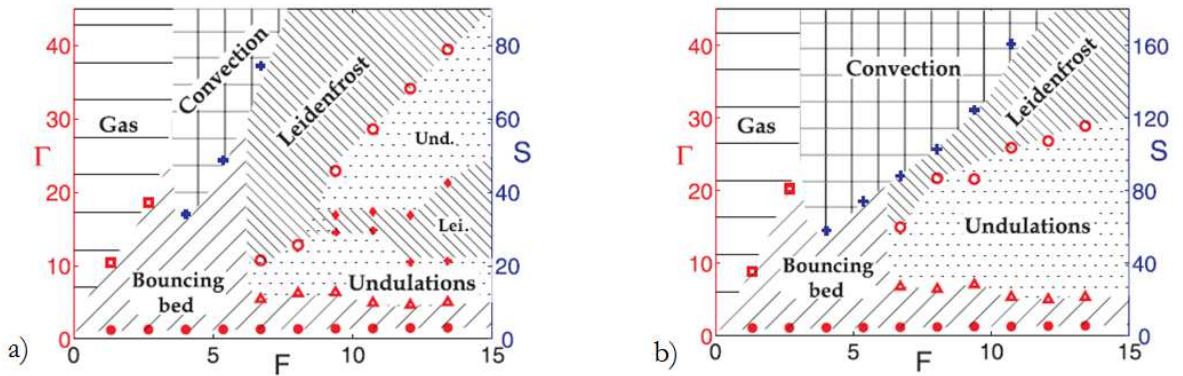


Figure 1: Phase diagram, a) $r = 2$ [mm], b) $r = 4$ [mm] performed in a quasi-2D container (container length: 101 [mm]) [22].

Their experiments reveal a “bouncing bed” regime at comparably low accelerations and all values for F . In this regime the particle bed detaches from the bottom of the bin (i.e., mild fluidization). Depending on the number of particle layers, different regimes are entered when further increasing the dimensionless acceleration: for a larger value of F (i.e., a deeper bed), undulations are observed. These are standing waves that oscillate with half of the shaking

frequency f and consist of a specific number of arches. The higher Γ , the higher the number of arches [22]. With increasing acceleration the undulations become more and more unstable and enter the region of the Leidenfrost state. This state is the granular equivalent to the phenomena of hovering liquid droplets on a hot surface: at the bottom of the container a region with fast moving particles, replicating the gaseous phase a fluid system, is formed. On this (granular) gas phase a dense cloud of particles is floating. The Leidenfrost state and the undulation state are indicating an intermediate type of fluidization [22].

In case the energy injected through the bin bottom increases further (i.e., $S >$ approximately 30), it is possible for some particles to break through the particle bed of the bouncing bed and trigger coherent particle motion, i.e., a convective flow cell. These cells are initiated near the vertical sidewalls, and manifest in a downward motion of particles near the walls because of a higher local dissipation due to particle friction at the walls. The higher the injected energy, the bigger are the convection cells and the fewer of them can be observed [23]. These convection cells can also be observed in fluids that are heated at the bottom (i.e., Rayleigh-Bénard convection [24]). The experiments of Eshuis et al. [22] revealed a gaseous fluidization regime of the particle bed only for a dimensionless bed height smaller than Γ . The collisions in this regime are likely to involve only two particles (i.e. binary collisions), and are nearly instantaneous (i.e., in the mean free time is much larger than the duration of a single collision [22,25]).

The results of Eshuis et al. [22] suggest that neither Γ nor S , but only a combination of both parameters is sufficient to describe the behaviour of the bed: as described in the previous section, Γ and S are essentially Froude numbers, using either r or d_p as typical length scales. As long as the particle bed follows more or less the vibrational motion (i.e., $\Gamma < 10$ resulting in a “mild” fluidization), Γ is the key dimensionless parameter. In contrast, for the transition to the convective regime, S is the representative parameter (i.e., “strong” fluidization). In the intermediate fluidized regime (i.e. undulations and Leidenfrost state) a competition of length scales takes place, and two dimensionless parameters (e.g., Γ and S) are needed to predict the transition. It should be noted that other parameters like, e.g., container size, and material properties have a big influence on the dynamics of the system [22].

2.2.3 Deep Beds

Deep vibro-fluidized beds, i.e., with a dimensionless bed height F bigger than about 20, are of more practical relevance, and have been studied, e.g., by Tai and Hsiau [21]. Using image

processing technology and particle tracking, the latter authors investigated various transport properties in the regime where convection cells form. The formation of the convection cells at low Γ is observed in the top region near the walls, and the cells occupy only a small region of the particle bed. This indicates that the top regions in the particle bed get easier fluidized compared to the bottom regions. This is due to the fact that the pressure is increasing with increasing distance from the free surface. As mentioned in the previous section above, V_b (or S) are better parameters for describing this regime, since $\Gamma > 15$ to induce the formation of the convection cells [22]. The convection cell becomes bigger in size with increasing V_b , and finally takes up the whole container. This state is interpreted as a “fully vibro-fluidized bed”. It turns out that the transition to a fully vibro-fluidized bed occurs at $V_b \approx 2$ for a certain initial bed height, as detected by measurements of the granular temperature (see Figure 2 and Figure 3, [21]).

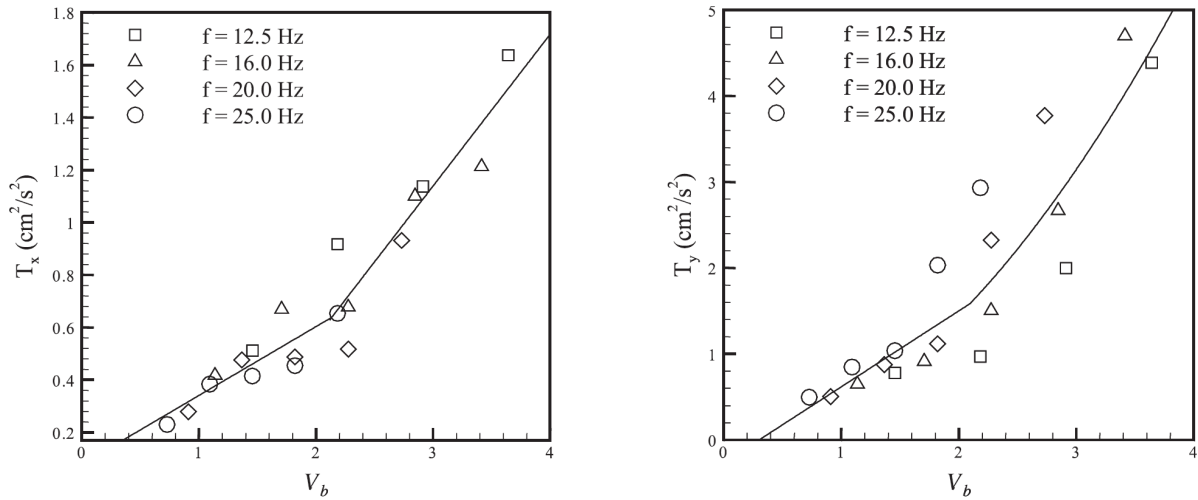


Figure 2: Granular temperature in x (horizontal) and y (vertical) directions plotted over V_b [21].

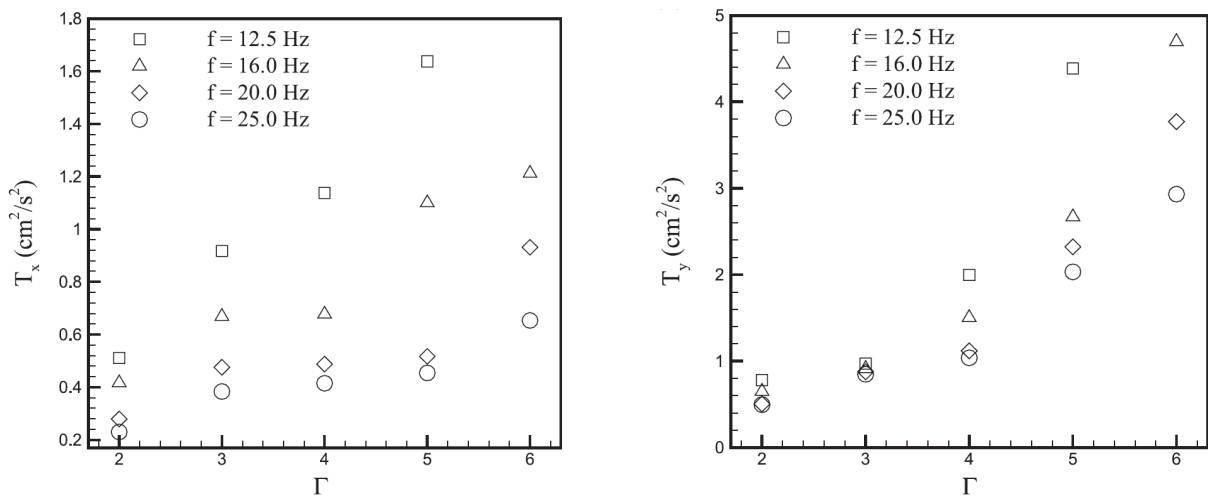


Figure 3: Granular temperature in x (horizontal) and y (vertical) directions plotted over Γ [21].

In addition, Tai and Hsiau [21] observed an anisotropy of the granular temperature, i.e., vertical velocity fluctuations were reported to be stronger than that in the horizontal direction. Furthermore, the granular temperature is increasing with increasing Γ or decreasing f (at $\Gamma = \text{const.}$). This is because the energy input of the shaker scales with the amplitude r , and hence for $\Gamma = \text{const.}$, $r \propto 1/f^2$.

Subsequent studies performed by Hsiau et al. [26] reveal the influence of the initial bed height on quasi 2D vibro-fluidized beds. In their experiments (using fixed values for f and Γ) they investigated the height of the convection cells as a function of the initial bed height (see Figure 4; heights were normalized with the particle diameter). It was observed that starting from a height of a fully fluidized bed, where the height of the convection cell H_C takes up the whole bed height H_E , a maximum level of fluidization is obtained at a dimensionless initial bed height of $H = 45$. This maximum level of fluidization corresponds to the maximal (dimensionless) convective flow J , which is a parameter for the strength of the convection cells. Note that the granular temperature would qualitatively show the same behavior as J . For the case of $H > 45$ a solid-like particle layer with height H_S is formed beneath the convection cell. This layer is taking up more and more of the particle bed when increasing H , i.e., H_C as well as the fraction of particles that are fluidized decreases. This is because more energy dissipation occurs in the solid layer, and a lower amount of vibrational energy and is received by the convection region causing a decrease of. For $H > 70$ the solid layer further increases, and the trends show a slightly more complex behavior [26].

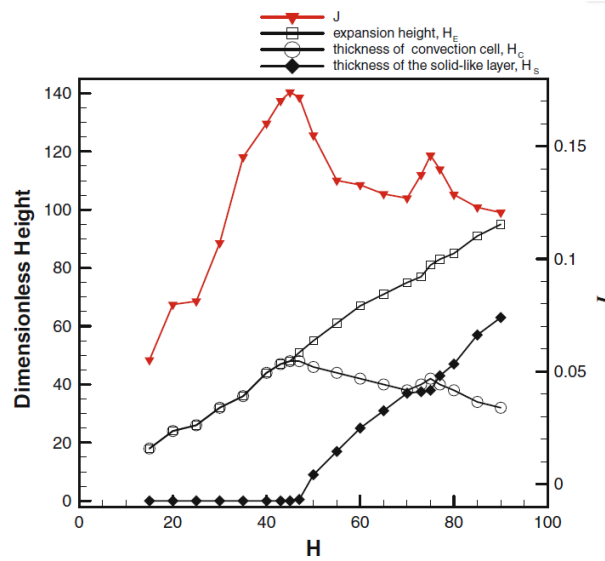


Figure 4: Variation of initial filling height H and observing the expansion height H_E , the height of convection region H_C , the solid layer height H_S and convection strength J under fixed vibration conditions of $f = 40$ [Hz] and $\Gamma = 16$ [26].

2.3 Discharge Behaviour of Granular Materials from a Bin

2.3.1 The Beverloo Correlation

Classical investigations of freely discharging granular materials from silos under the action of gravity, but in absence of vibrations, date back to the work of Hagen in 1852 [27]. Hagen correlated that the mass flow \dot{m}_0 of a dry granular material emerging from a circular bottom exit of silo using $\dot{m}_0 \propto \rho_b g^{1/2} D_0^{5/2}$. Here ρ_b is the bulk density, g is the gravitational acceleration and D_0 is the orifice diameter (or the hydraulic diameter in case of a non-circular orifice [28]). Beverloo et al. [7] improved this relationship by introducing a reduced orifice diameter D_B , arriving at:

$$\dot{m}_0 = C \rho_b \sqrt{D_B^5 g} \quad \text{with} \quad D_B = D_0 - k d_p. \quad 2.7$$

The orifice diameter is reduced due to the fact that particles with diameter d_p near the orifice form a stable hemisphere, and reduce the effective diameter of the orifice. C and k are parameters, which depend on the bulk density, as well as particle and silo/hopper properties. Typically, these parameters need to be determined experimentally for a certain granular system. For monodisperse dry particle in a silo, typical values are $C \approx 0.55 - 0.65$ and $k \approx 1 - 2$ [7]. Eqn. 2.7 predicts the discharge rate quite well if $D_0 > 5d_p$ and if either $d_p > 0.5$ [mm] (i.e. no interstitial gas effects) or/and the bin has got an open top [28]. For applications where $D_0 < 5d_p$, jamming events during the discharge are likely to occur, causing erratic behaviour [29]. Also, the Beverloo correlation is not accurate over a wide span of D_0 (i.e., a relative error of 10% has to be accepted when increasing D_0 by two orders of magnitude [29]).

2.3.2 Mechanistic Insight

According to Eqn. 2.7, the outflow rate of the granular matter is independent of the filling height of the silo. Earlier studies assumed that the flow rate through an orifice depends on the pressure, and hence Janssen's equation was identified as the origin of this behaviour [27,30] (see Figure 5). However, recent studies revealed that the discharge rate of particles is constant is due to local conditions in the vicinity of the outlet [9,31,32]. Specifically, the empiricism-based Beverloo correlation can be explained physically by considering the behaviour of grains near the orifice: under the assumption of a "free fall hemisphere" near the orifice, and by

integrating over the velocity of the discharging particles, the scaling of the exit flow rate with $\sqrt{D_B^5 g}$ can be shown [8].

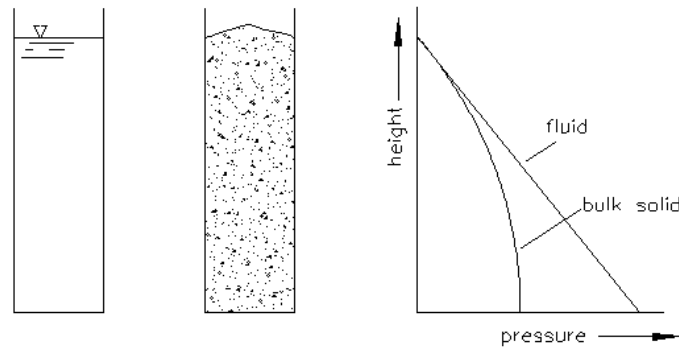


Figure 5: Qualitative behavior of pressure depending on filling height of in liquids and granular materials [33].

The assumption of a “free fall hemisphere” is clearly a strong simplification, since it does not explain how particles enter this hypothetical hemisphere, or what is the effect of inter-particle friction and vibrations on the discharge behaviour. More conclusive arguments are provided by Staron et al. [9], which investigated the discharge behaviour and how it is effected by inter-particle friction. By using a continuum model of granular flow, they show the transition from filling-height independent to fluid-like behaviour (see Figure 6). A region of low pressure above the orifice is identified as the origin of constant discharge. This suggests that the lateral pressure distribution is of key importance, explaining previous difficulties to identify the reason for constant outflow behaviour based on experimental data.

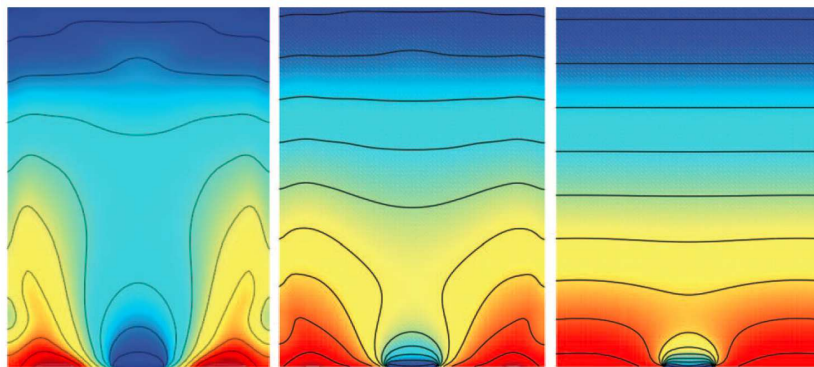


Figure 6: Pressure fields during discharge of silo; left: $\mu=0.32$, middle: $\mu=0.1$, right: normalized viscosity $\eta=0.01$.

2.3.3 Lateral Discharge

For the present study the flow of granular material through lateral orifices is more relevant, since we aim on a powder feeder with a horizontal exit. Compared to investigations of orifices at the bottom of the bin (as discussed in the last paragraphs), much less work has been done

for lateral discharge. Sheldon et al. [34] investigated the discharge rate of a bin in several tilted positions (i.e., a horizontal, a vertical, and a position with no discharge at all) and reported a discharge rate similar to what one would expect from the Beverloo correlation. In contrast, Bagrintsev and Koshkovskii [35] concluded from studies on the outflow through vertical holes that $\dot{m}_0 \propto \rho_b g^{1/2} D_0^{7/2}$. This discrepancy could be clarified by Medina et al. [28] performing experiments on lateral discharges with different wall thicknesses w . Specifically, they suggested

$$\dot{m} = C_l \rho_b g^{1/2} D_B^{5/2} \left[\frac{D_0}{w} - \theta_r + O(D_0^3 / w^3) \right], \quad 2.8$$

where \dot{m} is the mass flow through a lateral outlet, C' is a constant, \dot{m}_0 is the outflow through a orifice at the bottom as predicted by Eqn. 2.7, w denotes the wall thickness, and θ_r is the angle of repose. Note, that this equation only holds for thick walls, i.e., $D_0/w > \theta_r$, while for thin walls the discharge rates scales with $\dot{m}_0 \propto \rho_b g^{1/2} D_0^{5/2}$.

2.3.4 Effect of Vibrations

Discharge of vertically-vibrated granular material from a hopper (with a orifice at the bottom) was investigated by Wassgren et al. [36]. Besides the development of reversed convection cells compared to straight bins, the observed discharge rates were successfully scaled with the vibration velocity amplitude and the acceleration amplitude. Another work done by Pacheco-Martinez et al. [37], using horizontally-vibrated walls with a orifice at the bottom, revealed that a completely fluidized particle bed (without discharge) can be achieved as indicated by a linear pressure profile. However, by opening the orifice to start the discharge, the Janssen's effect is re-established immediately and the hydrostatic condition is lost. Pacheco-Martinez et al. [37] showed that it requires intense vibration conditions to retain the fully fluidized state under discharge conditions. Also, Torricelli-like discharge behaviour was observed at higher vibrational strength, and wall friction was not affecting the discharge rate. Most important, Pacheco-Martinez et al. [37] concluded that the discharge rate scales with the induced shear rate. This indicates that fluid-like behaviour of a granular material upon discharge can be realized. In our work we will further investigate exactly this transition to a fluid-like behaviour at high vibrational accelerations.

3 Theoretical Analysis

In order to analyse our data in a meaningful way, we first introduce a dimensionless parameter for the discharge rate. We do this by defining the dimensionless quantity Tor , which is the ratio of the measured discharge rate and a hypothetical discharge rate assuming inviscid fluid flow, i.e., $Tor = \dot{m} / \dot{m}_{inv}$. The latter is based on Torricelli's law, and the mean bulk density in the bin:

$$\dot{m}_{inv} = \rho_b A_{\perp} \sqrt{2gh}, \text{ with} \quad 3.1$$

$$\rho_b = \frac{m_0}{A_{bin} h_0}. \quad 3.2$$

Here \dot{m} is the discharge rate in [kg/s], ρ_b is the bulk density in [kg/m³], A_{\perp} is the cross-sectional area of the orifice in [m²], A_{bin} is the cross-sectional area of the bin in [m²], m_0 is the total mass of particles in the bin in [kg], g is the gravitational acceleration, h_0 is the initial height of the dilated bed, and h is the current particle bed height in [m]. Note, that h_0 is different from the height h_{fill} of the particle bed after filling, which is used to define the expansion of the bed (see the end of this Section).

Tor can be interpreted as a dimensionless fluidity of the discharged material. Clearly, Tor would be a constant for fluid-like discharge behaviour, i.e., $Tor = 1$ for an ideal (i.e., inviscid) fluid. In contrast, a constant dimensional discharge rate typical for granular materials would be reflected by $Tor \propto 1/\sqrt{h}$, i.e., an increase of Tor with decreasing h . At this point it is important to note, that it has to be known *a priori* whether the bed is fluidized or not when analysing the results for Tor vs. h : this is because an increase of Tor with decreasing bed height can be caused by (i) ‘‘classical’’ granular discharge behaviour, or (ii) an increase of the level of fluidization. For the latter, the value for Tor directly indicates how well fluidized the particle bed is, and how close the mean bulk density approximates the true bulk density in the orifice.

In case one assumes that the discharge rate is also influenced by an effective viscosity of the granular material, one can estimate the discharge rate under the assumption of a constant viscosity and bulk density [38]. In the limit of high viscosity, and when neglecting the kinetic energy of discharged particles, the velocity of discharged particles scales linearly with the bed

height, and hence $Tor \propto \sqrt{h}$. We have used this result in order to interpret experimental data that showed an increase of Tor with bed height for shallow beds.

Figure 7 qualitatively compares the discharge behaviour for (i) a granular material as given by the Beverloo equation, (ii) for an inviscid fluid (Torricelli), as well as (iii) that of a highly-viscous fluid. Note that the time scale used in Figure 7 is normalized with a factor considering geometric relations as well as initial filling height and discharge velocity at discharge start. Clearly, the discharge characteristics shown in Figure 7 are useful for the interpretation of regime changes during bin discharge.

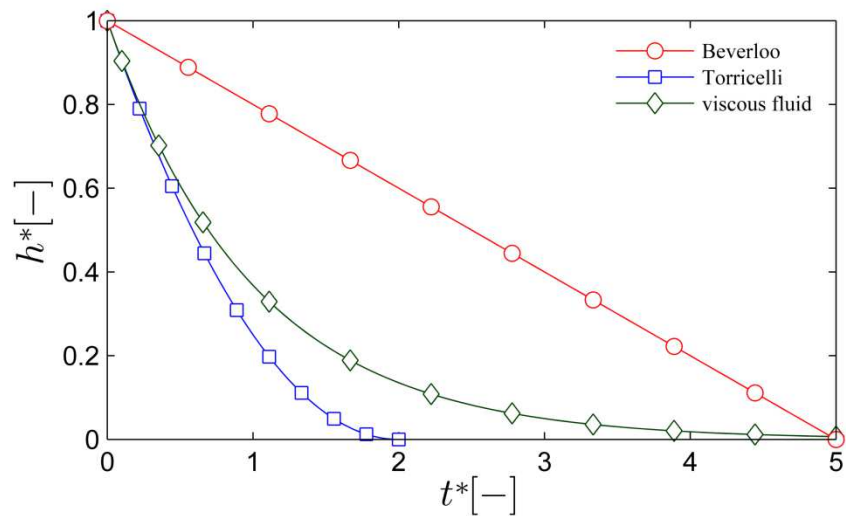


Figure 7: Qualitative plot of different discharge behavior for an inviscid fluid (i.e., “Torricelli-like”), a viscous fluid, as well as granular materials (i.e., “Beverloo-like”).

4 Discrete Element Simulations

4.1 Simulation Setup

The simulations are carried out with the software package LIGGGHTS-TUG (Version 3.0.2.), which is based on the open-source package “LIGGGHTS” developed by Kloss et al. [39]. For all simulations we have employed the widely accepted linear spring-dashpot model [40].

The base case consists of a vibrating bin as described in Figure 8 (also see Appendix: Section 10.2). Particles are considered to be slightly polydisperse, i.e., the particle size distribution was discretized into five classes (see Appendix, Section 10.1). The distribution was matched with that of the particles used in the experiments, and showed only a minimal tendency to segregate (see Section 4.3 for details). In our standard configuration 0.350 [kg] of the granular material (approximately 151,000 particles) have been used. Key physical parameters for the PMMA/glass system are provided in Table 1. The bin is vibrated vertically (i.e., in the z -direction) following a sinus-shaped motion with amplitude r and rotation rate ω .

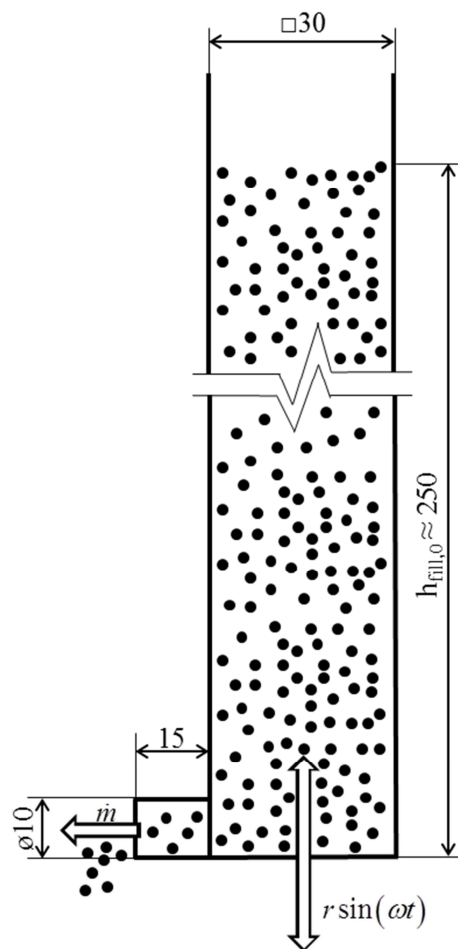


Figure 8: Sketch of the vibrating bin with main dimensions and initial filling height (dimensions are in [mm]).

Parameter	Value
Particle density (glass)	2500 [kg/m ³]
Poisson ratio for glass beads [41]	0.23
Poisson ratio for PMMA ¹	0.40
Coefficient of restitution glass/glass [42]	0.91
Coefficient of restitution glass/PMMA [42]	0.68
Coefficient of friction glass/glass [43]	0.09
Coefficient of friction glass/PMMA [43]	0.11

Table 1: Basic parameters of simulation

4.2 Effect of Simulation Parameters

4.2.1 Stiffness Effect on the Maximum Overlap

The Young's modulus for soda lime glass is 710^{10} [Pa] [41] and for PMMA $2.5 \cdot 10^9$ [Pa] [44]. Thus, glass beads are extremely stiff particles, rendering the use of the Young's modulus of the original system impossible when performing soft-sphere simulations. This is due to the short contact times, resulting in extremely small time steps (e.g., a typical contact time of a collision involving glass beads is $\Delta t_c = 3.4 \cdot 10^{-6}$ [s], which would result in a simulation time step size of approximately $\Delta t_{DEM} = 6.8 \cdot 10^{-8}$ [s]). In order to realize the computations, one has to adjust the simulation parameters in a way to get a result that is representative of the physical system. One metric to quantify how close the simulation is to the physical system is the (mean) overlap of particles during the collisions. As a rule of thumb, the maximum overlap should not exceed 1 [%] of the particle diameter in DEM-based simulations.

Therefore, test simulations are performed with different values for the Young's moduli and under various shaking conditions. In these simulations the ratio between the two Young's moduli of glass and PMMA is kept constant (i.e., $Y_{glass} / Y_{PMMA} = 28$). Specifically, simulations with fixed shaking conditions (i.e., 25 [Hz] and an acceleration of 5 [g]) were performed for a Young's modulus (of the particles) ranging from $7 \cdot 10^6$ [Pa] to $7 \cdot 10^8$ [Pa]. Furthermore, the effect of the shaking conditions was studied in simulations using a fixed Young's modulus of $7 \cdot 10^6$ [Pa], $7 \cdot 10^7$ [Pa] and $7 \cdot 10^8$ [Pa].

In order to compare simulation results, as well as to link the parameters of the collision model with the parameters describing the vibrations, a dimensionless number needs to be defined. Specifically, we have used a Froude number Fr' which is based on the ratio of the a characteristic vibration time scale t_{osc} (given by the frequency of the vibrations, i.e., ω_{osc}), and a collisional time scale t_c . The latter is related to the eigenfrequency ω_{DEM} inherent to the contact model. In order to reflect the effect of the vibrational acceleration, we have included the dimensionless vibrational acceleration Γ in the Froude number to arrive at:

$$Fr' = \frac{a}{g} \frac{t_{osc}}{t_c} = \Gamma \frac{\omega_{DEM}}{\pi \omega_{osc}}. \quad 4.1$$

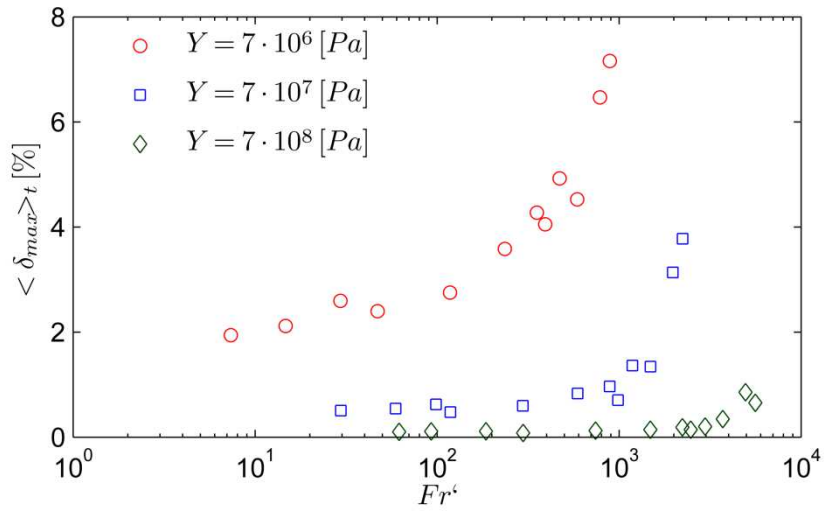


Figure 9: Time averaged maximum overlap over Froude number.

The time-averaged (normalized) maximum overlap $\langle \delta_{max} \rangle_t$ as a function of Fr' is shown in Figure 9. Clearly, $\langle \delta_{max} \rangle_t$ increases with increasing Fr' and decreasing stiffness of the particles. In order to collapse the curves for different values of Y , we first seek for an estimate of the dimensionless overlap δ_{ref} as a function of the particle stiffness in a system under a certain load characterized with a typical (contact) pressure p . Therefore, we use a scaled pressure to define a reference (dimensionless) overlap [12]:

$$\delta_{ref} \propto \frac{pd_p}{k}. \quad 4.2$$

Here k is the particle stiffness, i.e., the stiffness used in the linear spring-dashpot model. Now, we recognize that Young's modulus is related to k (for details see Eqn. 9.7 in the Appendix) via:

$$k \propto Y^{4/5} d_p (\rho_p v_{char}^2)^{1/5} \quad 4.3$$

We now combine the above equations, and recognize that the maximum overlap will be some multiple of the reference overlap δ_{ref} in the absence of vibrations, i.e., at $Fr' = 0$. Also, we use the maximal hydrostatic pressure $p_{hydro,max}$ (in a non-vibrated system) as the reference pressure since it can be easily calculated from the bed height and the bulk density. Hence, we arrive at the following expression for the scaled overlap $\langle \delta_{max} \rangle_t^*$:

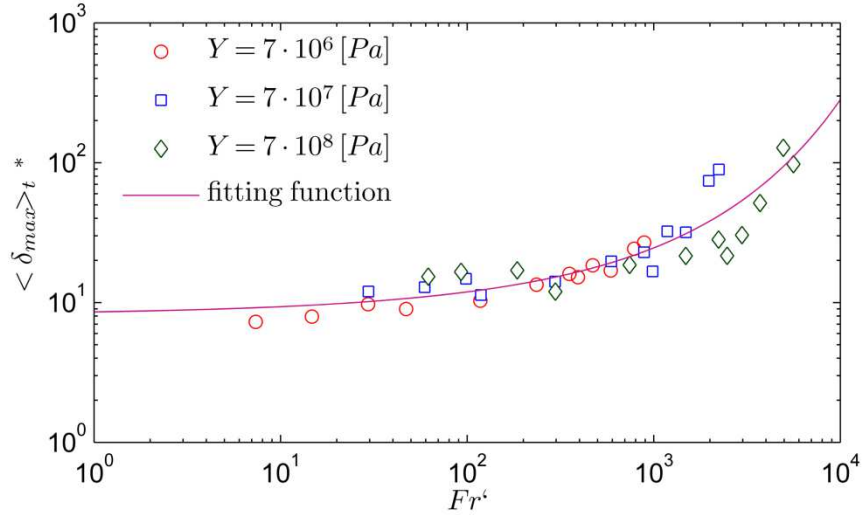
$$\langle \delta_{max} \rangle_t^* = \frac{\langle \delta_{max} \rangle_t}{\delta_{ref}} = \frac{\langle \delta_{max} \rangle_t Y^{4/5} (\rho_p v_{char}^2)^{1/5}}{p_{hydro,max}} \quad 4.4$$

We now correlate $\langle \delta_{max} \rangle_t^*$ and Fr' using an expression that predicts a constant value in the absence of vibrations, and gradually increases with increasing strength of vibrations, i.e., Fr' . Specifically, we find that the following expression approximates our results (shown in Figure 9) reasonably well:

$$\log \left(\langle \delta_{max} \rangle_t^* \right)^{0.5} = a + b \cdot e^{\log(Fr')} \quad 4.5$$

$$a = 0.955; b = 0.0112$$

The data shown in Figure 10 has been collected during simulations with a completely filled bin (no particle discharge), i.e., the hydrostatic pressure was fixed. In simulations with particle discharge the overlap $\langle \delta_{max} \rangle_t$ will decrease with time as reflected by our definition of $\langle \delta_{max} \rangle_t^*$ (since the hydrostatic pressure at the bottom of the bin will decrease as well). Hence, Eqn. 4.5 was applied to the situation of a completely filled bin to guide the selection of appropriately stiff particles (i.e., Y) in subsequent simulations.

Figure 10: Dimensionless overlap over Fr' .

4.2.2 Stiffness Effect on Discharge Behaviour

Despite ensuring a maximum overlap in the simulations, the question remains of whether the discharge behavior is influenced by the particle stiffness or not. Therefore, simulation runs were performed for the setup reported in Table 1 and various choices for Young's modulus as reported in Table 2. All simulations were performed at 5 [g] and 25 [Hz].

The chosen stiffness, required time step Δt_{sim} (see the Appendix for details on the choice of the time step), and the maximum overlap are summarized in Table 2.

Case Nr.	Y_p	Δt_{sim}	$\langle \delta_{max} \rangle_t$
11	$7 \cdot 10^7 Pa$	$1 \cdot 10^{-6}$	0.424 %
12	$7 \cdot 10^8 Pa$	$4 \cdot 10^{-7}$	0.082 %
42	$7 \cdot 10^9 Pa$	$1.6 \cdot 10^{-7}$	0.015 %

Table 2: Stiffness investigation: full run simulation parameters

Our data (see Figure 11) clearly indicates differences in the degree of fluidization as a function of particle stiffness, despite the maximal overlap is well below 1%. Figure 11a indicates the time evolution of the bin mass over time, highlighting that stiffer particles lead to a slower discharge (i.e., a larger bin emptying time) and consequently a sub-optimal fluidization. Figure 11b show the progressions of the filling height over the experiment, indicating (as expected) the same trends as the curve in Figure 11a. An “ideal” fluid (i.e., and inviscid and incompressible fluid) discharging from the bin would follow Torricelli's equation (Eqn. 4.6), i.e., the velocity of the fluid at the outlet is determined by the filling height and gravity:

$$v = \sqrt{2gh} . \quad 4.6$$

In contrast, the Beverloo correlation suggests no dependence of the outlet mass flow rate as a function of the filling height, and therefore a linear decrease of the mass in the bin with time. Figure 11c, showing the mass flow rate normalized by the total averaged mass flow rate, indicates Beverloo-like behavior for the stiff particles (i.e., case 42) for most of the simulation, while for the softer particles (case 11 and 12) the behavior is more complex and tends to follow more Torricelli's equation. At the end of each experiment, every case shows fluid-like behavior also revealed by Figure 11c, i.e., a regime transition occurs [22]. This is because a shallow particle bed can be easier fluidized, simply because more vibrational energy is available per particle. Our simulation results suggest that stiffer particles show a transition to this fluid-like behavior at a lower bed height.

In Figure 11b one can observe oscillations of the bed height for soft particles (i.e., cases 11 and 12), which is caused by the noticeable compressibility of these particles. After a time of approximately 12 [s], a change in the oscillation amplitude for case 12 can be noticed. Similarly, for case 11 such a change is observed after a time of approximately 19 [s]. These changes indicate a transition to a different regime of vibro-fluidization, as has been already discussed in Section 2.2.2. Figure 11c indicates that the regime transitions also results in a change of the discharge rate, noticeable by a kink at 12 [s] for case 12, and a weaker kink at 19 [s] for case 11. Furthermore, Figure 11b suggests that there is a second regime transition for case 12 at 32 [s].

Figure 11d is showing the curves of the dimensionless mass flow Tor (see Section 3) plotted over bed height. Note that Tor is plotted starting from $h^* = 0.2$ to 0.9, and data collected at earlier and later times was discarded. This is due to the data filtering procedure, which would result in incorrect measurements for earlier and later times (see Section 10.7). Figure 11d is also revealing the previous discussed issues concerning discharge behavior and regime changes. The Beverloo-like behavior of case 42 is indicated by a curve following $Tor \propto 1/\sqrt{h}$ and the Torricelli like behaviour of case 11 and 12 can be seen for some sections of the Tor curves indicated by a constant trend. Also the discussed regime changes are noticeable by kinks in the Tor curves.

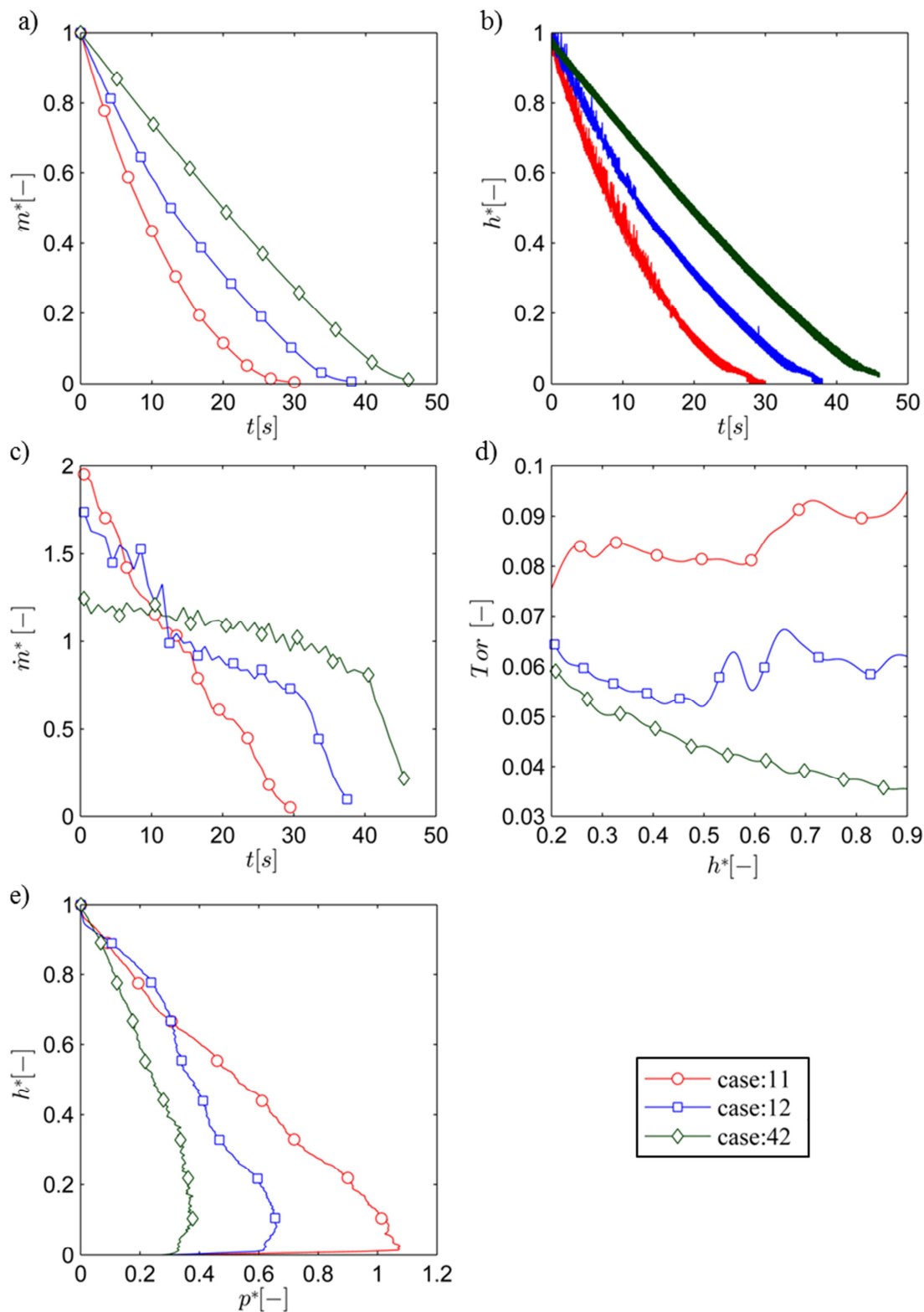


Figure 11: Effect of the particle stiffness on the simulation results: Time evolution of a) the total particle mass in the bin (normalized with the total particle mass at $t = 0$), b) the bed height (normalized starting bed height), c) the mass flow (normalized with time-averaged mass flow), d) Tor as a function of bed height, e) the time-averaged pressure (averaging was performed over the first second).

In Figure 11e the pressure distribution at early times (i.e., $t = 0 \dots 1$ [s]) is shown as a function of the bed height. Note, that the time averaging over the pressure is performed only over the

first second of the simulation, since the change of the bed height due to the discharge would lead to an incorrect average pressure. The pressure reported Figure 11e is calculated from the particle contact stresses and normalized by the (hypothetical) hydrostatical pressure (for details on the calculation of this reference pressure see Appendix 9.3). The (hydrostatic) pressure distribution in an ideal fluid would be linear, which is only the case for case 11.

Our simulation results suggest that with increasing stiffness the pressure distribution becomes increasingly non-linear, i.e., typical for granular materials. As discussed in the “Background” section, there is better fluidization in the top layers of deep beds. The thickness of the fluidized top layer increases with increasing shaking strength. Thus, we expect similarly flat pressure profiles near the top of the particle bed up to a certain depth, which is the case for the soft and moderately stiff particles (see case 11 and 12 in Figure 11e). However, the little duration of averaging leads to deviations of the pressure curves in this regions (i.e. the over prediction of case 12). Another interesting feature is observed for case 11: the maximum pressure near the bottom is (on average) higher than the maximum hydrostatic pressure. We speculate that the reason for this behavior is that soft particles experience more bed oscillations (see Figure 11b) and thus absorb a higher amount of kinetic energy. This energy dissipates when the particles hit the bottom of the bin, and thereby cause the higher pressure levels.

As in the previous simulations the ratio of the Young’s moduli of particles and bin was kept constant. Another set of simulations, using stiffer bins, lead to the same results compared to simulations with same particle stiffness. We conclude that the bin stiffness is from minor importance and the system behavior is governed most by particle stiffness.

4.2.3 Influence of Wall Friction

Janssen’s classical analysis suggest that the pressure profile a bin filled with granular material is influenced by wall friction and the lateral stress ratio [33]. Thus, on the one hand we expect that a reduction of the wall friction will lead to a hydrostatic pressure profile in the bin. On the other hand, however, we expect that (for a vibrated system) the energy injected via frictional forces between particles and the lateral walls will decrease. Hence, the level of fluidization may decrease when decreasing wall friction.

In order to test which of the two effects is dominating the pressure profile, an additional simulation was performed with zero wall friction coefficient. (see Figure 12). Clearly, the pressure profile in the case with frictionless walls (i.e., case 64 in Figure 12) becomes linear near the bottom of the bin. Hence, frictional forces between particles and the lateral walls do

not contribute to the vibro-fluidization of the granular material. Clearly, a combination of materials with a low friction coefficient is preferable when aiming on fluidizing a particle bed using vibrations.

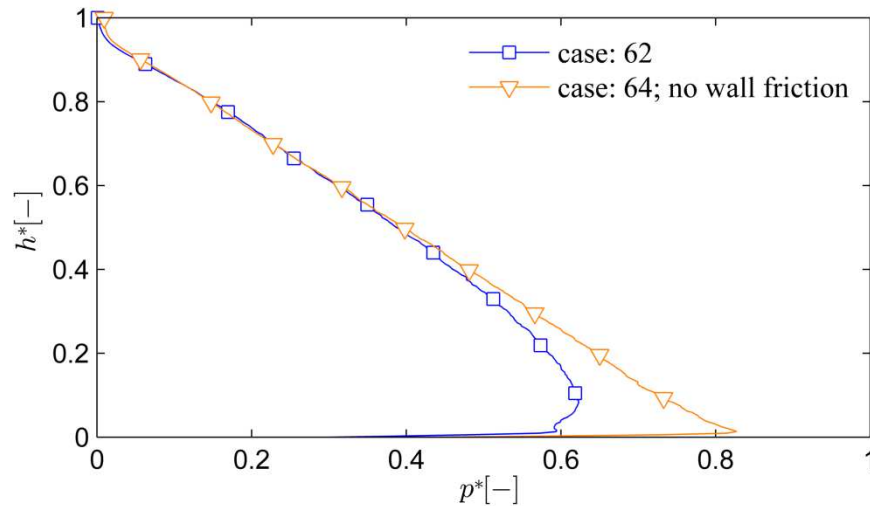


Figure 12: Time-averaged pressure profile (averaged of 5 [s]) with and without wall friction (both systems were vibrated at $\Gamma = 5$ and 25 [Hz]).

4.3 Segregation

We have monitored the mean vertical position of each particle class in all of our simulations in order to investigate whether segregation occurs or not. In order to get a single segregation parameter, we have recorded the vertical (dimensionless) distance Δz^* of “large” (i.e., that in the two classes with the biggest diameter) and “small” (i.e., that in the three classes with the smaller diameters) normalized with the mean particle diameter as a function of time. While initially this distance is close to zero (particles were placed randomly into the bin), we observe a slow drift of the large particles towards the top of the particle bed (see Figure 13).

After 5 [s] of shaking, Δz^* is approximately 1.4 for comparably low shaking strength (i.e., case 77) and about 0.1 for high shaking strength (i.e., case 87). Thus, vibrations lead to a certain degree of segregation, which is, however, in the order of one particle diameter in our system. Consequently, we do not expect segregation to influence the discharge behaviour.

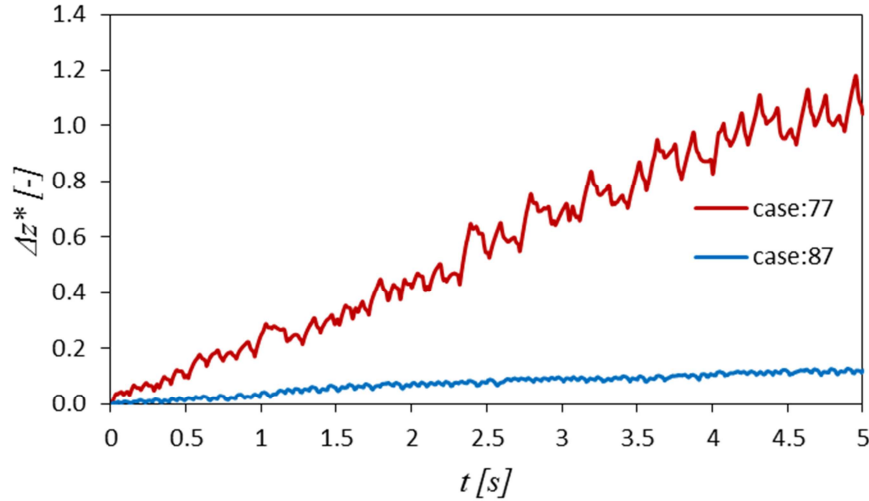


Figure 13: Mean vertical distance of large and small particles (case77: $Y = 7 \cdot 10^8$ [Pa], 25 [Hz], $\Gamma = 5$; case87: $Y = 7 \cdot 10^8$ [Pa], 100 [Hz], $\Gamma = 16$).

4.4 Effect of the Orifice

Explorative simulations have shown that the orifice design is critically impacting the pressure distribution near the bottom of the bin. Hence, we have performed simulations over 5 seconds of real-time (i) with the original orifice design but no discharge, and (ii) without an orifice. Table 3 summarizes the simulation conditions, in which we have also varied the particle stiffness.

Case Nr.	Y_p	Δt_{sim}	Bin
61	$7 \cdot 10^7 Pa$	$1 \cdot 10^{-6}$	<i>with orifice</i>
62	$7 \cdot 10^8 Pa$	$4 \cdot 10^{-7}$	
63	$7 \cdot 10^9 Pa$	$1.6 \cdot 10^{-7}$	
76	$7 \cdot 10^7 Pa$	$1 \cdot 10^{-6}$	<i>without orifice</i>
77	$7 \cdot 10^8 Pa$	$4 \cdot 10^{-7}$	
78	$7 \cdot 10^9 Pa$	$1.6 \cdot 10^{-7}$	

Table 3: Simulation settings for the investigation of the effects due to particle stiffness and orifice design.

Simulation results are summarized in Figure 14 and suggest that the pressure field near the top of the particle bed, i.e., for $h^* > 0.7$, is unaffected by both stiffness and orifice design. Simulations with softer particles (i.e., cases 61, 76 and 62, 77) indicate that the orifice has a only weak impact on the pressure distribution. Specifically, the presence of an orifice leads to a slightly lower pressure near the bottom of the bin. As will be discussed in the next paragraph, this is caused by the larger dilatation of the particle bed for simulations with an orifice. The situation becomes more pronounced for the stiffest case (i.e., case 63 and 78 for

which $Y_p = 7 \cdot 10^9$ [Pa]), in which the pressure profiles are strongly impacted by the presence of the orifice. In order to pinpoint the origin of this difference, videos of the simulations were analyzed with a special focus on the orifice region. Furthermore, the vertical volume fraction profile was analyzed and is discussed next.

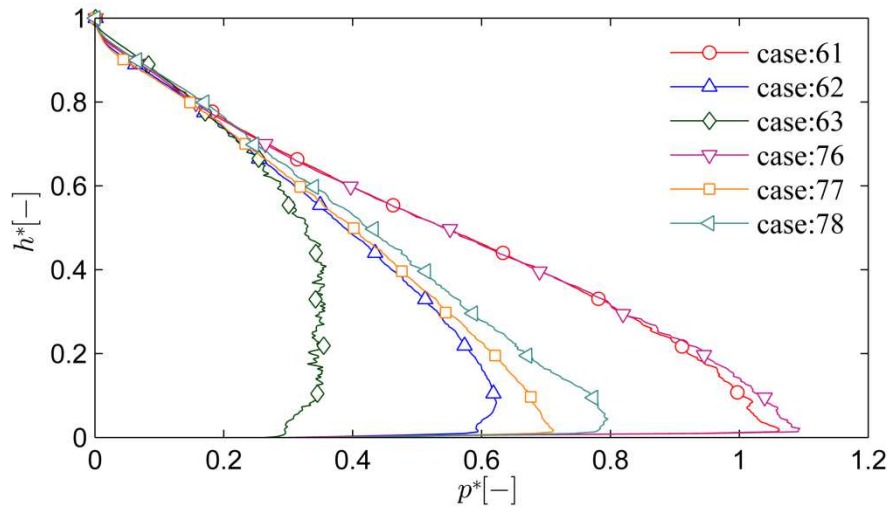


Figure 14: 5 [s] Averaged pressure profiles plotted over the scaled particle bed height: bin with orifice (61, 62, 63) and without orifice (76, 77, 78).

Figure 15 shows three snapshots for two variations of the particle stiffness with and without orifice, in which particles are colored according to the force acting on them. Snapshots were recorded at three instances of time, which are identical for each simulation setup. In Figure 15a the localized stress distribution in the particle is visible, i.e., videos reveal that a pressure wave propagates vertically upwards in the bin for the cases 77 and 78. This is not the case for the simulations with an orifice at this instance of time, because a comparably large region void of particle develops at the bottom of the bin. The instantaneous pressure profile is also reflected by the particle volume fraction distribution in the bin, visible in Figure 16a, which indicates a steep increase of ϕ_p near the pressure wave (i.e., case 77 at $h \approx 0.02$ [m] and for case 78 at $h \approx 0.05$ [m]).

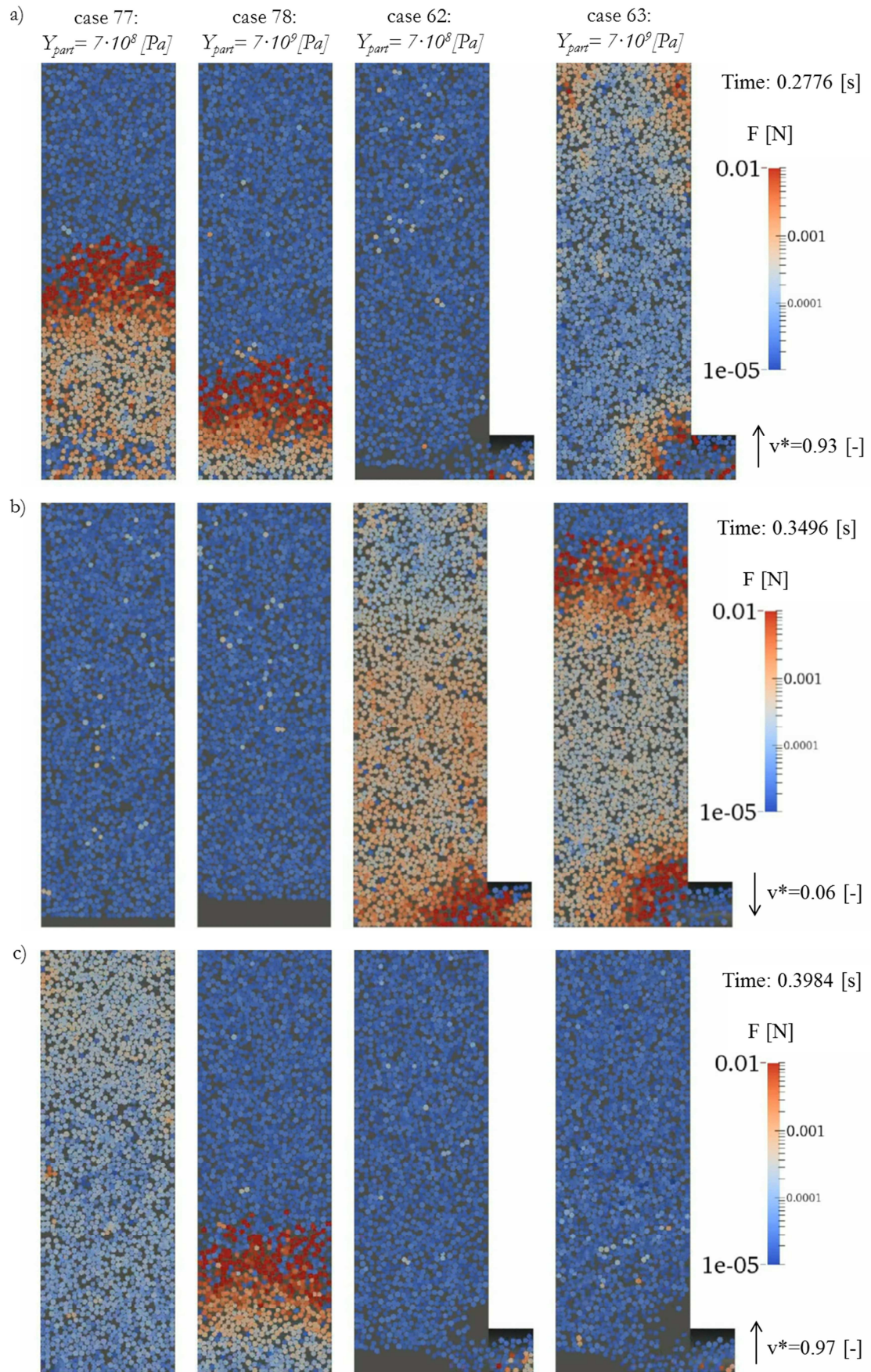


Figure 15: Snapshots of DEM-based simulations (a thin slice near the center of the bin is shown, particles are colored according their force; v^* indicates the current shaking velocity normalized with the maximum velocity, the shaking direction is indicated by the arrow)

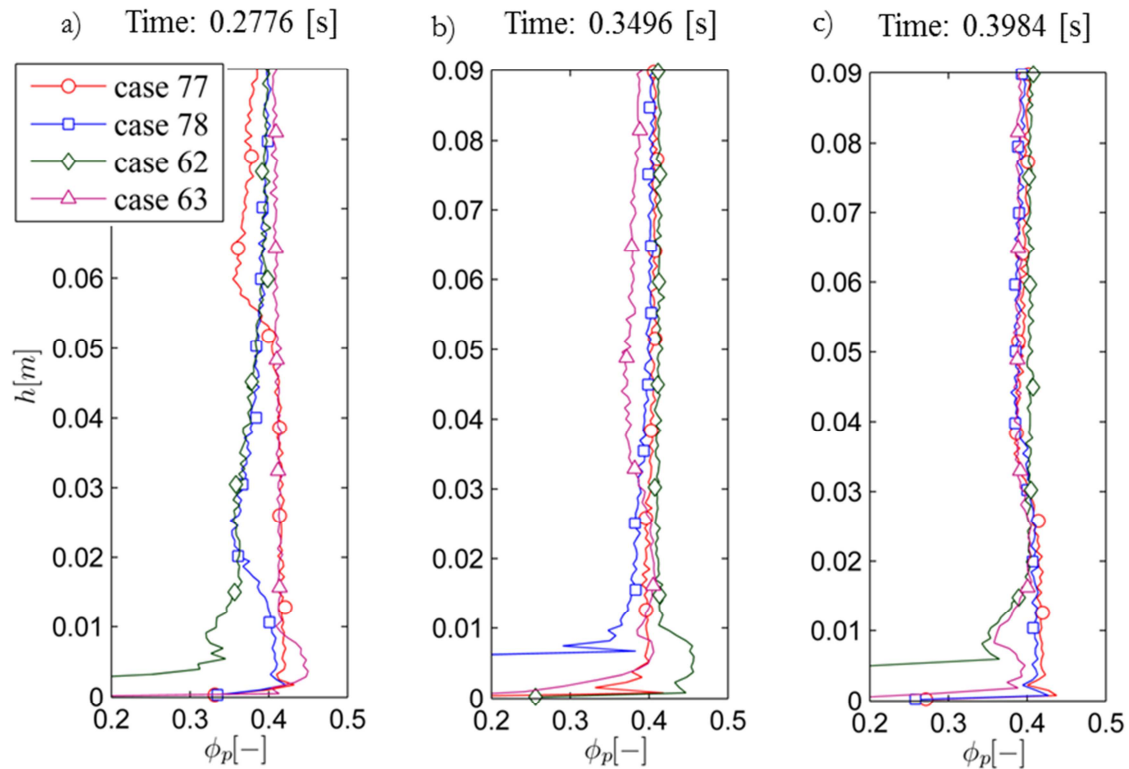


Figure 16: Snapshots of DEM-based simulations: volume fractions plotted over height in accordance to Figure 15

Figure 15b shows a snapshot at an instance of time in which a pressure wave develops in the bins with an orifice. In comparison with the pressure fields in the simulations without orifice, the pressure wave is not as localized, and occupies a much larger region of the particle bed. Case 63 even reveals a second high-pressure region near the orifice. The volume fraction profiles in Figure 16b also indicate that the stress transmission is less abrupt in the case with orifice. Clearly, regions of high pressure are not as clearly reflected by regions of high ϕ_p as it was the case for the simulations without orifice.

In Figure 15c the particle bed is shown at an instance of time in which the bed is lifted off the bottom of the bin with orifice. This reveals that the outlet acts like a buffer zone. In the particle bed's lifted condition, the particles from the outlet are moving back into the bin. In the moment the particle bed is contacting the bottom of the bin again, the cylindrical region of the orifice is filled with particles. As the particles flow into the orifice region, particles collide with the lateral walls of the bin causing a high-pressure region as is visible in Figure 15b for case 63, and to a lesser extent for case 62. This more complex pressure distribution is the reason why the pressure curves for the bins with orifice suggest an insufficient fluidization near the orifice region (see Figure 14). Thus, on average a lower pressure is observed with an

orifice, since the latter acts like a buffer that dampens pressure fluctuations. Consequently, we expect that the influence of the orifice decreases when decreasing the length of the orifice.

Note that in our analysis the particle volume fraction profile was determined from all particles in a certain horizontal slice of the computational domain and the volume of the slice. The latter was computed from the cross sectional area of the bin (without orifice) and the vertical extend of the slice. Thus, ϕ_p in slices near the orifice do not correspond to a mean particle volume fraction, but rather to a hypothetical volume fraction that would be obtained in case the orifice would be absent (see Section 9.3 for details).

Results displayed in Figure 15 also suggest a significant effect of the particle stiffness for the simulations without an orifice (compare case 77 and 78). This effect was not observed when looking at the time-averaged data shown in Figure 14. The reason for this discrepancy is that the snapshots reported in Figure 15 can be only used to qualitatively compare the stress distribution, since the latter is highly dynamic. In order to illustrate this, we have time-averaged the pressure distribution between 0.24 [s] and 0.4 [s] (i.e., over 4 oscillations, see Figure 17). We find that such a short-term average is different from the long-term averages presented in Figure 14, and only qualitative agreement can be found (e.g., the flattening of the pressure profile for bins with orifice can be found in short- and long-term averaged).

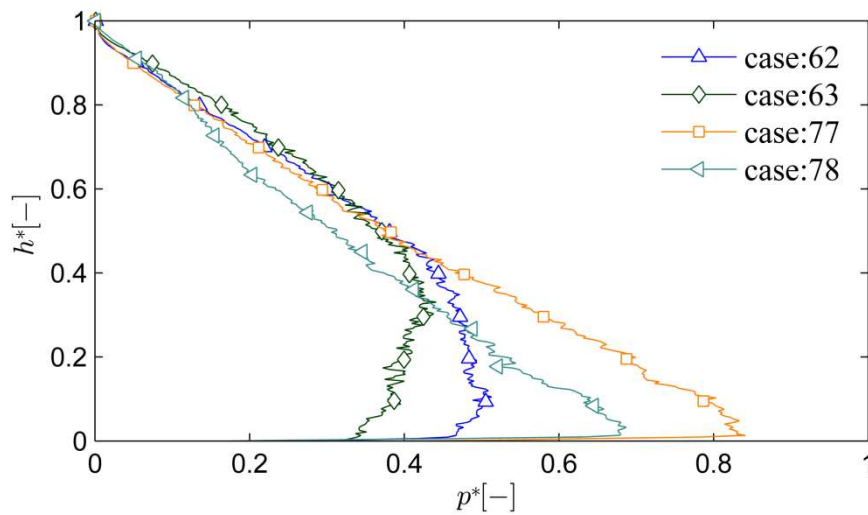


Figure 17: Pressure profiles for bins with (cases 62 and 63) and without (cases 77 and 78) averaged over 0.16 [s].

4.5 Effect of Bin Design

Enhanced fluidization of the particle bed should be gained by special shaped bins. Therefore 5 seconds of real-time simulations are worked out with different bin designs.

As seen in Section 4.2.2, a deep particle bed of stiff particles gets only weakly fluidized. This is due to the fact that the particles are supported more and more by the bin walls with increasing depth causing a constant pressure over wide range in the bottom region [27]. Different bin designs are realized based on the concept of dividing the particle bed in a series of small particle beds stacked above each other. In simulations with a particle stiffness of $Y_p = 7 \cdot 10^8$ [Pa] and vibration parameters of 25 [Hz] and $\Gamma = 5$ over a duration of five seconds real-time, the averaged pressure profiles were measured. Figure 18 shows the investigated bin designs and Figure 19 provides the results.

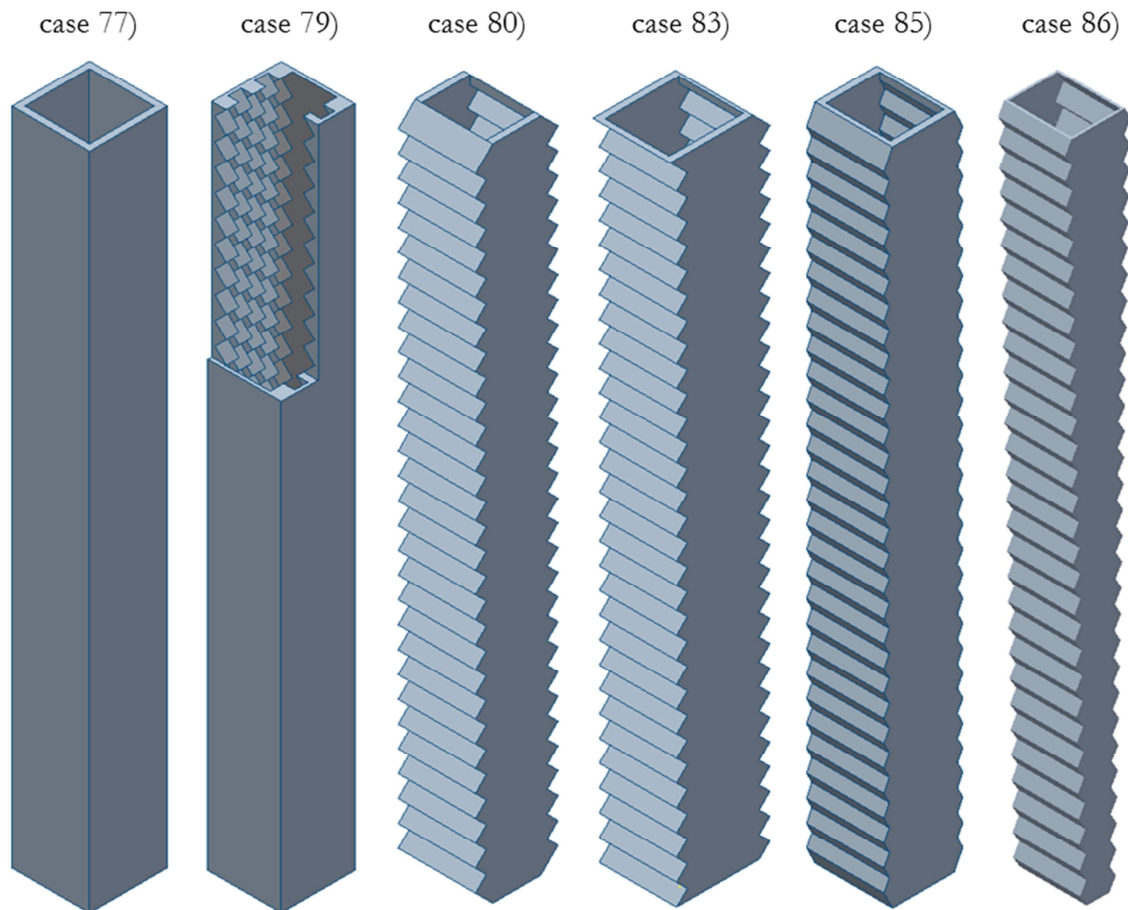


Figure 18: Bin designs used in DEM-based simulations.

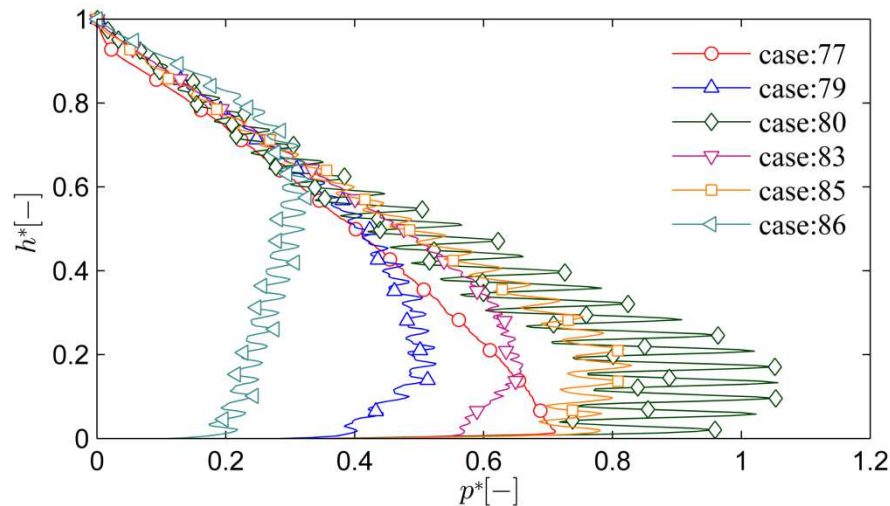


Figure 19: 5[s] averaged pressure profiles over particle bed height for different bin designs

As can be seen in Figure 19, the bin design changes have major impact on the pressure distribution. In comparison to the standard straight bin design (i.e., case 77) a better fluidization can be achieved by using jagged walls in case 80. However, this leads to pressure peaks at the tips regions because particles get trapped between the tips and are not able to move freely anymore. A bin design studied in case 79 aimed on eliminating these pressure peaks. However, particles get jammed in the bottom region, due to the overall rough walls, i.e., the corners and edges of bin design used in case 79.

The bin design studied in case 83 yielded results similar to the ones obtained with the original straight bin. The only difference was that more jamming in the bottom region was observed in case 83.

The best compromise between fluidization and pressure peaks is obtained with the bin design studied in case 85. This design uses jagged walls, however, a flatter angles was used compared case 80. While a similarly good fluidization level compared to case 80, the bin design used in case 85 showed smaller fluctuations in the pressure distribution. Unfortunately, a flat pressure profile was also obtained in the bottom region of the bin also for case 85.

Next, a cone shaped design with jagged walls was studied (see case 86). The idea was to increase the pressure by using an overall conical-shaped wall and enhance fluidization in the bottom region. However, the fluidization becomes even worse when using such a design. We speculate that the reason for this behavior is that the bin gets too narrow at the bottom, such that particles cannot be fluidized and get jammed.

In order to guide future work, the following conclusions can be drawn for the effect of the bin design:

- a narrow bin design (i.e., less than 10 particle diameters) inhibits vibro-fluidization and should be avoided,
- by partitioning the bin into a series of shallow particle beds stacked above each other (e.g., by introducing jagged walls) vibro-fluidization can be enhanced,
- the angle of individual features in jagged walls should be optimized in order to positively affect vibro-fluidization. Also, it can be expected that the shape of individual features will influence vibro-fluidization, and hence should be investigated,
- rough walls with a large specific surface area (e.g., like studied in case 79) causes more friction, and hence vibro-fluidization is inhibited.

4.6 Summary

In summary, our simulations indicate that

- particle stiffness has a major effect on vibro-fluidization,
- vibro-fluidization of a deep particle bed becomes increasingly difficult with increasing particle stiffness. Hence, we expect that real-life (extremely stiff) particles only allow a partial vibro-fluidization once the bed has exceeded a certain height. More systematic investigations need to be performed in order to study the effect of the stiffness of the wall material,
- a low friction coefficient between particles and wall enhances vibro-fluidization,
- the regime of vibro-fluidization will change because of the decrease of bed height, causing variations in (i) the discharge rate and (ii) the oscillations of the bed height,
- simulations with a stiffness reflecting that of glass are not feasible with our current computational resources, and hence a comparison with experimental data is essential.

With respect to the latter, we planned experiments with the following questions in mind:

- Do the regime transitions observed in the simulations also occur in the experiments?
- What is the influence of the (dimensional) shaking frequency f and the (dimensionless) acceleration Γ on the discharge and vibro-fluidization behavior?
- What is the influence of the orifice position?

5 Experiments

5.1 Setup

The setup of the experiment consists of

- a narrow bin constructed from PMMA with a design matching that of the base case used in the simulations, including an orifice which can be mounted on different heights,
- an air-cooled electro dynamic shaker,
- a computerized control loop for the shaker, including an amplifier, an acceleration sensor and a data recording system,
- a chute for guiding the particles from the orifice onto the scale,
- a dynamic scale measuring the instantaneous weight gain due to particle discharge from the bin, as well as
- a high-speed camera for recording the evolution of the bed height.

A detailed description of the setup can be found in the Appendix (see Section 10).

5.2 Experiment I: Orifice at the Bin Bottom

In these experiments the orifice of the bin was mounted at the bottom allowing a complete discharge of the bin. The initial particle mass was 0.250 [kg] for each experiment. Since the particle bed height cannot be accurately measured below a certain limit, the experimental data is only analysed for filling heights above 30 [mm], i.e., approximately 30 time the particle diameter. Each experiment is performed in triplicate, and the results are presented as mean values with error bars representing a 98% confidence interval for the mean values. Typically, these confidence intervals were within 10% of the mean, indicating excellent reproducibility of our experiments.

Table 4 provides an overview of the chosen parameters of the conducted experiments. Figure 20, Figure 23, Figure 24 and Figure 25 present the results of the experiments for vibrational frequencies of 25 [Hz], 50 [Hz], 75 [Hz] and 100 [Hz], respectively. In these figures panel a) indicates the time-evolution of the discharged mass scaled with the total discharged mass. Panel b) shows the progress of the particle bed height normalized with the initial bed height in dilated state (i.e., under vibrated conditions). Note, that the normalization is done in order to better compare individual results: since the vibration conditions affect the bulk density, experiments with identical initial mass of particles would yield different initial bed heights and

hence different (dimensional) height profiles (see Figure 28 at the end of this Section). Panel c) shows the dimensionless quantity Tor , which is used as the key quantity to interpret our experimental data.

Experiment	f [Hz]	Γ [-]	r [mm]	V_b [-]
1	25	4	1.59	2.28
2	25	5	1.99	2.85
3	25	6	2.39	3.42
4	25	7	2.78	3.99
5	25	8	3.18	4.56
6	50	6	0.60	1.71
7	50	8	0.80	2.28
8	50	10	0.99	2.85
9	50	12	1.19	3.42
10	50	14	1.39	3.99
11	75	8	0.35	1.52
12	75	10	0.44	1.90
13	75	12	0.53	2.28
14	75	14	0.62	2.66
15	75	16	0.71	3.04
16	100	8	0.20	1.14
17	100	10	0.25	1.43
18	100	12	0.30	1.71
19	100	14	0.35	2.00
20	100	16	0.40	2.28

Table 4: Overview of shaking parameters used in experimental runs I with $m_0 = 0.250$ [kg].

Note that in our subsequent discussion Tor is plotted starting from $h^* = 0.2$ to 0.9, and data collected at earlier and later times was discarded. This is due to the data filtering procedure in the post processing, which would result in incorrect measurements for earlier times.

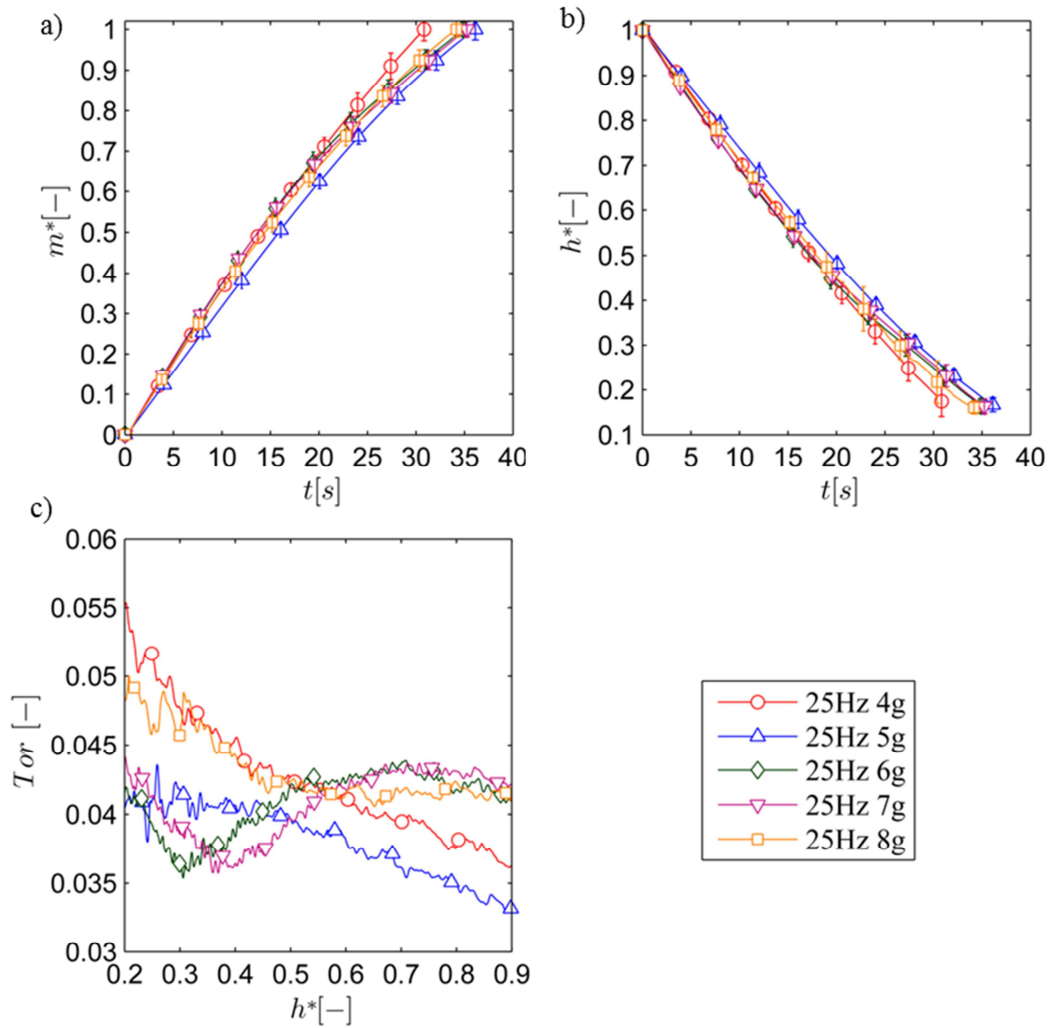


Figure 20: Results for experiment I and a vibration frequency of $f = 25$ [Hz].

Our results shown in Figure 20a and b indicate that for the case of $f = 25$ [Hz] there is no clear trend of the discharge rate with respect to the acceleration. While we could not exactly pinpoint the reason for this behavior, we speculate that the comparably large amplitudes used in the experiments cause this peculiar behavior: movies of the experiments reveal that the discharge process is disturbed by the lifting of the particle bed in the bottom region of the bin. This leads to situations in which the cross section of the orifice is not completely filled with particles. In addition, the comparably large amplitudes (see Table 4) also cause large fluctuations of the particle bed's surface. Specifically, we have observed that single particles exit the particle bed, which makes tracking of the bed height difficult and inaccurate. Particle exiting events become more frequent at the end of each experiment, i.e., in case of shallow beds. This is also reflected by the increasing confidence intervals towards the end of each experiment shown in Figure 20b. Figure 21 shows snapshots of two critical regions of the particle bed, illustrating these findings.

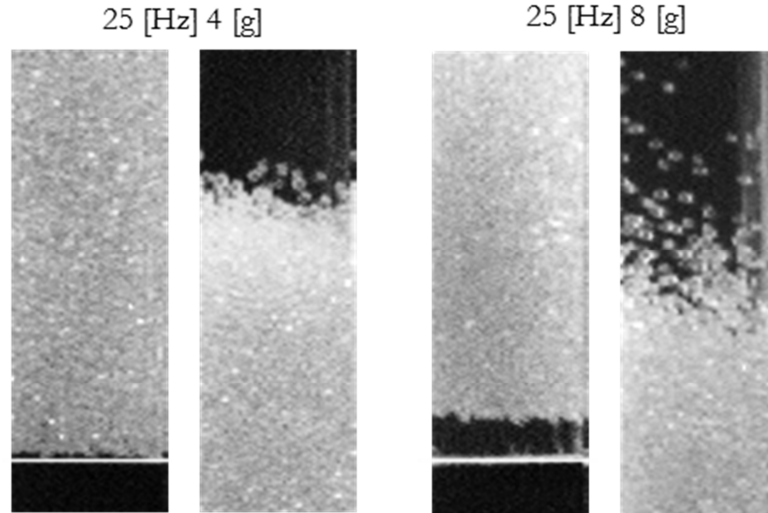


Figure 21: Maximum detachment of the particle bed near the bottom of the bin (left panel), as well as a diffuse top layers (right panel) for two different accelerations and $f = 25$ [Hz] in initial filled bin.

Figure 20c reveals that the discharge rate undergoes various regime changes as a function of the filling height. The cases with accelerations of $\Gamma = 6, 7$ and 8 show a fluid-like (inviscid) discharge behavior for heights above 60% of the initial bed height, indicated by an almost constant value for Tor close to 0.042 . Thus, the discharge rate corresponds to that predicted by Torricelli's law taking a (constant) correction factor 0.042 into account. This indicates that only ca. 5% of the hydrostatic pressure energy (at the bottom of the bin) can be converted to kinetic energy of the exiting particles. Clearly, the vibro-fluidized particle bed cannot be considered as being inviscid, but it behaves like a viscous fluid when flowing through the orifice. Also, the compressibility of the particle bed must be taken into account, since it can lift off the bottom, and particles can detach from the free interface (see Figure 21).

For intermediate bed heights (i.e., $0.3 < h^* < 0.6$) and accelerations of $\Gamma = 6$ and $\Gamma = 7$ we observe a decrease of the level of fluidization (indicated by a drop in Tor) with decreasing h^* . This results in a strong decrease of the dimensional discharge rate with decreasing h^* . We speculate that this is caused by a lower particle volume fraction near the orifice, since we expect that for decreasing h^* a hydrostatic pressure profile will persist. We argue that the lower particle volume fraction near the orifice is caused by the lifted-off particle bed. Indeed, our experimental results presented in Section 5.3 support this speculation. An alternative explanation is that the effective granular viscosity increases, leading to a regime where the discharge rate is controlled by (granular) viscosity (see our discussion in Section 3). Figure 22 is showing the Tor curve of $\Gamma = 6$ compared to a hypothetical highly viscous behaving fluid. Unfortunately, we were unable to measure the particle volume fraction in the experiment runs,

same as the pressure or the effective granular viscosity at the bottom of the bin to substantiate this speculation.

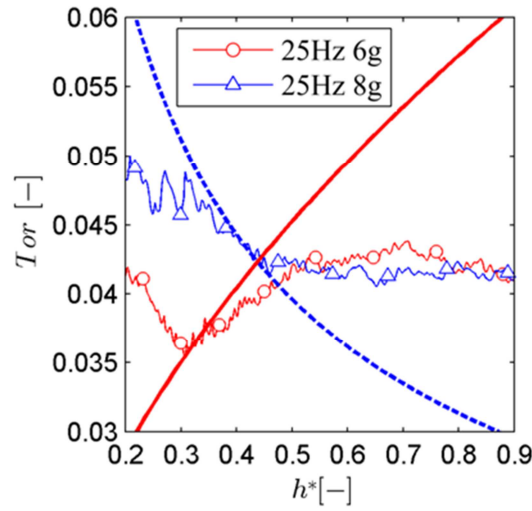


Figure 22: Comparison of selected experimental data with fluid-like and Beverloo-like discharge behavior (the dashed line indicates granular behavior, i.e., $Tor \propto 1/\sqrt{h^*}$; the solid line indicates viscous behavior, i.e., $Tor \propto \sqrt{h^*}$).

For lower bed heights (i.e., $h^* < 0.3$) an increase of Tor with decreasing bed height close to $Tor \propto 1/\sqrt{h^*}$ is observed, i.e., similar to the discharge behavior of a granular material. This can be seen for the case of $\Gamma = 8$ in Figure 22, which is showing the Tor curve compared to a curve following $Tor \propto 1/\sqrt{h^*}$. Only our data for $\Gamma = 5$ does not show this behavior, but in contrast approaches a plateau level for $h^* < 0.4$. This is clearly due to the onset of fluidization for upon a decrease of the bed height (a similar behavior was observed for higher frequencies as explained in the following paragraphs). The observed $Tor \propto 1/\sqrt{h^*}$ relationship for $\Gamma = 4$ is explain by “classical” granular discharge behavior, as in this experiment the bed was never fluidized.

For $\Gamma \geq 6$, however, the data for $h^* < 0.3$ is more difficult to interpret, since the particle bed must be fluidized (i.e., $Tor = \text{const}$ for $h^* > 0.3$, indicating fluidization already for deep beds). Consequently, solid-like discharge behavior is clearly not expected, and an increase of Tor with decreasing h^* seems peculiar for $\Gamma \geq 6$. Indeed, have observed this peculiar discharge behavior for a fluidized granular material only in a single other experiment (see our data for $f = 75$ [Hz] in one of the following paragraphs). We speculate that under certain vibration conditions and a steadily decreasing bed height the level of fluidization is increased, leading to a smaller effective viscosity of the granular material near the orifice. Consequently, the

discharge rate, and hence Tor increases for decreasing h^* . Unfortunately, we were unable to track down the exact reason for this discharge behavior, since we were unable to separately detect the particle volume fraction, the effective viscosity, or the pressure at the orifice experimentally.

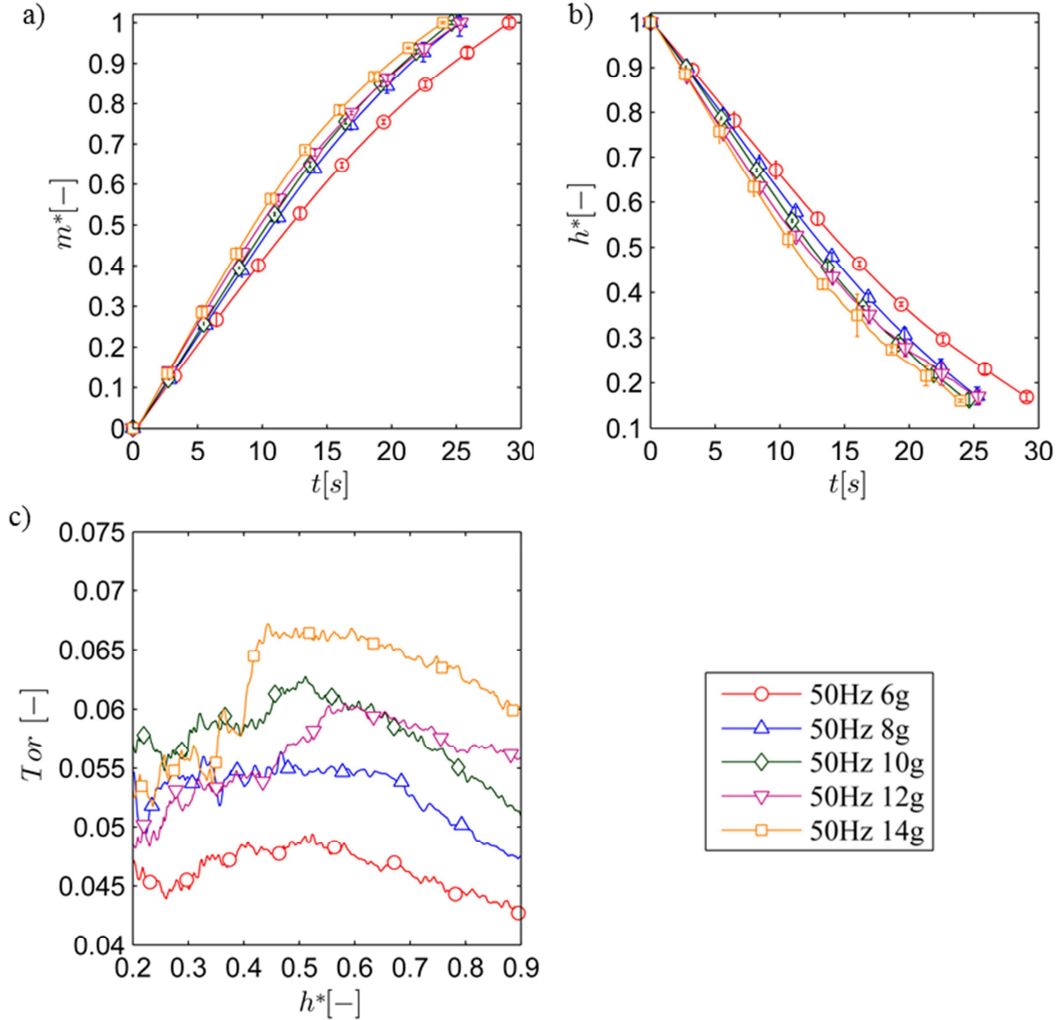


Figure 23: Results for experiment I and a vibration frequency of $f = 50$ [Hz].

Next we consider the experimental runs performed at higher vibration frequency (i.e., $f = 50$ [Hz]). Figure 23a and b indicate a gradual decrease of the discharge time with increasing acceleration, i.e., improved vibro-fluidization at higher Γ . This improved fluidization behavior can also be seen in Figure 23c for $h^* > 0.55$, i.e., Tor increases monotonically for increasing Γ . For shallow beds, however, this trend vanishes, and Tor decreases more or less abruptly with decreasing h^* depending on Γ . Specifically, for accelerations $\Gamma \geq 10$, a sudden drop of the dimensionless mass flow is observed. Since the particle bed is fluidized for all vibration settings (at least for a certain range of h^*), and the

discharge rate changes abruptly, we speculate that this drop is caused by a decrease of the particle volume fraction in the orifice region due to a lift-off of the particle bed. In summary, the experiment with $\Gamma = 8$ shows the most favorable vibro-fluidization behavior, and Torricelli-like discharge rate is observed for $0.3 < h^* < 0.7$. This clearly indicates that for $f = 50$ [Hz] the concept of a vibro-fluidized powder feeder can be realized within a certain range of h^* .

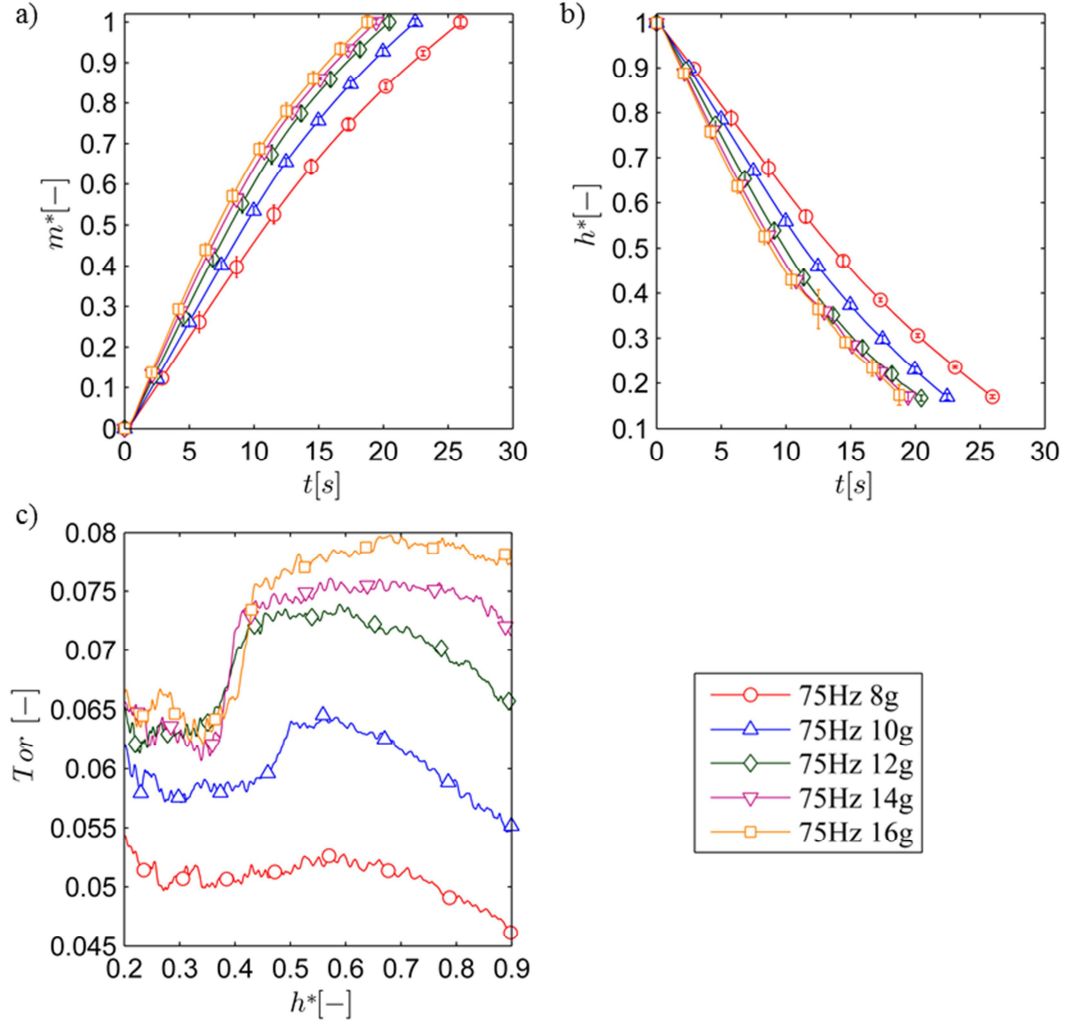


Figure 24: Results for experiment I and a vibration frequency of $f = 75$ [Hz].

For $f = 75$ [Hz] the discharge behavior improves further, and a clear correspondence between total time needed to discharge the granular material and Γ is observed. Again, we observe a sudden drop for Tor when decreasing the bed height for accelerations $\Gamma \geq 10$. These drops are larger than that observed for the experimental runs using $f = 50$ [Hz]. An exception is the case with $\Gamma = 8$, for which we observe an almost constant value for Tor for $0.3 < h^* < 0.6$, and a slight increase of Tor with decreasing h^* for very shallow beds. Torricelli like discharge

can also be observed for case with $\Gamma = 14$ in the range $0.45 < h^* < 0.85$. This second set of adequate vibration conditions (i.e., in which Tor is almost independent of h^*) at high accelerations seems to exist only for sufficiently high vibration frequencies. Next, we have performed vibration experiments at an even higher vibration frequency to substantiate if this is truly the case.

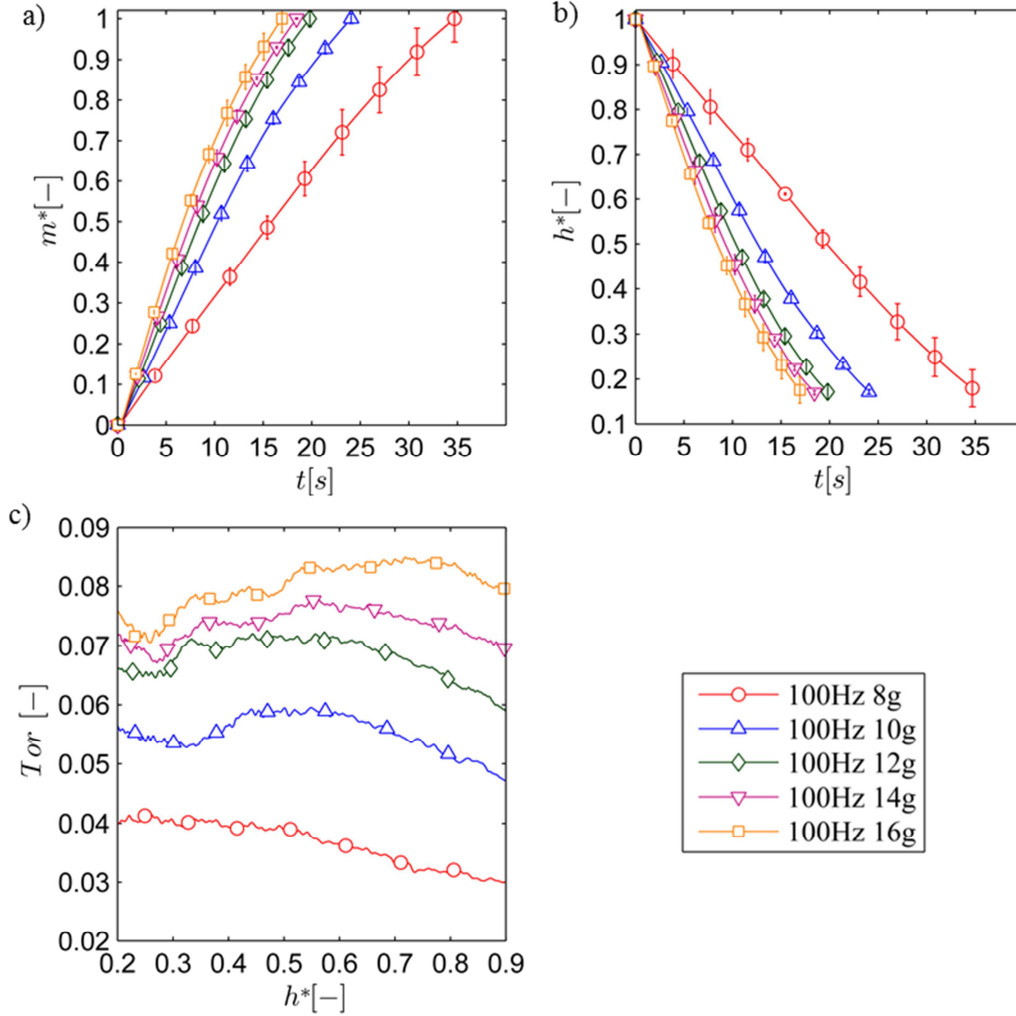


Figure 25: Results for experiment I and a vibration frequency of $f = 100$ [Hz].

Our data shown in Figure 25 clearly indicates that this is indeed the case, i.e., for $\Gamma \geq 12$ adequate vibro-fluidization is observed for a range of bed heights (see panel c in Figure 25). Also, a more pronounced effect of the acceleration on the discharge rate can be observed, suggesting that the discharge rate can be controlled more easily compared to situations with $f < 100$ [Hz]. The best fluidization conditions for $f = 100$ [Hz] are observed for $\Gamma = 16$ case and $0.55 < h^* < 0.8$. Under these conditions we have also measured the highest level of fluidization, i.e., Tor was close to 0.085. For $\Gamma = 16$ and $h^* < 0.55$ the dimensionless

discharge rate appears to gradually decrease with decreasing h^* , indicating that viscous effects in the orifice become more and more important for shallow beds.

In order to visualize the behavior of the granular material upon discharge, the data for the experimental run with the best fluidization conditions, i.e., $\Gamma = 16$ and 100 [Hz] is compared to the Torricelli's law in Figure 26. Clearly, granular materials discharge much slower compared to a fluid. However, a clear dependency of the discharge rate for vibro-fluidized granular material is visible.

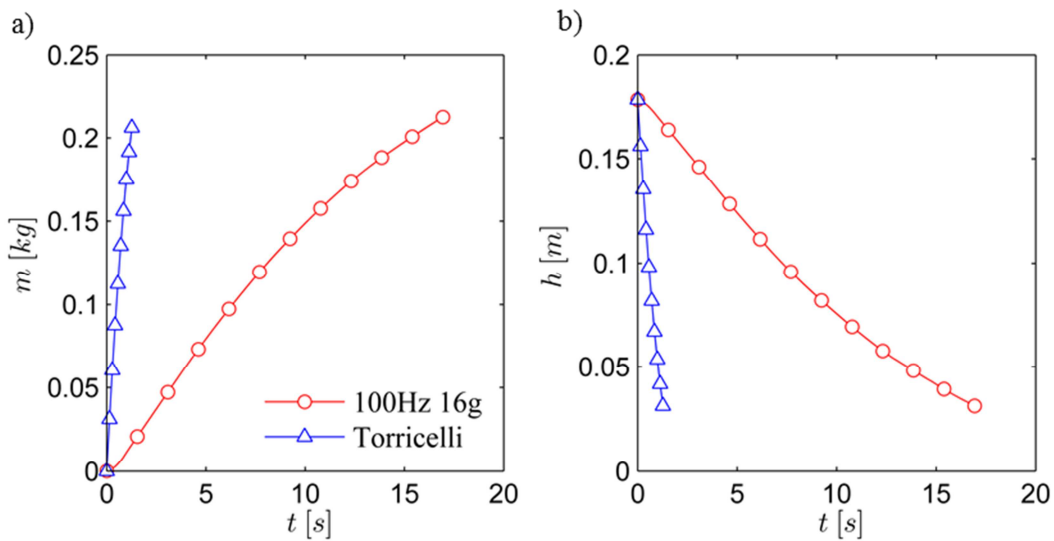


Figure 26: Comparison of the discharge mass (left panel) and bed height (right panel) for a granular material and a fluid (i.e., Torricelli's law).

Figure 27 compares the mean values of \overline{Tor} (indicated by an overbar), as well as the relative standard deviation, for various vibration settings. This is done to illustrate under which vibration conditions an adequate fluidization level can be obtained. Clearly, an increase of \overline{Tor} with increasing acceleration (for a fixed vibration frequency) gets more pronounced at higher vibration frequencies: while for 25 [Hz] no sensitivity with respect to Γ is noticeable, for 100 [Hz] an almost linear increase of \overline{Tor} with Γ is observed. However, the mean relative error of \overline{Tor} does not show a conclusive trend. As discussed before, this is due to the various regime transitions triggered by a change of h^* during the experiments.

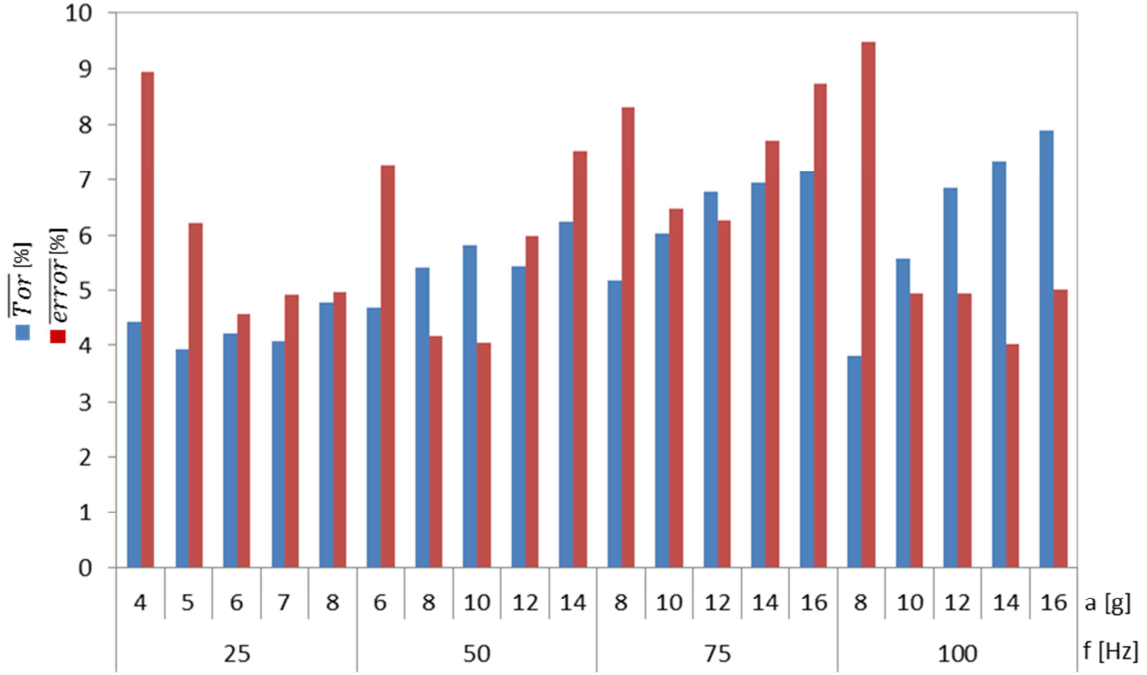


Figure 27: Overview of the mean dimensionless discharge rates \overline{Tor} , as well as its mean relative error for $0.2 < h^* < 0.9$.

We finally report the relative bed expansion before we discharge particles, i.e., $\Delta h^* = (h_0 - h_{fin}) / h_0$. Therefore, the top of the particle bed was monitored with a high speed camera, and the bed height was extracted from the images taking into account the current position of the bottom of the bin. The initial bed height h_0 was recorded for each experiment over 5 [s] with an acquisition frequency of 200 [Hz], i.e., averaging was performed over 1000 time instances. The image analysis tools available in *Matlab*[®] were used for this purpose. Figure 28 reveals that the bed expansion is mainly depending on the dimensionless vibration amplitude r^* , normalized with the mean particle diameter. The dimensionless acceleration Γ has only a weak influence. Specifically, we observe that for $\Gamma = 8$ (and $f = 50$ and 75 [Hz]), as well as for $\Gamma = 4$ (and $f = 25$ [Hz]) the bed expansion is below the trend. Most important, the largest bed expansion is observed for $f = 25$ [Hz] and $\Gamma = 6$ and 8 . This is due to the lift-off of the particle bed, i.e., the formation of a large void space near the bottom of the bin. As discussed, this void space also impacts the discharge rate.

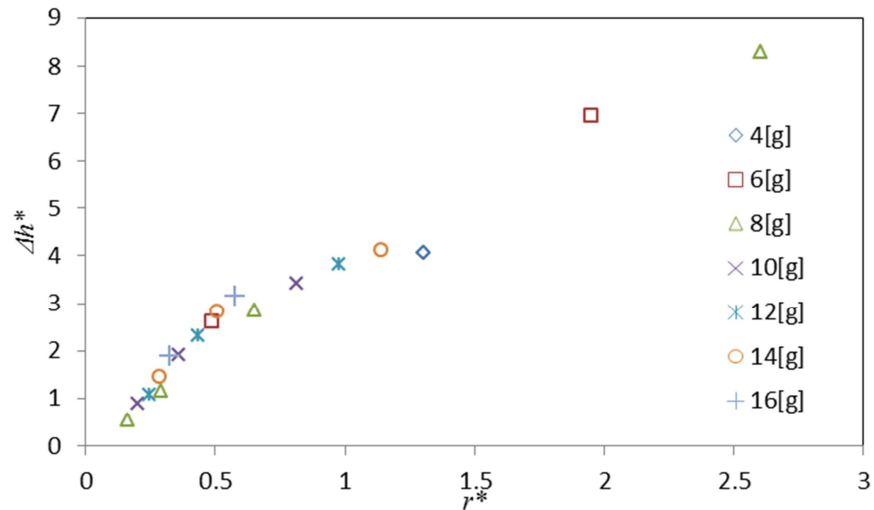


Figure 28: Bed expansion Δh^* as a function of the dimensionless shaking amplitude r^* for experiment I.

5.3 Experiment II: Orifice located at $h/d_p \approx 37$

An additional set of experiments was performed to study the influence of the positioning of the orifice. As discussed in Section 5.2, the particle bed may be lifted off the bottom for certain vibration parameters. Thus, the orifice (which was located at the bottom of the bin) may not always be covered with particles, consequently the discharge rate may decrease.

In the following experiments the orifice is positioned at a height (distance from the lower edge of the orifice to the bin bottom) of $h = 45$ [mm], ensuring that it is always covered by particles. In order to obtain comparable results, the bed height used to compute T_{or} is measured relative to the orifice position, i.e., for experiment II the orifice height was subtracted from the total bed height to obtain h .

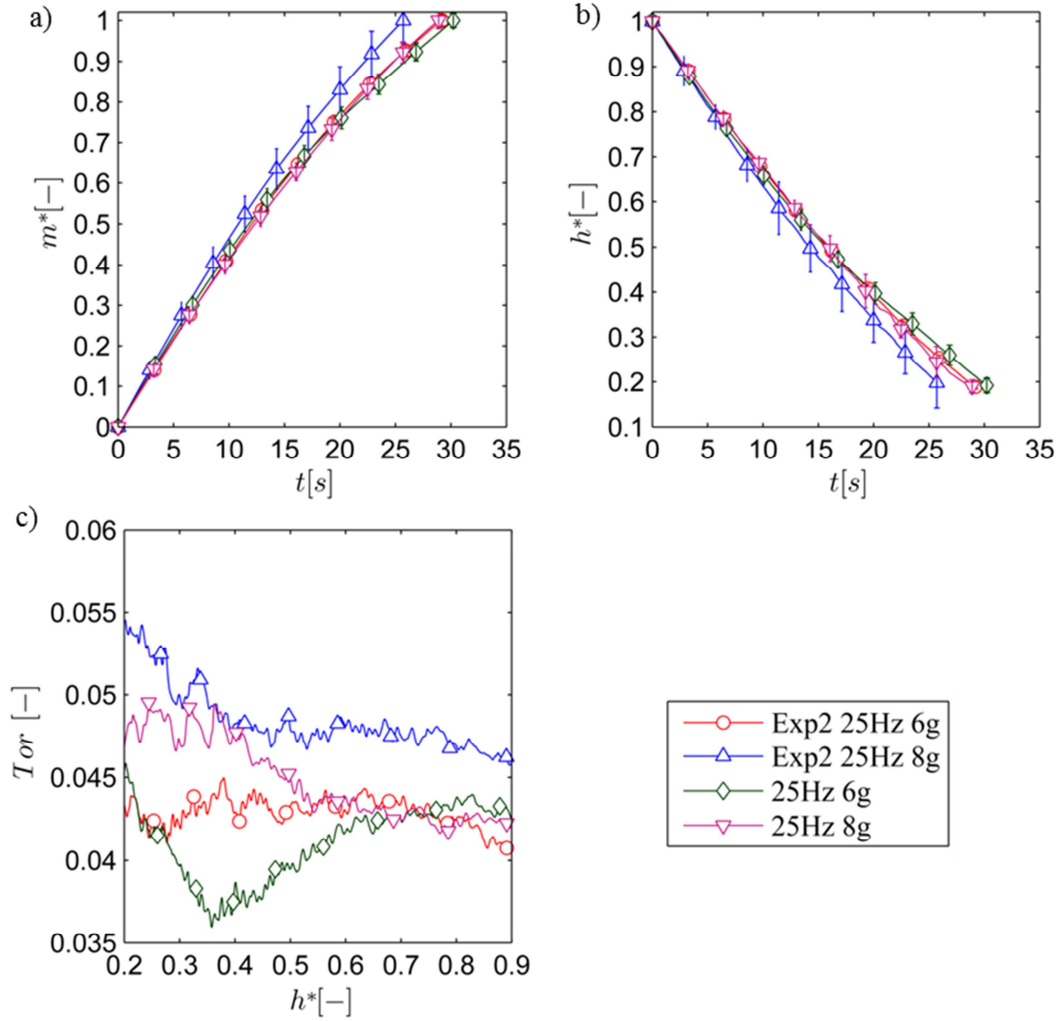


Figure 29: Comparison of data from experiments with different orifice position at $f = 25$ [Hz].

In Figure 29 the results of experiments with $f = 25$ [Hz] for setup I and II are shown in order to visualize the effect of the orifice position. As expected, the dip in the data for Tor for experiment I (see green diamonds in Figure 29c) is not observed in experiment II. The absence of this dip also leads to a substantial decrease of the time for a total discharge of the bin, as can be seen in Figure 29a. This indicates that for experiment I (and for large vibration amplitudes) the lift off of the particle bed indeed influences the discharge rate. This effect is bigger in the case of higher vibration amplitudes (i.e., $\Gamma = 8$), while in the case of 6 [g] the deviation becomes more pronounced for $0.3 < h^* < 0.6$. This is because the lift-off of particles becomes stronger for shallow beds under these vibration conditions. In Figure 29c the dimensionless discharge rate curves again illustrate the higher discharge rates obtained with the experiment II. Most important, our data for $\Gamma = 6$ illustrates that an almost constant value for Tor can be achieved when eliminating the effect due to lift off of the particle bed.

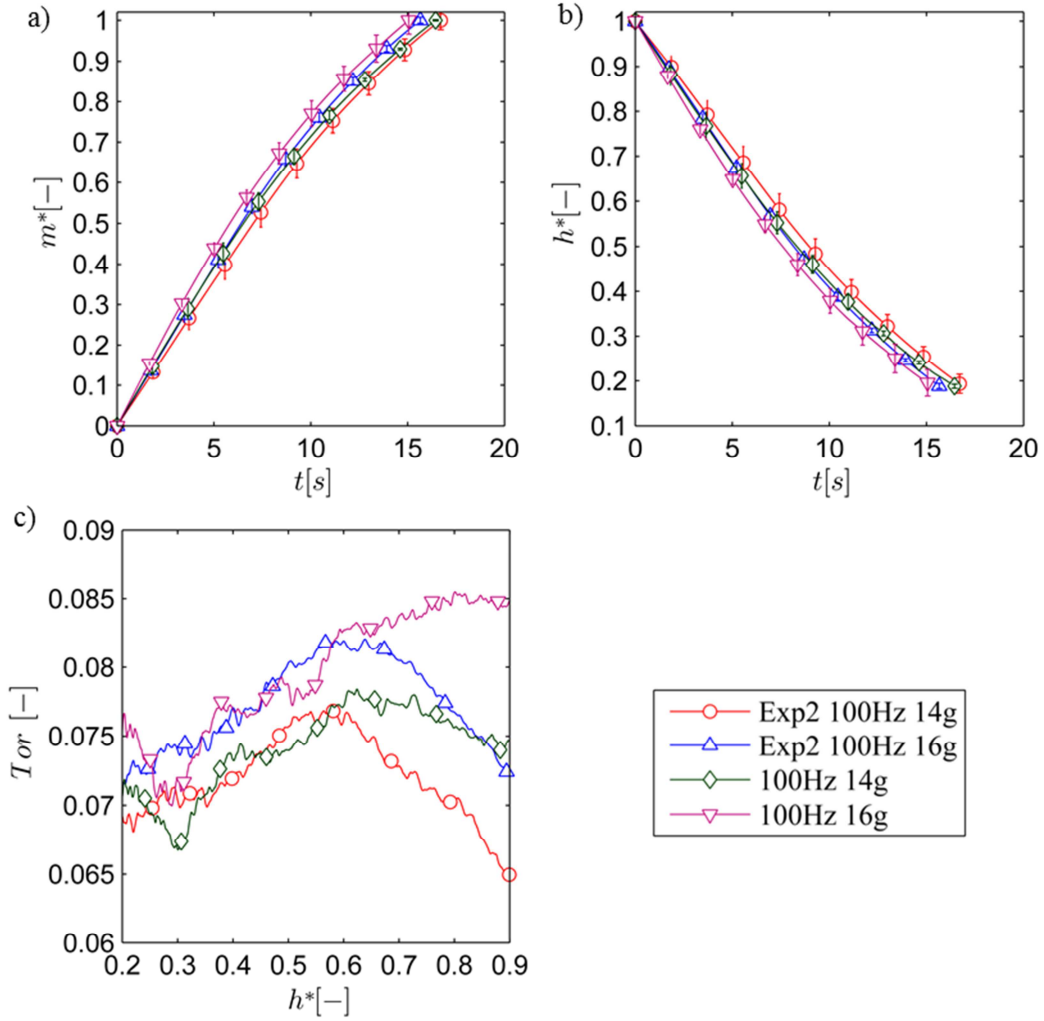


Figure 30: Comparison of data from experiments with different orifice position at $f = 100$ [Hz].

Figure 30 shows a comparison of the experiments with different orifice position for $f = 100$ [Hz]. These cases required very small vibration amplitudes, and hence no lift-off of the particle bed was observed. Thus, it can be expected that the particle volume fraction close to the orifice is constant, and hence changes of ϕ_p do not cause the decreasing T_{or} for decreasing h^* . This is also supported by the smooth transition of the curves for experiment II, which is in contrast to the sudden drop of T_{or} in case lift off of the particle bed is observed. Consequently, it is reasonable to assume that viscous effects lead to the decrease of T_{or} for $h^* < 0.6$. In contrast, the T_{or} curves show a different behaviour for a dimensionless bed height of $h^* > 0.6$, for which we observe (i) comparably small discharge rates, as well as (ii) solid-like discharge for experiment II. This indicates that for deep beds (such as the ones used in experiment II) the fluidization is indeed more difficult, in line with literature. Most important, this indicates that for an orifice located above the bottom of the bin, a shift from a solid-like to a fluid-like (but viscous) flow regime is triggered.

5.4 Summary

Our experiments can be summarized as follows:

- Torricelli-like discharge behaviour, i.e., that of an inviscid fluid can be induced by vibrating a granular material. However, the discharge rate is only a small fraction of that suggested by Torricelli's law, indicating that frictional effects need to be considered,
- the particle bed experiences various regimes of vibro-fluidization during discharge, since the particle bed height is a critical parameter for vibro-fluidization. In general, regime transitions occur for accelerations $\Gamma > 10$,
- adequate conditions for vibro-fluidization are observed for higher frequencies (i.e., 75 and 100 [Hz]) and accelerations $\Gamma > 12$,
- the bed expansions primarily depends on the shaking amplitude, and
- the vertical position of the orifice is of key importance, since it determines whether lift-off of the particle bed near the bottom of the bin has an effect or not.

6 Comparison of Simulations and Experiments

For experiment I (i.e., with the orifice at the bottom of the bin) with shaking parameters of $f = 25$ [Hz] and $\Gamma = 5$ a corresponding simulation run was performed. The simulations were performed for three different choices of the particle stiffness: $7 \cdot 10^7$ [Pa], $7 \cdot 10^8$ [Pa] and $7 \cdot 10^9$ [Pa] (i.e., equal to 0.1%, 1% and 10% of the real particle's stiffness).

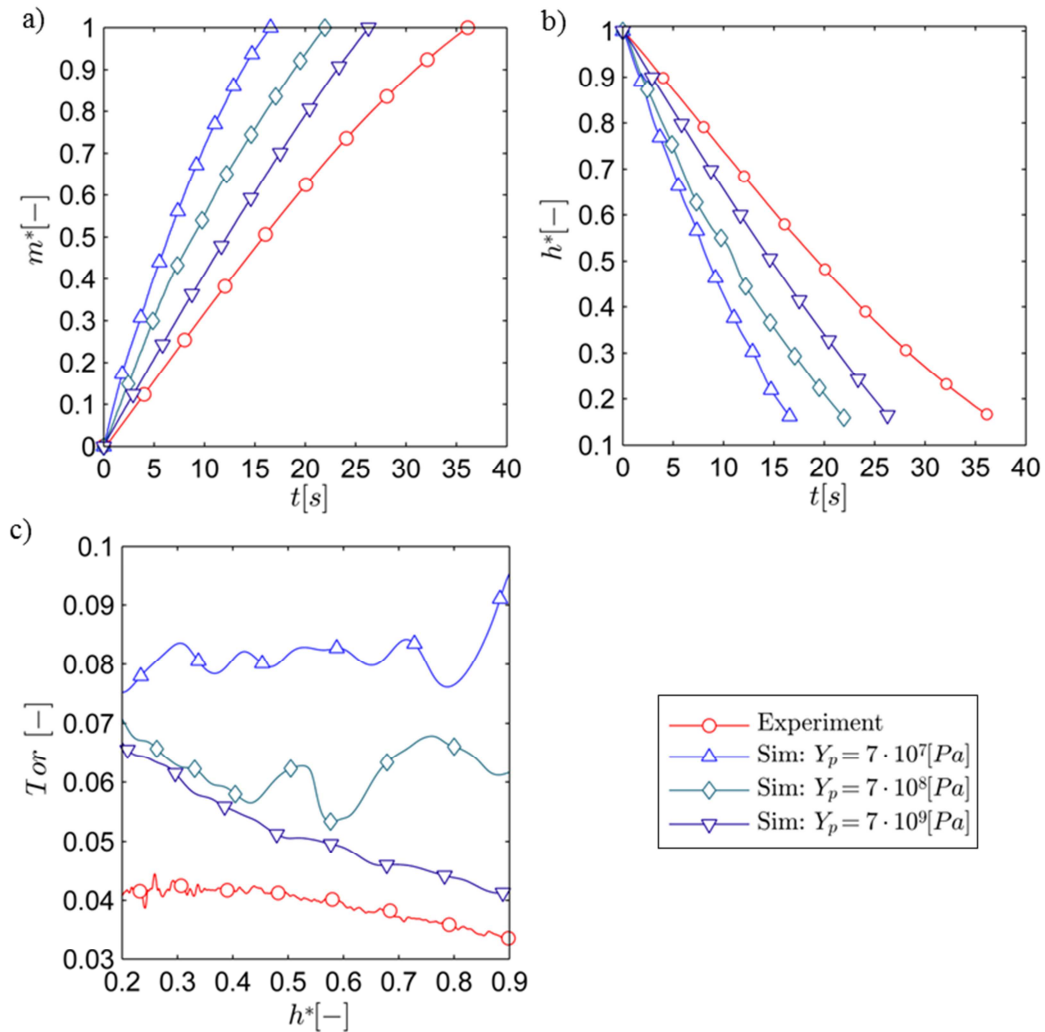


Figure 31: Comparison of results for experiment I with simulation data ($f = 25$ [Hz] and $\Gamma = 5$).

Our results (see Figure 31) clearly indicate that the particle stiffness is a key influence parameter, and all simulations significantly overpredict the discharge rate. However, when approaching the true particle stiffness, our simulation data approaches the experimental results. Specifically, we observe that our simulation results approach the qualitative Tor vs. h^* behavior for the experiment for comparably deep beds (see Figure 31c, $h^* > 0.5$). Most important, however, the simulations are unable to predict the discharge behavior for shallow

beds. We have addressed more detailed investigations to explain this discrepancy to future work.

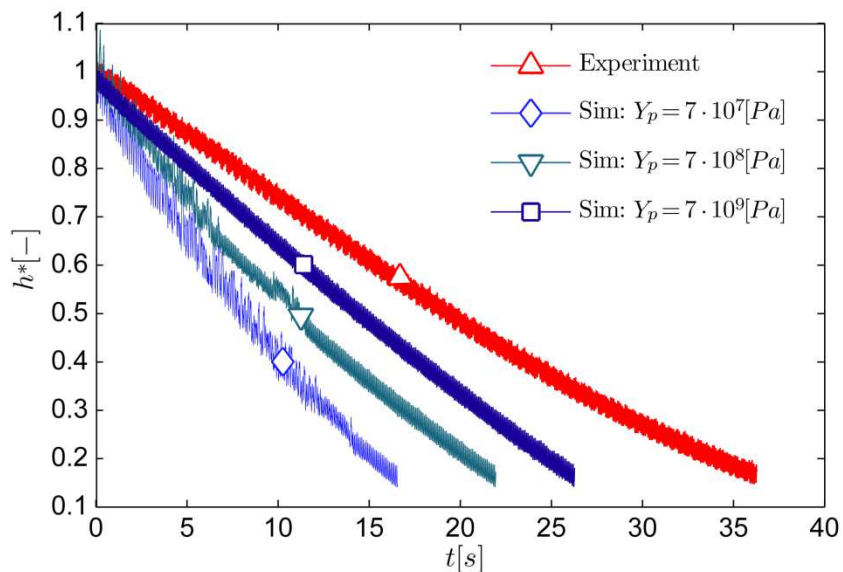


Figure 32: Raw height data curves of experiment and simulations: $f=25$ [Hz], $\Gamma = 5$

In Figure 32 the raw data of the time evolution of the bed height during the experiments and simulations is presented. The experimental curve is showing very regular oscillations over the total duration of the experiment. This indicates that the particle bed experiences no regime transition, which is supported by our data for the dimensionless mass flow rates (see Figure 20). Considering the simulation data, the two cases with a low Young's modulus clearly show different oscillation behaviours, implying that regime transitions do occur. Our simulation results for the stiffest particles indicate that regime transitions are hard to predict by using simulations involving particles with a comparably low stiffness.

7 Conclusions and Outlook

The current study focused on the development of a particle feeder that relies on vibro-fluidized particles. The key idea is to use vibrations to change the flow behavior of the particles, which offers new possibilities to control the discharge rate. Soft-sphere DEM-based simulations have been performed to study key phenomena in vibro-fluidized beds, and to quantify the influence of the most important simulation parameters. These simulations revealed that the particle stiffness, as well as the design of the orifice severely impacts the stress distribution in the bin. Since the true particle stiffness could not be modeled in the simulations, data from these simulations was used for qualitative interpretations, with the following key findings:

- The maximum particle-particle overlap in soft-sphere simulations is a function of the shaking parameters and the particles' Young's modulus. We propose a model for predicting the maximum overlap which can be used to choose an appropriate Young's modulus for given vibration conditions.
- The Young's modulus of the particles (i.e. the particle stiffness) critically affects the collective behavior of the particles, and thus fluidization and discharge characteristics. When approaching the true stiffness of the particles, the simulation results (for the discharge rate) become more and more representative of the experimentally determined data. This is especially true for comparably deep beds.
- In a vibrated particle bed, most of the energy is dissipated at the walls due to friction. Also, vertical walls do not contribute to fluidize the particle bed. This implies that a low friction coefficient between particles and wall is preferable to enhance fluidization.
- The simulations indicate that deep particle beds in straight bins get poorly fluidized. To enhance fluidization, investigations with different bin designs have been performed. The results of these simulations suggest that bins which divide the particle bed in a series of shallow particle compartments have advantageous fluidization characteristics. Narrow particle beds should be avoided, since those regions would inhibit particle fluidization. Moreover, our investigations have shown that even small changes in the geometry, in combination with stiff particles, can lead to quite different fluidization behaviors.

Next, an experimental setup was designed to quantify the effect of shaking parameters on the degree of fluidization and the discharge behavior of glass beads with a mean diameter of about

1.2 [mm]. These experiments indeed show that a sufficient fluidization of the particle bed can be obtained, however, only under certain conditions. Our experimental findings can be summarized as follows:

- The degree of fluidization, and consequently the discharge rate, is a function of the bed height, and hence can be predicted only over a limited range of bed heights. This is because the particle bed at sufficiently high accelerations (i.e., $\Gamma > 10$) is vibro-fluidized in different regimes.
- While Torricelli-like discharge behaviour can be observed, the discharge rate is only a small fraction of that given by Torricelli's law. Thus, the fluidized particles behave like a compressible viscous fluid, and frictional losses during discharge must be taken into account.
- Based on the mean values of the dimensionless discharge parameter, we conclude that with increasing frequency and acceleration the bed is fluidized to a higher degree. However, stable Torricelli-like discharge is only achieved over a range of bed heights, as well as certain combinations of acceleration and frequency. Preferred conditions for vibro-fluidization are observed at 25 [Hz] and $\Gamma = 6$ (with an orifice at $h/d_p = 45$), as well as 50 [Hz] and $\Gamma = 6$ (with the orifice at the bottom).
- In situations with high amplitudes, particles lift off of the bottom of the bin, which is sub-optimal for the case where the orifice is at the bottom of the bin.
- The bed expansion due to vibrations is proportional to the shaking amplitude.

The current study is a small step towards a more complete understanding of the discharge behaviour of vibrated particle beds. However, several other parameters need to be examined in future research in order to complete our picture of these systems. Questions like

- How do smaller particles and cohesive powders behave under vibrated conditions?
- How does the particle size influence the discharge behaviour?"
- Is interstitial air playing a role in such particle beds?
- What is the effect of the orifice designs, and its position on the bin?

still need to be answered. In order to accurately control the discharge rate via an adjustment of the bed height in a vibro-fluidized particle bed, a conventional powder dosage device (e.g., a loss-in-weight feeder) is still required from today's point of view. This is because the fill level in the bin has to be controlled via an online height measurement system (e.g., an ultrasonic sensor, a capacitive sensor, or an optoelectronic sensor). Such a combined system of a loss-in-

weight and a vibro-fluidized particle bed can be expected to decrease fluctuations in the feed rate, since the instantaneous discharge rate is given by the current bed height. In any case, the selection of an appropriate (i.e., accurate and robust) height measurement system should be given special attention in future work.

Another interesting area of application for a vibro-fluidized powder feeder is the dosage of a well-defined amount of powder, e.g., for capsule-filling processes: since the particles in the vibro-fluidized bed behave like a viscous fluid, it should be possible to reproducibly dose a defined amount of (possibly even cohesive) powder with a higher rate compared to an unvibrated system. For such a system the question remains on the optimal open/close mechanism for the orifice for fast and accurate dosage of powder.

8 References

- [1] S. Mascia, P.L. Heider, H. Zhang, R. Lakerveld, B. Benyahia, P.I. Barton, et al., End-to-end continuous manufacturing of pharmaceuticals: integrated synthesis, purification, and final dosage formation., *Angew. Chem. Int. Ed. Engl.* 52 (2013) 12359–63.
- [2] K. Järvinen, W. Hoehe, M. Järvinen, S. Poutiainen, M. Juuti, S. Borchert, In-line monitoring of the drug content of powder mixtures and tablets by near-infrared spectroscopy during the continuous direct compression tableting process, *Eur. J. Pharm. Sci.* 48 (2013) 680–688.
- [3] G. Vetter, *Dosing Handbook*, 1st editio, Elsevier Advanced Technology, 1998.
- [4] W.E. Engisch, F.J. Muzzio, Method for characterization of loss-in-weight feeder equipment, *Powder Technol.* 228 (2012) 395–403.
- [5] E. Teruel, I. Ramos, M. Gil, Pulverised fuel feeding for co-firing based on loss-in-weight flow metering, *Biomass and Bioenergy.* 39 (2012) 403–412.
- [6] G. Loria, G. Vassura, *Opere di Evangelista Torricelli*, 1919.
- [7] W.A. Beverloo, L.A. Leniger, J. van de Velde, The flow of granular solids through orifices, *Chem. Eng. Sci.* 15 (1961) 260–269.
- [8] J.E. Hilton, P.W. Cleary, Granular flow during hopper discharge, *Phys. Rev. E.* 84 (2011) 011307.
- [9] L. Staron, P. Lagrée, S. Popinet, P. Lagr, The granular silo as a continuum plastic flow : The hour-glass vs the clepsydra The granular silo as a continuum plastic flow : The hour-glass vs the clepsydra, 103301 (2012).
- [10] S. Chialvo, S. Sundaresan, A modified kinetic theory for frictional granular flows in dense and dilute regimes, *Phys. Fluids.* 25 (2013) 070603.
- [11] Y. Gu, S. Chialvo, S. Sundaresan, Rheology of cohesive granular materials across multiple dense-flow regimes, *Phys. Rev. E.* 90 (2014) 032206.
- [12] S. Chialvo, J. Sun, S. Sundaresan, Bridging the rheology of granular flows in three regimes, *Phys. Rev. E.* 85 (2012) 021305.
- [13] P. Jop, Y. Forterre, O. Pouliquen, A constitutive law for dense granular flows., *Nature.* 441 (2006) 727–30.
- [14] X. Cheng, G. Varas, D. Citron, H. Jaeger, S. Nagel, Collective Behavior in a Granular Jet: Emergence of a Liquid with Zero Surface Tension, *Phys. Rev. Lett.* 99 (2007) 188001.
- [15] V. Vidyapati, S. Subramaniam, Granular Flow in Silo Discharge: Discrete Element Method Simulations and Model Assessment, *Ind. Eng. Chem. Res.* 52 (2013) 13171–13182.

- [16] B.N. Asmar, P. a. Langston, a. J. Matchett, J.K. Walters, Validation tests on a distinct element model of vibrating cohesive particle systems, *Comput. Chem. Eng.* 26 (2002) 785–802.
- [17] D. Geldart, Types of Gas Fluidization, *Powder Technol.* 7 (1973) 285–292.
- [18] J.R. van Ommen, J. Nijenhuis, C.M. van den Bleek, M.-O. Coppens, Four Ways To Introduce Structure in Fluidized Bed Reactors, *Ind. Eng. Chem. Res.* 46 (2007) 4236–4244.
- [19] I. Aranson, L. Tsimring, Patterns and collective behavior in granular media: Theoretical concepts, *Rev. Mod. Phys.* 78 (2006) 641–692.
- [20] A. Kudrolli, Size separation in vibrated granular matter, *Reports Prog. Phys.* 67 (2004) 209–247.
- [21] C.. Tai, S.. Hsiau, Dynamic behaviors of powders in a vibrating bed, *Powder Technol.* 139 (2004) 221–232.
- [22] P. Eshuis, K. van der Weele, D. van der Meer, R. Bos, D. Lohse, Phase Diagram of Vertically Shaken Granular Matter, *Phys. Fluids.* 19 (2008) :123301.
- [23] P. Eshuis, D. van der Meer, M. Alam, H.J. van Gerner, K. van der Weele, D. Lohse, Onset of convection in strongly shaken granular matter., *Phys. Rev. Lett.* 104 (2010) 038001.
- [24] E. Bodenschatz, W. Pesch, G. Ahlers, Recent Developments in Rayleigh-Bénard Convection, (2000) 709–778.
- [25] I. Goldhirsch, Rapid granular flows, *Annu. Rev. Fluid Mech.* 35 (2003) 267–293.
- [26] S.-S. Hsiau, C.-C. Liao, P.-Y. Sheng, S.-C. Tai, Experimental study on the influence of bed height on convection cell formation, *Exp. Fluids.* 51 (2011) 795–800.
- [27] B.P. Tighe, M. Sperl, Pressure and motion of dry sand: translation of Hagen’s paper from 1852, *Granul. Matter.* 9 (2007) 141–144.
- [28] A. Medina, D. Cabrera, A. López-Villa, M. Pliego, Discharge rates of dry granular material from bins with lateral exit holes, *Powder Technol.* 253 (2013) 270–275.
- [29] C. Mankoc, a. Janda, R. Arévalo, J.M. Pastor, I. Zuriguel, a. Garcimartín, et al., The flow rate of granular materials through an orifice, *Granul. Matter.* 9 (2007) 407–414.
- [30] M. Sperl, Experiments on corn pressure in silo cells – translation and comment of Janssen’s paper from 1895, *Granul. Matter.* 8 (2005) 59–65.
- [31] M.A. Aguirre, J.G. Grande, A. Calvo, L. a. Pugnaroni, J.-C. Géminard, Granular flow through an aperture: Pressure and flow rate are independent, *Phys. Rev. E.* 83 (2011) 061305.

- [32] C. Perge, M.A. Aguirre, P.A. Gago, L. a. Pughaloni, D. Le Tourneau, J.-C. Géminard, Evolution of pressure profiles during the discharge of a silo, *Phys. Rev. E.* 85 (2012) 021303.
- [33] D. Schulze, *Pulver und Schüttgüter*, Springer Berlin Heidelberg, 2006.
- [34] H.G. Sheldon, D.J. Durian, Granular discharge and clogging for tilted hoppers, *Granul. Matter.* 12 (2010) 579–585.
- [35] I.I. Bagrintsev, Investigation of the outflow of granular materials through openings in the wall of a vertical cylindrical tube, *Chem. Pet. Eng.* (1977) 12–13.
- [36] C.R. Wassgren, M.L. Hunt, P.J. Freese, J. Palamara, C.E. Brennen, Effects of vertical vibration on hopper flows of granular material, *Phys. Fluids.* 14 (2002) 3439.
- [37] H. Pacheco-Martinez, H.J. van Gerner, J.C. Ruiz-Suárez, Storage and discharge of a granular fluid, *Phys. Rev. E.* 77 (2008) 021303.
- [38] B.D. Storey, Analysis of a draining tank, (2006) 1–4.
- [39] S.P. C. Kloss, C. Goniva, A. Hager, S. Amberger, Models, algorithms and validation for opensource DEM and CFD-DEM, *Prog. Comput. Fluid Dyn. Int. J.* 12 (2012) 140 – 152.
- [40] J. Sun, S. Sundaresan, A constitutive model with microstructure evolution for flow of rate-independent granular materials, *J. Fluid Mech.* 682 (2011) 590–616.
- [41] W.C. Oliver, G.M. Pharr, An improve technique for determining hardness elastic modulus using load displacement sensing indentation experiments, *J.Mater R.* 7 (1992) 1564–1583.
- [42] T.W. Martin, J.M. Huntley, R.D. Wildman, Hydrodynamic model for a vibrofluidized granular bed, *J. Fluid Mech.* 535 (2005) 325–345.
- [43] S. Radl, *Modeling of Multiphase Systems in Pharmaceutical Applications*, Graz University of Technology, 2010.
- [44] MIT Material Property Database, (n.d.).
- [45] S. Luding, Introduction to Discrete Element Methods Basics of Contact Force Models and how to perform the Micro-Macro Transition to Continuum Theory, (2008) 785–826.
- [46] T. Schwager, T. Pöschel, Coefficient of restitution and linear–dashpot model revisited, *Granul. Matter.* 9 (2007) 465–469.

9 Appendix A - Simulation

9.1 Discrete Element Method (DEM) [39,45]

The basic concept of DEM is to calculate the trajectory of each particle in the simulation directly using Newton's equation of translational and rotational motion:

$$m_i \frac{d^2}{dt^2} \mathbf{r}_i = \mathbf{f}_i + m_i \mathbf{g} \text{ and } I_i \frac{d}{dt} \boldsymbol{\omega}_i = \mathbf{t}_i \quad 9.1$$

Here m_i denotes for the mass of particle i , \mathbf{r}_i its position, $\mathbf{f}_i = \sum_c \mathbf{f}_i^c$ the total force acting on the particle due to the collisions with other particles and walls, \mathbf{g}_i for acceleration like gravity, I_i for the particle's moment of inertia, $\boldsymbol{\omega}_i$ for the angular velocity and \mathbf{t}_i for the total torque.

For calculating the contact forces due to collisions a linear spring dashpot model is used. The key assumption of this model is that repulsive particle-particle and particle-wall forces are proportional to an (virtual) overlap δ of the particles (or the particle and the wall). This (virtual) overlap replaces the deformation of the particles, which would happen in reality. The total force of the model can be decomposed to a normal and a tangential force:

$$\delta = r_i + r_j - |\mathbf{r}_i - \mathbf{r}_j| \quad 9.2$$

$$\mathbf{f} = \mathbf{f}_n + \mathbf{f}_t \quad 9.3$$

$$\mathbf{f}_n = (k_n \delta \mathbf{n}_{ji} - \gamma_n \mathbf{v} n_{ij}) \quad 9.4$$

$$\mathbf{f}_t = (k_t \delta \mathbf{t}_{ji} - \gamma_t \mathbf{v} t_{ij}) \quad 9.5$$

In this equations δ is standing for the overlap of the particles i and j obtained from their radius r and their positions \mathbf{r} , the indices n and t are standing for normal and tangential directions, k denotes the spring stiffness, γ the viscous damping coefficient, \mathbf{v} the particle's velocity, \mathbf{n}_{ij} is the normal vector and \mathbf{t}_{ij} the tangential vector. The linear spring dashpot model gives a very simplified illustration of colliding particles and even can lead to an artificial

issue: at some points during the end of a particle collision, attractive forces between the two particles would occur. Therefore an additional lower bound is needed which sets $\mathbf{f} = \mathbf{0}$ if the original calculated \mathbf{f} falls below zero [46].

To satisfy the Coulomb's friction criteria the following equation has to be fulfilled.

$$|\mathbf{f}_t| < \mu |\mathbf{f}_n| \quad 9.6$$

The stiffness and damping coefficients are calculated from material properties using the following equations.

$$k_n = \frac{16}{15} \sqrt{r_{eff}} Y_{eff} \left[\frac{15 m_{eff} v_{char}^2}{16 \sqrt{r_{eff}} Y_{eff}} \right]^{1/5} \quad \text{and} \quad k_t = k_n \frac{2}{7} \quad 9.7$$

$$\gamma_n = \frac{4 m_{eff} k_n}{\sqrt{1 + \left(\frac{\pi}{\ln(e_n)} \right)}} \quad \text{and} \quad \gamma_t = \gamma_n \quad 9.8$$

Y denotes the Young's modulus, v_{char} a characteristic velocity and e_n the coefficient of restitution. The index *eff* stands for effective properties calculated as follows.

$$m_{eff} = m_i m_j / (m_i + m_j) \quad 9.9$$

$$r_{eff} = r_i r_j / (r_i + r_j) \quad 9.10$$

$$1/Y_{eff} = \frac{(1 - v_1^2)}{Y_1} + \frac{(1 - v_2^2)}{Y_2} \quad 9.11$$

The application of this linear spring dashpot models allows calculating typical contact duration of a collision as the half period of an oscillation of the analogue damped harmonic oscillator.

$$t_c = \pi / \omega_{DEM} \quad \text{and} \quad \omega_{DEM} = \sqrt{\left(k_n / m_{eff} \right) - \left(\gamma_n / (2 m_{eff}) \right)^2} \quad 9.12$$

t_c is the contact time of a collision and ω is the eigenfrequency of the contact. This contact time is from practical importance since is it used to obtain a certain simulation time step size.

Typically for the time step size a value of $t_c/50$ is used to be able to get a necessary resolution of collision events and obtain a stable simulation.

9.2 LIGGGHTS Setup

The different geometries were constructed in *Inventor*® and saved as .stl files. Some necessary surface manipulations were done using *Cubit*®. The main dimensions are reported in Section 10.2.

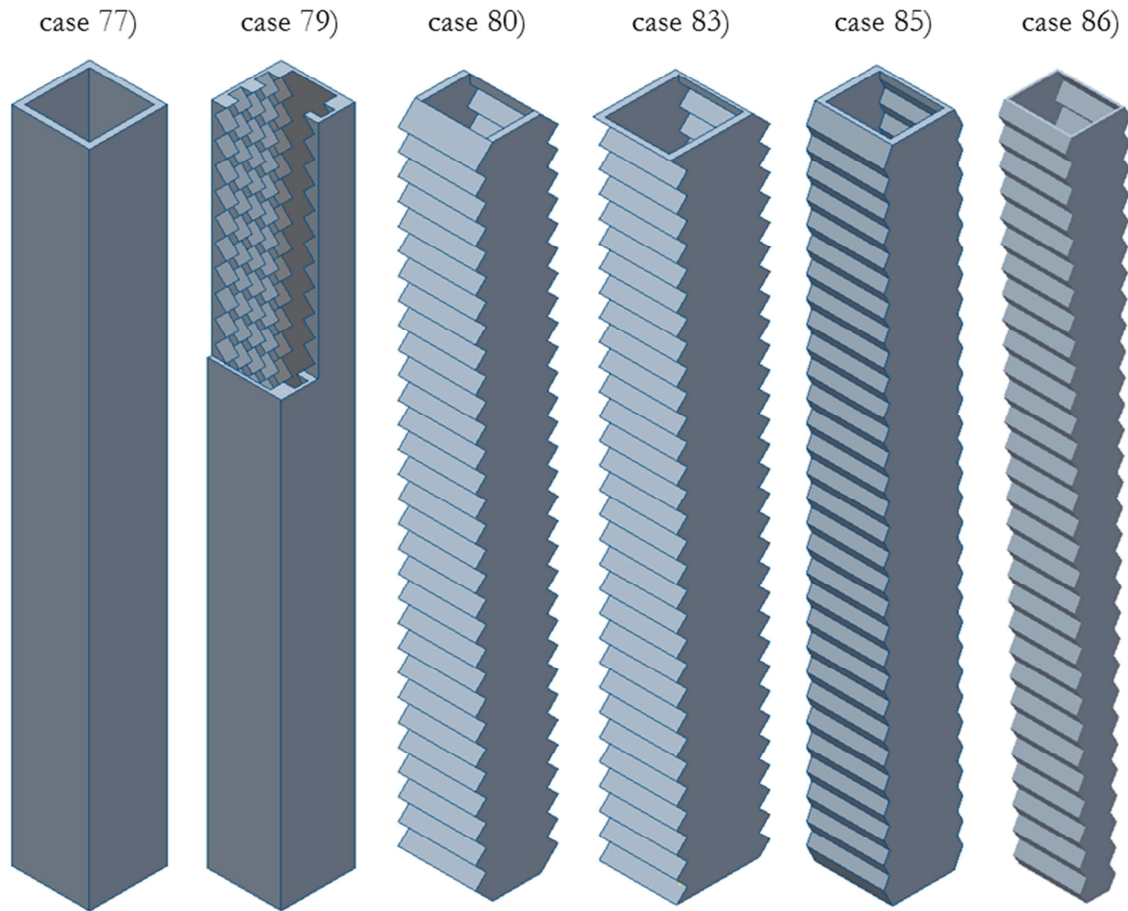


Figure 33: Different bin designs for simulations

The simulation uses a slight particle size distribution according to the particles used in the experiment (see Section 10.1). An example of an input script for particle distribution generation (for each geometry one particle configuration; particles are dropped into the geometry) is shown below.

```

#Insert Particles

fix pts1 all particletemplate/sphere 1 atom_type 1 density constant ${rhoP} radius
constant ${radiusP1}
fix pts2 all particletemplate/sphere 1 atom_type 1 density constant ${rhoP} radius
constant ${radiusP2}
fix pts3 all particletemplate/sphere 1 atom_type 1 density constant ${rhoP} radius
constant ${radiusP3}
fix pts4 all particletemplate/sphere 1 atom_type 2 density constant ${rhoP} radius
constant ${radiusP4}
fix pts5 all particletemplate/sphere 1 atom_type 2 density constant ${rhoP} radius
constant ${radiusP5}
fix pdd1 all particledistribution/discrete 1 5 pts1 0.0736 pts2 0.2371 pts3 0.3327 pts4
0.2671 pts5 0.0895

region insReg block -0.0149 0.0149 -0.009 0.0149 0.001 0.70 units box
fix ins all insert/pack seed 100001 distributiontemplate pdd1 vel constant 0. 0. -1.00 &
insert_every once overlapcheck yes all_in yes volumefraction_region 0.275 region
insReg

```

The main data generated by the simulations is listed below:

- A report of mass and particle number development, maximum overlap for the current time step, the center of mass for the classes of the three smaller particle sizes and the classes of the two biggest particle sizes to investigate the segregation are stored in txt. file.
- In a spatial averaging procedure the particle bed is divided into small spatial slices. For each slice the sum of the contact pressure of the particles in the three main directions and the number of particles in the slice is calculated and reported.
- For visualization, checking and detail observations additional the particle information was also saved in dump files for later examination with *Paraview*®

Depending on the goal of the simulation, whether a full run simulation with discharge of particles or only a pressure analysis over the height of the particle bed, the output of the simulation was varied in the sake of data management.

An example of an input script for LIGGGHTS is shown below.

```

#-----<Vibrating Powder Feeder>-----
#-----<    © Gerald Reif    >-----
#-----<        2014        >-----
#-----<    MAIN SCRIPT    >-----

#-----Input Parameters-----

variable timeStep equal 1.6e-7
variable frequ equal 25. #[Hz] frequency of shaking
variable accel equal 5. #[g] acceleration of shaking
variable SampleStep equal 31250 #Number of Steps for taking a sample

variable oscillationPeriod equal 1./${frequ} #shaking period for one oscillation
variable amplitude equal ${accel}*9.81/(2.*PI*${frequ})^2. #shaking amplitude

#Young's moduli
variable Yglass equal 7e9
variable Ypmma equal ${Yglass}/28.
#Poisson ratios
variable Nuglass equal 0.23
variable Nupmma equal 0.4
#Coef. of restitution
variable Epgg equal 0.91
variable Epgp equal 0.68
variable Eppp equal 0.68
#Coef. of friction
variable Frgg equal 0.09
variable Frgp equal 0.11
variable Frpp equal 0.15

#-----General Settings for Granular Systems-----
atom_style granular
atom_modify map array
boundary f f f
newton off
communicate single vel yes
units si

#-----Region/Simulationbox Definition and ReadIn Particle Data-----
region reg block -0.016 0.016 -0.016 0.0325 -0.003 0.303 units box
#create_box 3 reg #keep outcommented
read_data particle.data

```

```

group smallPart type 1
group largePart type 2

neighbor      0.00005 bin #skin distance: 10%-20% of r_particle
neigh_modify  delay 0

#-----Material Properties-----
fix m1 all property/global youngsModulus peratomtype ${Yglass} ${Yglass} ${Ypmma}
fix m2 all property/global poissonsRatio peratomtype ${Nuglass} ${Nuglass} ${Nupmma}
fix m3 all property/global coefficientRestitution peratomtypepair 3 ${Epgg} ${Epgg}
    ${Epgp} ${Epgg} ${Epgg} ${Epgp} ${Epgp} ${Epgp} ${Eppp}
fix m4 all property/global coefficientFriction peratomtypepair 3 ${Frgg} ${Frgg} ${Frgp}
    ${Frgg} ${Frgg} ${Frgp} ${Frgp} ${Frgp} ${Frgp}
fix m5 all property/global characteristicVelocity scalar 1 #standard 1

#-----Pair Style and Geometry Insertion-----
pair_style gran model hooke tangential history limitForce 'on' ktToKnUser 'on'
pair_coeff * *
timestep ${timeStep}

fix gravi all gravity 9.81 vector 0.0 0.0 -1.0

#load geometry
fix cad all mesh/surface file Bin_long_outlet_closed.stl type 3 scale 1 curvature 1e-5
fix wall1 all wall/gran model hooke tangential history mesh n_meshes 1 meshes cad &
    limitForce 'on' ktToKnUser 'on'
#front plane to close outlet
fix wall2 all wall/gran model hooke tangential history primitive type 3 yplane 0.025

#-----Computes, Output Variables-----
#Energy
compute rke all erotate/sphere

#Total mass and number of particles
compute PartMass all property/atom mass
compute totalMass all reduce sum c_PartMass
variable totalMassVar equal c_totalMass
variable currAtom equal atoms

#Overlap
compute PartDia all property/atom diameter
compute minPartDia all reduce min c_PartDia

```

```

compute      myPair all pair/local dist
compute      myPairMin all reduce min c_myPair
variable     maxoverlap equal ((1.)-c_myPairMin/(c_minPartDia))*100.

#Timestep
variable     time equal step*${timeStep}
variable     simstepequal step

#Contact Stress
compute      myStressContact all stress/atom pair bond
compute      pContact all reduce sum c_myStressContact[1] c_myStressContact[2]
              c_myStressContact[3]

#Center of mass
variable     zpos atom mass*z
variable     cm atom mass
compute      zsall1 smallPart reduce/region reg sum v_zpos
compute      msall1 smallPart reduce/region reg sum v_cm
variable     regionMassall1 equal c_msall1
variable     ymeanall1 equal c_zsall1/(c_msall1+1e-30) #center of small particles
compute      zsall2 largePart reduce/region reg sum v_zpos
compute      msall2 largePart reduce/region reg sum v_cm
variable     regionMassall2 equal c_msall2
variable     ymeanall2 equal c_zsall2/(c_msall2+1e-30) #center of big particles

#-----Thermo-----
fix          integr all nve/sphere #apply nve integration to all particles
thermo_style custom step v_time atoms ke c_rke c_totalMass v_maxoverlap
thermo      1000
thermo_modify lost ignore norm no

#-----Write Output Files-----
run 1 #insert the first particles so that dump is not empty
dump dmp all custom 6250000 post/dump*.vib_bin id id type diameter density x y z vx vy
      vz fx fy fz omegax omegay omegaz #dump particle data
dump stl1 all mesh/stl 6250000 post/bin*.stl cad #dump geometry

```

```

#write report of data to .txt file
fix    report all print  ${SampleStep}  "${time}  ${simstep}  ${currAtom}  ${totalMassVar}
      ${maxoverlap}  ${regionMassall1}  ${ymeanall1}  ${regionMassall2}  ${ymeanall2}
      ${oscillationPeriod}  ${amplitude}" file 42_report.txt title "time simstep np
      totalmass maxoverlap massSmall zcomSmall massLarge zcomLarge oscPeriod amplitude"
      screen no

#write report of contact pressure and filling level to .txt file
fix    averseport all ave/spatial 1 1  ${SampleStep}  z 0.0 0.001 c_myStressContact[1]
      c_myStressContact[2] c_myStressContact[3] file 42_rep_avepress.txt units box

#-----Simulation Sequence-----
#Generate vibrated bed
fix    move1 all move/mesh mesh cad wiggle amplitude 0.00 0.00  ${amplitude} period
      ${oscillationPeriod}

run    6250000 upto # shake one second
unfix  wall2 # open outlet
run    256250000 upto #discharge particles

```

For analyses of volume fraction per layer, similar to the contact pressure calculation, an additional fix was used, reporting the data in .vtk files.

```

#Averaging fix void fraction
fix    pic all ave/pic nevery 2000 cell_size_relative 0.5 alphaScaling 1.0 &
      mapping 2 1.0 interpolation 1 interpolationVMean 1 &
      forceBinDir 0 0 1 cellVolumeUser 6.62018768674699E-07 &
      stencil 3

dump   dmpPic all pic/vtk 2000 postPic/dump_pic*.vtk isGlobal 1 writeFluct 1

```

The dump files with the particle data were converted to .vtk files by using the program *LPP* (LIGGGHTS post-processing). The .vtk files were analyzed by using *ParaView*® *v4.1* or *Matlab*®. The report .txt files were post processed with *Matlab*®.

9.3 Post Processing with Matlab

The whole analyzing software consists of several functions. The first function reads in the report and spatial average files. From the spatial average data the height data gets extracted and transferred from the LIGGGHTS global coordinate system to a coordinate system located at the bin bottom. Further from the spatial average data the mean pressure for each slice gets calculated using:

$$p = \frac{\overline{p_{pair,x}} + \overline{p_{pair,y}} + \overline{p_{pair,z}}}{3V_{slice}} n_p \quad 9.13$$

Here p is the pressure in the examined slice, $\overline{p_{pair,x-y-z}}$ is the mean pressure over all particles in x,y,z-direction gained from the simulation, n_p is the number of particles in the slice and V_{slice} is the volume in the slice (calculated from shape functions for each bin). Performing this calculation over all slices, one ends up with a pressure profile over height.

Moreover the bulk density ρ_b and quasi hydrostatic pressure p_{hydro} in quiescent condition get calculated from:

$$\rho_b = \frac{m_0}{V_0} \quad 9.14$$

$$p_{hydro} = \rho_b g h_0 \quad 9.15$$

Here m_0 is the mass of particles, h_0 the filling height and V_0 the volume of the bin filled with particles at the start.

Also some general information as maximum overlap, time step sizes and runtime is calculated.

```
function [results]=postpro(cano,input)
% ***** Graz University of Technology *****
% copyright: Gerald Reif, 2014.3.25.
% % ***** Graz University of Technology *****

% DESCRIPTION:
% Function for postprocessing for LIGGGHTS simulation
%
%input: cano...casenumber as string
%       input...general data
%       input.ampli...           %[m]
%       input.osc_period...     %[s]
%       input.a_bin...          %[m] lenght of bin's side
%       input.d_out...          %[m] outlet diamentor of bin
%       input.height_out...     %[m] height of center of outlet hole
%       input.d_part...         %[m] particle diameter
%       input.rho_part...       %[kg/m3] particle density
%       input.ss_vibstart...    %simulationstep at which vibrating start
%       input.ss_dcstart...     %simulationstep at which discharge start
```

```

%% Reading data:

% read report.txt
report_in=readreport([cano 'ol_report.txt']);
delta_tsim=report_in.time(1)/report_in.simstep(1);   %[s] stepsize of time
in simulation
delta_ss_rep=report_in.simstep(1);                 %[s] stepsize of
getting data out of simulation
ss_vibstart_rep=input.ss_vibstart/delta_ss_rep;    %[s] simulationstep
of vibrationstart
ss_dcstart_rep=input.ss_dcstart/delta_ss_rep;     %[s] simulationstep
of dischargestart

% read avespatial.txt
press_in=readAveSpatial([cano 'ol_rep_avepress.txt']);
    delta_ss_p=press_in.simstep{1};

%% height correction/analyses
cor_h=0; %prevalue
for i=1:length(press_in.simstep)

tempo=find(press_in.rawDat{i}(:,3), 1, 'last');

    for j=tempo:-1:1
        if press_in.rawDat{i}(j,3) > 150 %finding height of "dense" bed->
ca. 25% of dense packing
            if press_in.simstep{i} >= input.ss_vibstart
                cor_h=input.ampli*sin(2*pi/input.osc_period*(press_in.simstep{i}-
input.ss_vibstart)*delta_tsim); %correction height due to
                oscillations
            end
height.cor(i,:)=[delta_tsim*press_in.simstep{i},press_in.rawDat{i}(j,2)-
cor_h]; %corrected: height from the bottom of the bin to bed height

height.uncor(i,:)=[delta_tsim*press_in.simstep{i},press_in.rawDat{i}(j,2)
]; %uncorrected: height from the bottom of the bin to bed height
        break
    end
    height.cor(i,:)=[delta_tsim*press_in.simstep{i},0];
    height.uncor(i,:)=[delta_tsim*press_in.simstep{i},0];
end

end

height.start=height.uncor(ss_vibstart_rep,2); %starting height before
vibrating

%% pressure data processing

delta_h= press_in.rawDat{1}(2,2)-press_in.rawDat{1}(1,2);
no_bins= length(press_in.rawDat{1});

%Calculating total pressure per bin and timestep

cor_h=0; %correction of height due to oscillations

```

```

for i=1:length(press_in.rawDat);
    press.contact{i}=[no_bins,2];    %property matrix
    press.time(i)=delta_tsim*press_in.simstep{i};

    if press_in.simstep{i} >= input.ss_vibstart
        cor_h=input.ampli*sin(2*pi/input.osc_period*(press_in.simstep{i}-
input.ss_vibstart)*delta_tsim); %correction height due to oscillations
    end

    for j=1:no_bins;
        [bin_area,bin_volume]=shape_funct(input.bin_shape,(j-
1)*delta_h+delta_h/2-cor_h);
        vol_element=delta_h*bin_area;
        tempo=sum(abs(press_in.rawDat{i}(j,4:6)))*press_in.rawDat{i}(j,3)
        /(3*vol_element); %pressure calculation for each bin

        press.contact{i}(j,:)=[press_in.rawDat{i}(j,2)-cor_h,tempo];
        %pressure at corrected height
    end
end

end

%% general analyses:

[max_ol,max_ol_i]=max(report_in.maxoverlap(ss_vibstart_rep:end)); %max
overlap during vibration period
j=0;
sum_ol=0;
for i=ss_vibstart_rep:length(report_in.maxoverlap)
if report_in.maxoverlap(i) > 0
    sum_ol=sum_ol+report_in.maxoverlap(i);
    j=j+1;
end
end
mean_ol=sum_ol/j; %mean max overlap during vibration period
rho_bulk= report_in.totalmass(1)/bin_volume); %bulk density at start
p_hydro=rho_bulk*height.start*9.81;

%% writing result cell

%output of important time- and simulationsteps
results.delta_tsim=delta_tsim;
results.delta_ss_rep=delta_ss_rep;
results.ss_vibstart_rep=ss_vibstart_rep;
results.ss_dcstart_rep=ss_dcstart_rep;

%output data
results.overlap=[max_ol, mean_ol];
results.press=press;
results.report_in=report_in;
results.height=height;
results.rho_bulk=rho_bulk;
results.p_hydro=p_hydro;

end

```

For the calculation of bin areas and volumes at certain heights, shape functions for each bin were set up and compromised in the following function.

```
function [bin_area,bin_volume]=shape_funct(bin_shape,h)

% ***** Graz University of Technology *****
% copyright: Gerald Reif, 2014.9.13.
% ***** Graz University of Technology *****
%
%function for calculating cross area and bin volume for different bin
shapes at specific height
%
%input:
%   bin_shape... [] 1...straight, 2...zickzack, 3...shifted zickzack,
%                   4...zickzick, 5...flat zickzack, 6_cone_zickzack
%   h...         [m] height
%
%output: bin_area...      [m^2] area at height h
%        bin_volume...   [m^3] area at height h

i=0;
if bin_shape == 1;
    a=0.03;    %[m]
    bin_area = a^2;
    bin_volume = a^2*h;
end

if bin_shape == 2;
    a=0.03;    %[m]
    h_s=0.01; %[m]
    s=0.005;  %[m]
    while h>=h_s
        h=h-h_s;
        i=i+1;
    end
    bin_area=2*a*s/(-h_s/2)*abs(h-h_s/2)+a^2;
    vol_section=a^2*h-a*((2*h-h_s)*abs(2*h-h_s)+h_s*abs(h_s))*s/(2*h_s);
    bin_volume=i*h_s*(a-s)*a+vol_section;
end

if bin_shape == 3;
    a_s=0.006; %[m]
    a=0.03;    %[m]
    h_s=0.01; %[m]
    s=0.005;  %[m]
    while h>=h_s
        h=h-h_s;
        i=i+1;
    end
    bin_area=0.00078+2*a_s*s/(-h_s/2)*abs(h-h_s/2);
    vol_section=a^2*h-a*((2*h-h_s)*abs(2*h-h_s)+h_s*abs(h_s))*s/(2*h_s);
    bin_volume=i*h_s*(a-s)*a+vol_section;
end

if bin_shape == 4;
    bin_area = 0.0009;
    bin_volume = bin_area*h;
end
```

```

if bin_shape == 5;
    a=0.03;    %[m]
    h_s=0.01; %[m]
    s=0.003;  %[m]
    while h>=h_s
        h=h-h_s;
        i=i+1;
    end
    bin_area=2*a*s/(-h_s/2)*abs(h-h_s/2)+a^2;
    vol_section=a^2*h-a*((2*h-h_s)*abs(2*h-h_s)+h_s*abs(h_s))*s/(2*h_s);
    bin_volume=i*h_s*(a-s)*a+vol_section;
end

if bin_shape == 6;
    a=0.03;    %[m]
    h_s=0.01; %[m]
    s=0.003;  %[m]
    h_r=h;
    while h>=h_s
        h=h-h_s;
        i=i+1;
    end
    bin_area=2*a*s/(-h_s/2)*abs(h-h_s/2)+a^2+(h_r*(0.007/0.300)-
0.0075)*a^2;
    vol_section=a^2*h-a*((2*h-h_s)*abs(2*h-h_s)+h_s*abs(h_s))*s/(2*h_s);
    bin_volume=i*h_s*(a-s)*a+vol_section;
end
end
end

```

In the main program the previous shown function for read in and manipulate the raw files get called and the gained data is processed and plotted. Also a function for providing a video of the animated pressure profile was implemented. The program is shown below.

```

% ***** Graz University of Technology *****
% copyright: Gerald Reif, 2014.2.25.
% % ***** Graz University of Technology *****

% DESCRIPTION:
% Post processing for LIGGGHTS simulation
%
%input: casenumber; report files in same folder

%output:  graphs of discharge, mass flow and bed height development

close all
clear all
clc

%% General Input and Reading data:

cn=[11];%

i=0;
i=i+1;
input{cn(i)}.ampli=0.001989; %[m]
input{cn(i)}.osc_period=0.04; %[s]
input{cn(i)}.a_bin=0.03; %[m] lenght of bin's side
input{cn(i)}.d_out=0.01; %[m] outlet diamenters of bin

```

```

input{cn(i)}.height_out=0.005; %[m] height of center of outlet hole
input{cn(i)}.d_part=0.00122265; %[m]mean particle diameter
input{cn(i)}.rho_part=2500; %kg/m3 particle density
input{cn(i)}.ss_vibstart=5000; %simulationstep at which vibrating start
input{cn(i)}.ss_dcstart=1000000; %simulationstep at which discharge
starts
input{cn(i)}.bin_shape=1; %bin shape: 1...straight, 2...zickzack,
3...shifted zickzack
caseno{cn(i)}=postpro(num2str(cn(1)),input{cn(i)}); %getting data of
files
plotprop{cn(i)}=[1 0 0];

fontSizeTitle=12;
fontSizeAxis=11;
fontSizeLeg=11;
fontSizeLabel=8;
markerSize = 9;
lineWidth=1;
mark={'o','s','d','^','v','x','o','s','d','^','v','x','o','s','d','^','v',
,'x','o','s','d'};

pa=[0.1800    0.1500    0.750    0.790];
str='';
for i=1:length(cn)
    str=[str,'_',num2str(cn(i))];
end

%% discharge analyses

% plot totalmass over time
figure(1)
set(gcf,'Color',[1 1 1])
set(gcf, 'Units','centimeters', 'Position',[10 10 8 7])
hold on
grid off
box on

n=10;

for i=1:length(cn),

M_n = round(linspace(caseno{cn(i)}.ss_dcstart_rep,
numel(caseno{cn(i)}.report_in.totalmass),n)); % indices of markers

p1(i)=plot(caseno{cn(i)}.report_in.time(caseno{cn(i)}.ss_dcstart_rep:end)
-1,caseno{cn(i)}.report_in.totalmass(caseno{cn(i)}.ss_dcstart_rep:end)/
caseno{cn(i)}.report_in.totalmass(caseno{cn(i)}.ss_dcstart_rep),'color',p
lotprop{cn(i)}); %mass of particles in bin normalized with m_start over
time

p1(i)=plot(caseno{cn(i)}.report_in.time(M_n)-
1,caseno{cn(i)}.report_in.totalmass(M_n)/caseno{cn(i)}.report_in.totalmas
s(caseno{cn(i)}.ss_dcstart_rep),mark{i},'color',plotprop{cn(i)},'markersi
ze',5, 'MarkerFaceColor',plotprop{cn(i)}); %mass of particles in bin
normalized with m_start over time

```

```

p1(i)=plot(caseno{cn(i)}.report_in.time(M_n(1))-
1,caseno{cn(i)}.report_in.totalmass(M_n(1))/caseno{cn(i)}.report_in.total
mass(caseno{cn(i)}.ss_dcstart_rep),'color',plotprop{cn(i)},'marker',mark{
i},'markersize',5,'MarkerFaceColor',plotprop{cn(i)}); %mass of particles
in bin normalized with m_start over time

list{i}=['case:', num2str(cn(i))];
end
% title('mass over time')
xlabel('$time
[s]$', 'interpreter', 'latex', 'FontName', 'Times', 'FontWeight', 'bold', 'fontsi
ze', fontSizeLabel)
ylabel('$m^{*} [-
]$', 'interpreter', 'latex', 'FontName', 'Times', 'FontWeight', 'bold', 'fontsi
ze', fontSizeLabel)
% p1=addmarkers(p1,20);
leg1=legend(p1,list,'FontName','Times','fontsize',fontSizeLeg);
legend 'boxoff'
axis([0 50 0 1])
axis 'auto x'
clear('list')
pa=[0.1700    0.1500    0.750    0.790];
set(gca, 'position',pa)
export_fig(['MassOverTime',str,'.tiff'],'-tif','-r600','-nocrop')
hold off

% call discharge analyses
for i=1:length(cn)

caseno{cn(i)}.dc_data=dcspan(caseno{cn(i)}.report_in,caseno{cn(i)}.ss_dcst
art_rep);
end

% call averaging massflow
for i=1:length(cn)
ave_ss=(1/caseno{cn(i)}.delta_tsim)/caseno{cn(i)}.delta_ss_rep; % e.g.
1[s]; averaging timestepsize

%averaging massflow
j=1;
for i=ss_dcstart_rep+no_avts:no_avts:length(report_in.totalmass)
    mf(j,:)= [report_in.time(i-no_avts/2), (report_in.totalmass(i-
no_avts)-report_in.totalmass(i))/(report_in.time(i)-report_in.time(i-
no_avts))]; %averaged massflow at certain time
    j=j+1;
end
end

% plot averaged massflow
figure(2)
set(gcf, 'Color',[1 1 1])
set(gcf, 'Units','centimeters', 'Position',[10 10 8 7])
box on
hold on
n=10;
for i=1:length(cn)
M_n = round(linspace(1,numel(caseno{cn(i)}.mf_ave)/2,n));

```

```

p2(i)=plot(caseno{cn(i)}.mf_ave(:,1)-
1,caseno{cn(i)}.mf_ave(:,2)/caseno{cn(i)}.dc_data.ave_dcrate,'color',plot
prop{cn(i)}); %averaged mass flow dimensionless!!!
p2(i)=plot(caseno{cn(i)}.mf_ave(M_n,1)-
1,caseno{cn(i)}.mf_ave(M_n,2)/caseno{cn(i)}.dc_data.ave_dcrate,mark{i},'c
olor',plotprop{cn(i)},'markersize',5, 'MarkerFaceColor',plotprop{cn(i)});
p2(i)=plot(caseno{cn(i)}.mf_ave(M_n(1),1)-
1,caseno{cn(i)}.mf_ave(M_n(1),2)/caseno{cn(i)}.dc_data.ave_dcrate,'color'
,plotprop{cn(i)},'marker',mark{i},'markersize',5,
'MarkerFaceColor',plotprop{cn(i)});

list{i}=['case:', num2str(cn(i))];
end
xlabel('$time
[s]$', 'interpreter', 'latex', 'FontName', 'Times', 'FontWeight', 'bold', 'fontsi
ze', fontSizeLabel)
ylabel('$\dot{m}^{*} \ [-
]$', 'interpreter', 'latex', 'fontsize', fontSizeLabel)
leg2=legend(p2,list,'FontName', 'Times', 'fontsize', fontSizeLeg);
legend 'boxoff'
axis([0 50 0 2])
axis 'auto x';
clear('list')
pa=[0.1700    0.1500    0.750    0.790];
set(gca, 'position',pa)
export_fig(['AveragedMassFlow',str,'.tiff'],'-tif','-r600','-nocrop')
hold off

%% height analyses

%plot corrected height
figure(3)
set(gcf,'Color',[1 1 1])
set(gcf, 'Units','centimeters', 'Position',[10 10 8 7])
box on
hold all
j=0;
i=0;

%plotting corrected height:
for i=1:length(cn)
    p3(i)=plot(caseno{cn(i)}.height.cor(:,1)-
1,caseno{cn(i)}.height.cor(:,2)/caseno{cn(i)}.height.cor(1,2),'color',plo
tprop{cn(i)}); %plotting absolut height of bedheight to bottom of bin
    list{i}=(['case:', num2str(cn(i))]);
end

% title('bed height over time')
xlabel('$time
[s]$', 'interpreter', 'latex', 'FontName', 'Times', 'FontWeight', 'bold', 'fontsi
ze', fontSizeLabel)
ylabel('$\{h\}^{*} \ [-
]$', 'interpreter', 'latex', 'FontName', 'Times', 'FontWeight', 'bold', 'fontsi
ze', fontSizeLabel)

leg3=legend(p3,list,'FontName', 'Times', 'fontsize', fontSizeLeg);
clear('list')
axis([0 50 0 1])
% axis 'auto x'
legend 'boxoff'

```

```

pa=[0.1700    0.1500    0.750    0.790];
set(gca, 'position',pa)
export_fig(['Height',str, '.tiff'],'-tif','-r600','-nocrop')
hold off

%% animated pressure profile

%anim_press(300,500,1,10,caseno,input,plotprop,[633,7812],0)

%% pressure profil averaged over time
ave_time=1; %0.24sec step number stop averaging

for i=1:length(cn)
ave_start=1; %step number start averaging
ave_stop=(ave_time/caseno{cn(i)}.delta_tsim)/caseno{cn(i)}.delta_ss_rep;
%0.24 sec step number stop averaging
caseno{cn(i)}.press_ave=press_ave(ave_start,ave_stop,caseno{cn(i)}.press)
end

figure(7)
set(gcf, 'Color',[1 1 1])
set(gcf, 'Units','centimeters', 'Position',[10 10 8 7])
box on
hold on

for i=1:length(cn)
j=0;
k=0;
for j=1:length(caseno{cn(i)}.press_ave(:,2))
if caseno{cn(i)}.press_ave(j,2)>1
break
end
end

for k=j:length(caseno{cn(i)}.press_ave(:,2))
if caseno{cn(i)}.press_ave(k,2)<5
break
end
end

n=10;
M_n=round(linspace(j,k,n));

p7(i)=plot(caseno{cn(i)}.press_ave(j:k,2)/(caseno{cn(i)}.p_hydro),caseno{
cn(i)}.press_ave(j:k,1)/caseno{cn(i)}.press_ave(k,1),'color',plotprop{cn(
i)});

p7(i)=plot(caseno{cn(i)}.press_ave(M_n,2)/(caseno{cn(i)}.p_hydro),caseno{
cn(i)}.press_ave(M_n,1)/caseno{cn(i)}.press_ave(k,1),mark{i},'color',plot
prop{cn(i)},'markersize',5, 'MarkerFaceColor',plotprop{cn(i)});

p7(i)=plot(caseno{cn(i)}.press_ave(M_n(1),2)/(caseno{cn(i)}.p_hydro),case
no{cn(i)}.press_ave(M_n(1),1)/caseno{cn(i)}.press_ave(k,1),'color',plotpr
op{cn(i)},'marker',mark{i},'markersize',5,
'MarkerFaceColor',plotprop{cn(i)});

list{i}=['case:', num2str(cn(i)), ' '];
end

```

```

xlabel('$\{p\}^{\{*\}} [-
]$', 'interpreter', 'latex', 'FontName', 'Times', 'fontsize', fontSizeLabel)
ylabel('$\{h\}^{\{*\}} [-
]$', 'interpreter', 'latex', 'FontName', 'Times', 'fontsize', fontSizeLabel)

leg7=legend(p7,list,'FontName','Times','fontsize',fontSizeLeg);
legend 'boxoff'
axis([0 1.2 0 1])
Ticks = 0:0.20:1.20;
set(gca, 'XTickMode', 'manual', 'XTick', Ticks, 'xlim', [0,1.20]);
% axis 'auto x'
clear('list')
pa=[0.1700    0.1500    0.750    0.790];
set(gca, 'position',pa)
% export_fig(['AveragedPressure',str,'.tiff'],'-tif','-r600','-nocrop')
hold off

%% Tor-Evaluation

for i=1:length(cn)

height{i}=smooth(smooth((caseno{cn(i)}.height.cor(1:end,2)),0.1,'loess'),
200);

A=0.01.^2*pi/4;
A_base=0.03.^2;
h0_s(i)=height{i}(1);

rho_s(i)=0.35/(0.03*0.03*h0_s(i));

mass{i}=smooth(smooth((caseno{cn(i)}.report_in.totalmass),0.1,'loess'),20
0);

m_p_2_2{i}=(sqrt(2*9.81*height{i})*0.01^2*pi()/4*rho_s(i));
torri_2_2{i}=-
(diff(mass{i})./diff(caseno{cn(i)}.report_in.time))./(m_p_2_2{i}(1:end-
1)));
end

figure(8)
set(gcf, 'Color',[1 1 1])
set(gcf, 'Units','centimeters', 'Position',[10 10 7.5 7])
box on
hold on

for i=1:length(cn)
    n=16
    M_n = round(linspace(1,numel(torri_2_2{i}),n));

p8(i)=plot(height{i}(1:end-
1)./height{1}(1),torri_2_2{i},'color',plotprop{cn(i)});
p8(i)=plot(height{i}(M_n)./height{1}(1),torri_2_2{i}(M_n),mark{i},'color'
,plotprop{cn(i)},'markersize',5, 'MarkerFaceColor',mfc);
p8(i)=plot(height{i}(M_n(1))./height{1}(1),torri_2_2{i}(M_n(1)), 'color',p
lotprop{cn(i)}, 'marker',mark{i}, 'markersize',5, 'MarkerFaceColor',mfc);
end

```

```

xlabel('${h}^{*} [-
]$', 'interpreter', 'latex', 'FontName', 'Times', 'fontsize', fontSizeLabel)
ylabel('${Tor} \ \ [-
]$', 'interpreter', 'latex', 'FontName', 'Times', 'fontsize', fontSizeLabel)
% $\frac{\dot{m}^{*}}{\dot{m}_{calc}^{*}} \ \ [-]$'

Ticks = 0.2:0.1:0.90;
set(gca, 'XTickMode', 'manual', 'XTick', Ticks, 'xlim', [0.2,0.9]);
Ticks = 0.0:0.01:2;
set(gca, 'YTickMode', 'manual', 'YTick', Ticks, 'ylim', [0.03,0.1]);
%axis 'auto x'
%axis 'auto y'
pa=[0.1750    0.1500    0.750    0.790];
% pa=[0.225    0.1590    0.7    0.7850];
set(gca, 'position',pa)
xlabh = get(gca, 'XLabel');
set(xlabh, 'Position', get(xlabh, 'Position') - [0 .0002 0]);

export_fig(['Sim_TorriVsHeight.tiff'], '-tif', '-r600', '-nocrop')

hold off

```

```

function
anim_press(ss_anim_start,ss_anim_stop,ssize_anim,fps,caseno,input,plotprop,ids,save)

% ***** Graz University of Technology *****
% copyright: Gerald Reif, 2014.4.09.
% ***** Graz University of Technology *****
%
%function for animate pressure profile

%input:
%   ss_anim_start...   [] simulationstep of animationstart
%   ss_anim_stop...   [] simulationstep of animationstop
%   ssize_anim...     stepsize of making frames
%   fps...            frames per second
%   press...          pressure data
%   saveavi...        0...no; >0..yes and is also is case number
%output: avi file of pressure profile

fig=figure;
scrsz = get(0, 'ScreenSize');
figure('Position',[scrsz(3)/4 scrsz(4)*0.1 scrsz(3)*0.3 scrsz(4)*0.8])

axes1 = axes('Position',[0.230588235294118 0.160714285714286
0.674411764705881 0.764285714285714]);

set(gcf, 'color', 'w');

set(gcf, 'PaperPositionMode', 'auto')
hold on

j=1;
for i=ss_anim_start:ssize_anim:ss_anim_stop %choose steps you want to
plot

```

```

    for k=1:length(ids)

p(k)=plot(caseno{ids(k)}.press.contact{i}(:,2)./caseno{ids(k)}.p_hydro,
caseno{ids(k)}.press.contact{i}(:,1),plotprop{ids(k)});
%./input{ids(k)}.d_part
    list{k}=['case:', num2str(ids(k))];
    hold on
    end
    hold off
xlabel('$$\frac{p}{p_{hydro,start}} \left[ \; \; \right]$$', 'interpreter', 'latex', 'FontName', 'Times', 'fontsize', 12)
ylabel('$$h \left[ \; \; \right]$$', 'interpreter', 'latex', 'FontName', 'Times', 'fontsize', 12)
axis([0 15 0 0.301])
leg=legend(p,list, 'interpreter', 'latex', 'FontName', 'Times', 'fontsize', 12,
'location', 'NorthEast');
title('Contact
Pressure', 'interpreter', 'latex', 'FontName', 'Times', 'fontsize', 12)
S=sprintf('Time: %.4f s',caseno{ids(1)}.press.time(i));
text(8.5,0.249,S, 'interpreter', 'latex', 'FontName', 'Times', 'fontsize', 12);
M(j)=getframe(gcf);
j=j+1;

end

close(fig)
str1='';
% numtimes=1;
% movie(M,numtimes,fps) %playmovie
if save == 1
    for i=1:length(ids)
        str1=[str1,num2str(ids(k)), '_'];
    end

movie2avi(M,[str1, 'pressure.avi'], 'FPS', fps, 'compression', 'none');
%save movie
end

end

```

Another script was programmed for the analyses of the .vtk files containing the volume fraction info. The program gives an averaged profile and as shown before an animated development of the volume fraction.

```

% ***** Graz University of Technology *****
% copyright: Gerald Reif, 2014.7.19.
% % ***** Graz University of Technology *****
% DESCRIPTION:
% Scrip for read in and analyzing .vtk files containing void fraction
info

clear all
clc
close all

cn=[623];%

i=0;

```

```

i=i+1;
input{cn(i)}.sim_ts=4E-7;      %timestep size of simulation
input{cn(i)}.sim_cap=2000;    %stepsize of capturing data
input{cn(i)}.ampli=0.001989; %[m]
input{cn(i)}.osc_period=0.04; %[s]
plotprop{cn(i)}=[1 0 0];

% Load postPic data into matlab
for i=1:length(cn)
cd(['postPic_' num2str(cn(i))])
files=dir('*.vtk');
n= length(files);

[vertex_t,vol_fract_t]=readvtk(files(1).name);
data_vtk.delta_hcell=abs(vertex_t(2,3)-vertex_t(1,3));

for j=1:n
temp_ss=strrep(files(j).name,'dump_pic','');
temp_ss=strrep(temp_ss,'.vtk','');
files(j).step=str2num(temp_ss);
end
start_data=min([files.step]);
step=start_data;

for j=1:n
index1=1;

while (files(index1).step == step)< 1
index1=index1+1;
end

temp_ss=files(index1).step;
temp_ss_ar(j)=(temp_ss);
temp_sim_time(j,1)=temp_ss_ar(j)*input{cn(i)}.sim_ts;

cor_h=input{cn(i)}.ampli*sin(2*pi/input{cn(i)}.osc_period*temp_sim_time(j)
));
[vertex,vol_fract]=readvtk(files(index1).name);

vertex(:,3)=vertex(:,3)-cor_h;
index=find(vol_fract,1,'first');
vertex(index,3)=(vertex(index,3)+data_vtk.delta_hcell/2)/2;
vol_fract(index)=vol_fract(index)/(vertex(index,3)*2)*data_vtk.delta_hcell;

for k=1:length(vertex(:,3))
if vertex(k,3) > 0
break
end
vertex(k,3)=0;
end

data_vtk.vol_fract{j}(:,1)=vertex(index:index+length(vertex(:,3))-12,3)';
%ADJUST to length of vtk subplus(vertex(:,3)');
data_vtk.vol_fract{j}(:,2)=vol_fract(index:index+length(vertex(:,3))-12)';

step=step+input{cn(i)}.sim_cap;
end

```

```

data_vtk.sim_step=temp_ss_ar';
data_vtk.sim_time=temp_sim_time;
end

cd ../
%save(['data_vtk' num2str(cn(i))'],'data_vtk')

%% Post Processing

mark={'o','s','d','^'};
fontSizeTitle=12;
fontSizeAxis=12;
fontSizeLeg=12;
fontSizeLabel=12;
markerSize = 9;
lineWidth=1;

list{1}='case 77';

%load(['data_vtk' num2str(cn(3))'],'data_vtk');
%data{cn(1)}=data_vtk;

data_vtk=data;

ss_start=1;
ss_stop=201;

no_ss=ss_stop-ss_start+1;

vol_fract_ave=cell2mat(vol_fract(ss_start));
for i=ss_start+1:ss_stop
vol_fract_ave=vol_fract_ave+cell2mat(vol_fract(i));
end
vol_fract_ave=vol_fract_ave./no_ss;

i=1;
figure(i)
set(gcf,'Color',[1 1 1])
set(gcf, 'Units','centimeters', 'Position',[10 10 12 7])
box on
hold on

n=10 ; % number of total data markers in the curve graph

for i=1:length(cn)

M_n = round(linspace(1,numel(data_vtk{cn(i)}.vol_fract_ave(:,2)),n)); %
indices of markers

p1(i)=plot(data_vtk{cn(i)}.vol_fract_ave(:,2),data_vtk{cn(i)}.vol_fract_ave(:,1),'color',plotprop{cn(i)});
p1(i)=plot(data_vtk{cn(i)}.vol_fract_ave(M_n,2),data_vtk{cn(i)}.vol_fract_ave(M_n,1),mark{i},'color',plotprop{cn(i)},'markersize',5);
p1(i)=plot(data_vtk{cn(i)}.vol_fract_ave(M_n(1),2),data_vtk{cn(i)}.vol_fract_ave(M_n(1),1),'color',plotprop{cn(i)},'marker',mark{i},'markersize',5);
);

```

```
end

xlabel('\phi [-
]$', 'interpreter', 'latex', 'FontName', 'Times', 'fontsize', fontSizeLabel)
ylabel('$h
[m]$', 'interpreter', 'latex', 'FontName', 'Times', 'fontsize', fontSizeLabel)
leg1=legend(p1,list,'FontName','Times','fontsize',fontSizeLeg,'Location',
'SouthWest');
legend 'boxoff'
%axis([0 1.2 0 220])
Ticks = 0:0.05:0.45;
set(gca, 'XTickMode', 'manual', 'XTick', Ticks, 'xlim', [0,0.45]);
Ticks = 0:0.05:0.3;
set(gca, 'XTickMode', 'manual', 'YTick', Ticks, 'ylim', [0,0.3]);
%axis 'auto x'
pa=[0.1700    0.1500    0.750    0.790];
set(gca, 'position',pa)
export_fig(['void.tiff'],'-tif','-r600','-nocrop')
hold off

anim_void(ss_start,ss_stop,1,10,data_vtk,plotprop,cn,1)
```

10 Appendix B – Experiment

The experiment set up consist of an electrodynamic shaker, an acceleration sensor, dynamic scales and a high speed camera used for the height measurement. The single parts are described as follows. The connecting and controlling of the shaker and the sensor was accomplished using data acquisition modules from *National Instruments*® and the software *LabVIEW*® described in Section 10.4..

10.1 Particles

For the experiment glass beads of the sort of *SiLiBeads S* from Sigmund Linder GmbH with a declared range of the particle diameter between 1 and 1.3 [mm] are used. To have an exact knowledge and also to keep the simulation as precise as possible the particle size distribution of these glass beads is needed. Therefore the device *Sympatec QicPic*, using an image evaluation method, is used. The gained data was filtered with the criteria to only take into account particles with an aspect ratio higher than 0.8 to sort out images of overlapping particles. The final volume distribution is shown in Figure 34.

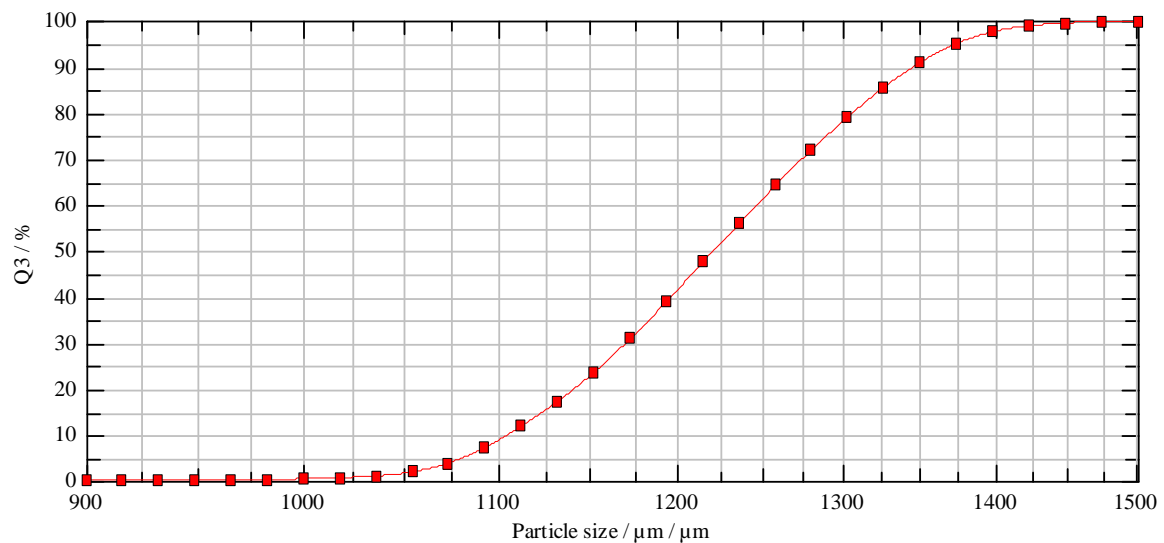


Figure 34: Particle volume distribution of SiLiBeads S d=1 to 1.3 mm

For the simulation five particle classes are defined resembling the gained particle distribution. The mean diameters of the classes are calculated as weighted average of fractions of the volume based distributions. The measured particle distribution and the five defined particle classes are shown in the table below. The mean particle diameter is 1.22 [mm].

Measured Distribution				Defined 5 Classes	
x_o	x_m	$Q_3(x_o)$	$\Delta Q_3(x_o)$	x_m	$\Delta Q_3(x_o)$
[μm]	[μm]	-	-	[μm]	-
915.99	908.00	0.05	0.05		
932.27	924.13	0.08	0.03		
948.84	940.56	0.11	0.03		
965.70	957.27	0.18	0.07		
982.86	974.28	0.28	0.10	1060.57	7.36
1000.33	991.60	0.44	0.16		
1018.10	1009.22	0.70	0.26		
1036.20	1027.15	1.10	0.40		
1054.61	1045.41	2.00	0.90		
1073.35	1063.98	3.96	1.96		
1092.43	1082.89	7.36	3.40		
1111.84	1102.14	12.01	4.65		
1131.60	1121.72	17.44	5.43		
1151.71	1141.66	23.73	6.29	1135.62	23.71
1172.17	1161.94	31.07	7.34		
1193.00	1182.59	39.13	8.06		
1214.20	1203.60	47.70	8.57		
1235.78	1224.99	56.05	8.35	1214.63	33.27
1257.74	1246.76	64.34	8.29		
1280.09	1268.92	72.09	7.75		
1302.84	1291.47	79.21	7.12		
1325.99	1314.42	85.66	6.45	1299.81	26.71
1349.56	1337.78	91.05	5.39		
1373.54	1361.55	95.12	4.07		
1397.95	1385.75	97.66	2.54		
1422.79	1410.37	98.92	1.26	1386.07	8.95
1448.08	1435.44	99.52	0.60		
1473.81	1460.95	99.83	0.31		
1500.00	1486.91	100.00	0.17		

Table 5: measured particle size distribution and definition of 5 classes for simulations

10.2 Bin Design

The bin is made out of transparent PMMA to make easy visual investigations possible. The bin has a square base area with a side length of 30 [mm] and a height of 300 [mm]. The front of the bin can be changed to allow the usage of outlet designs. The basic front bears a cylindrical outlet with a diameter of 10 [mm] and an outlet length of 15 [mm] (considering the material thickness it ends up in 23 [mm] outlet length in total). A design drawing can be seen in Figure 35.

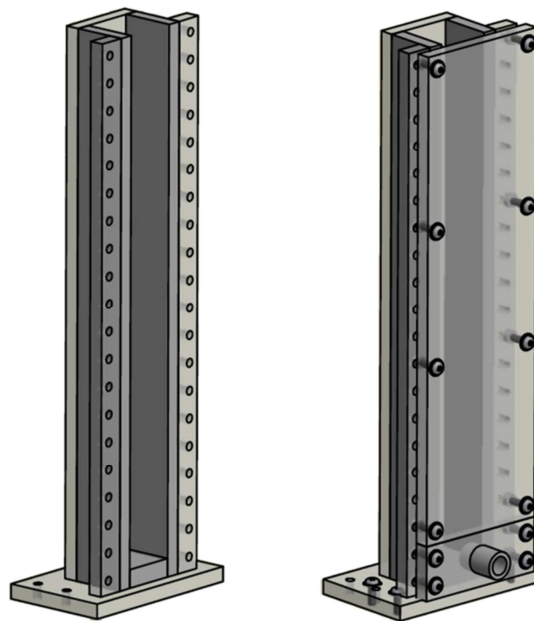


Figure 35: Design drawing of the bin without (left panel) and with (right panel) mounted front and orifice.

10.3 Shaker, Accelerometer and Scales

As shaker the *Vibration Test System TV51120* is used. The system consists of an electrical amplifier, a cooling blower and a vibration exciter. The technical data sheet is presented in Figure 38. A *NI 9263* analog output module provides the excitation current which gets amplified by the amplifier which powers finally the shaker. The shaker is attached on a 20[kg] heavy base plate (see Figure 36 a). To shield the surroundings from the shaker's vibrations, rubber puffs are mounted between the base plate and the shaker.

As accelerometer the *Seika BDK 100* is used. Before usage the sensor was calibrated at the Institute of Lightweight Design by Dipl.-Ing. Dr.techn. Thomas Thurner. The calibration value for the sensitivity of the sensor is 15.88 [mV/g]. The data sheet of the sensor is presented in Figure 38. The sensor is powered by a 5 [V] constant voltage source and the signal acquisition is done by an *NI 9234* high accuracy analog input module specifically

designed for high-channel-count vibration applications. The accelerometer is mounted on the shaker (see Figure 36 a) giving the possibility of controlling the acceleration of the shaker via a feedback loop (Figure 37).

The dynamic scales consist of the load cell *HBM PW22C3* and a self-constructed casing out of aluminum and PMMA. The data acquisition is accomplished by using a RJ50 adapter and a *NI 9237* bridge module. The assembled scales can be seen in Figure 36 b) and the data sheet of the load cell can be viewed in Figure 40.

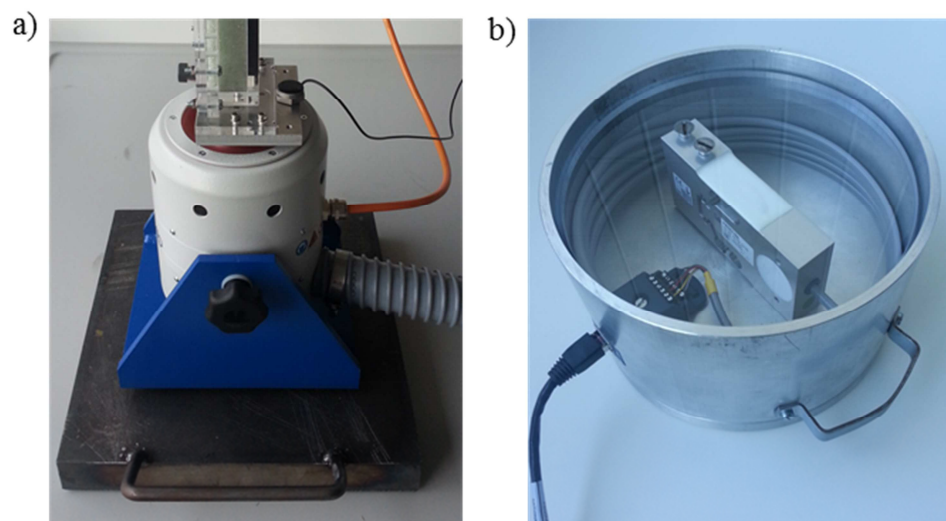


Figure 36: a) Shaker with accelerometer mounted to base plate;
b) Assembled scales including load cell, RJ50 connector and casing

For controlling the experiment, a *LabVIEW*® program was designed (see Section 10.4). An overview of the data acquisition devices and electronic schematic is shown in Figure 37.

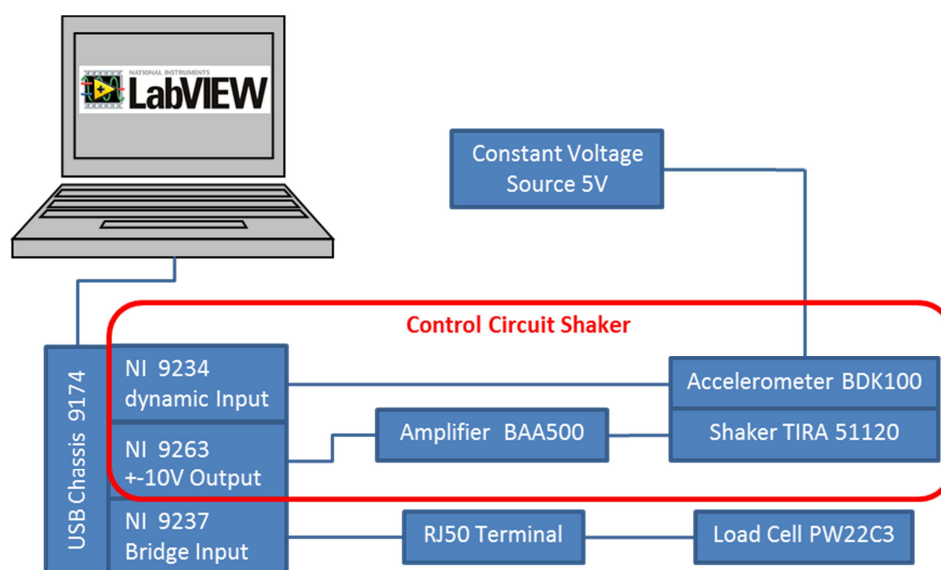


Figure 37: Electronic Schematic

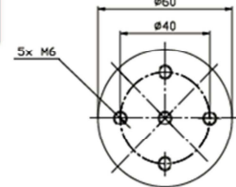
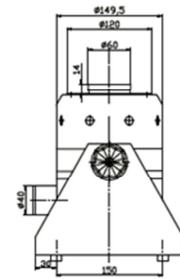
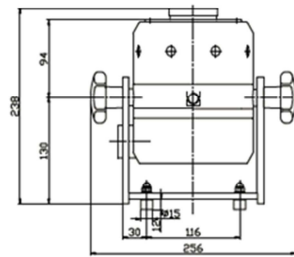


Vibration Test System TV 51120

S 51120 (Example drawing) Dimensions in mm

TECHNICAL PARAMETERS Vibration exciter S 51120

Rated peak force $Sine_{rms}/Random_{rms}$	200/140 N
Frequency range	2-7000 Hz
Main resonance frequency	>6500 Hz
Max. displacement Peak-Peak	13 mm
Max. velocity Sine/Random	1.5/1.5 m/s
Max. acceleration Sine/Random	89/62 g
Suspension stiffness	8 N/mm
Effective moving mass	0.23 kg
Max. weight tested	3 kg
Weight	12 kg
Armature diameter	60 mm



SCOPE OF DELIVERY, OPTIONS AND FEATURES OF THE SYSTEM

<p>Scope of delivery: Vibration exciter 200 N Swivel frame Power amplifier 500 VA Cooling blower Connection cable (3 m) Power cable amplifier (1.5 m) Blower hose \varnothing40 mm (3 m)</p>	<p>Options: Rack for mounting the amplifier Remote control (Hardware) Silencer for cooling blower (Noise reduction up to 5 dB(A)) Acoustic enclosure for cooling blower (Noise reduction 15 - 23 dB(A)) Cable extension Factory acceptance test</p>	<p>Features: Vibration isolation Coarse filter unit Automatic centering of the armature High cross-axial stiffness Light weight construction by using rare earth magnet Minimum maintenance effort Made in Germany Servicehotline</p>
---	--	--

TECHNICAL PARAMETERS Amplifier BAA 500

Output power _{max}	500 VA
Frequency range	DC - 20 kHz
Voltage-/Current mode	yes/yes
Voltage _{max} , max	45 V
Current _{max} , max	11.2 A
Load resistance, opt.	4 Ohm
Signal input voltage _{max}	< 5 V
Distortion	< 0.1 %
Signal to noise ratio	> 90 dB
Weight	25 kg
Dimensions (WxHxD)	483 x 90 x 450 mm
Power supply (Standard)	1- / N / PE 230 V \pm 5% 50 Hz, CEE 7/7
Recommended fuse protection (Standard)	16 A slow
Max. power consumption at 230 V	0.35 kVA
Interlocks:	Overload, temperature, clipping and more
Features:	High Signal to noise ratio of >90 dB

TECHNICAL PARAMETERS Cooling blower TB 0080

Volume flow rate	max. 80 m ³ /h
Total pressure difference	max. 120 hPa
Power	0.37 kW
Frequency	50 Hz
Hose diameter	40 mm
Hose length (Std.)	3 m
Weight	10 kg
Dimensions (WxHxD)	246 x 256 x 247 mm
Sound pressure level, max.	max. 53 dB(A)
Power supply (standard)	1- / N / PE 230 V \pm 5% 50 Hz, CEE 7/7
Max. power consumption at 230 V	0.46 kVA
Options:	
Silencer TB 0080-SI (Noise reduction up to 5 dB(A))	Dimensions (LxD): 310 x 65 mm Weight: 0.2 kg
Acoustic enclosure TB 0080-AE (Noise reduction 15 - 23 dB(A))	Dimensions (WxHxD): 795 x 841 x 699 mm Weight: 45 kg Hose length according to customers request (up to 10 m)

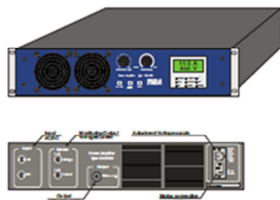


Figure 38: Data sheet TIRA 51120 (http://www.tira-gmbh.de/schwing/bilder/produkte/schw_er/9n_440n/system_tv_51120_eng.pdf, 2014.05.03)

seika.de[®] **BDK3, BDk10, BDk100**



Accelerometers of high overload resistance with integrated electronics for dynamic measurement of vibration and acceleration in the frequency range 1Hz to several kHz

Features

- very high overload resistance
- insensitive to interference by magnetic and electric fields
- multiple housing options
- light weight
- linear frequency response with little or no resonant peak at upper cut-off frequency
- low non-linearity
- small lower cut-off frequency
- high signal-to-noise ratio
- hermetically sealed
- low transverse sensitivity
- high long-term stability
- integrated sensor electronics
- low output impedance
- long connection lines possible

Description

The dynamic accelerometers BDk3, BDk10, and BDk100 are capacitive spring-mass accelerometers with integrated sensor electronics. Resonant peaks are minimized by dynamic gas damping in the primary transformer. The sensor electronics require only minimal power and are in conjunction with the capacitive primary transformer characterized by low error and high long-term stability.

Application

The accelerometers BDk3, BDk10 and BDk100 are used for applications requiring high overload resistance, high long-term stability, small lower cut-off frequency, light weight and low power consumption. Typical applications include:

- measurements on vehicles, machinery, buildings and plants for process control and error diagnosis
- seismic measurements
- vibration measurements
- safety engineering
- dynamic measurement of position and velocity

Technical Specifications

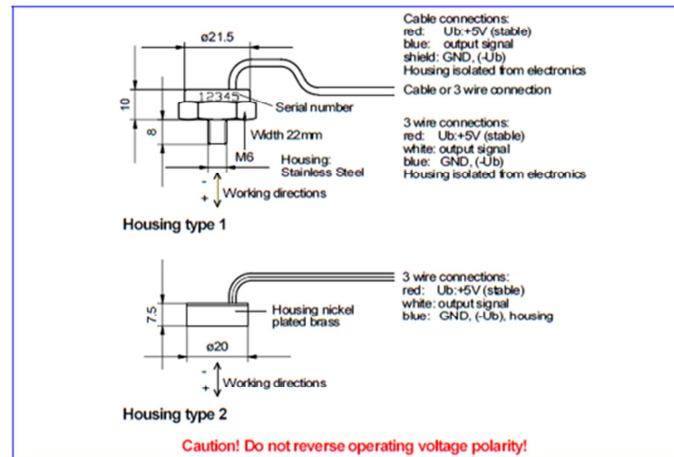
Type	BDk3	BDk10	BDk100
Measuring range	±3g (ca. ±30m/s ²)	±10g (ca. ±100m/s ²)	±100g (ca. ±1000m/s ²)
Resolution	<10 ⁻³ g	<5·10 ⁻³ g	<5·10 ⁻² g
Frequency range	1...300Hz	1...800Hz	1...1500Hz
Sensitivity at U _b = 5Volt	appr. 150mV/g	appr. 60mV/g	appr. 15mV/g
Temperature drift of sensitivity	<+6·10 ⁻² % / K		
Temperature drift of zero point	<0.1mV/K		
Zero offset	(2.5±0.1)Volt - generally: 0.5U _b ±4%		
Output impedance	approx. 100 Ohm		
Linearity deviation	<1%		

SEIKA Mikrosystemtechnik GmbH - Eilharter Str.10 - D-87435 Kempten - Tel: 0831-25532 Fax: 0831-25534
 Internet: <http://www.seika.de> - <http://www.seika.net> - Email: seika@seika.de

Transverse sensitivity	<1%
Mechanical overload resistance in direction of measurement	approx. 10 000g (appr. 100 000m/s ²) !
Nominal supply voltage (regulated)	U _{BN} = 5Volt
Permissible supply voltage range	U _{BE} = 2V ... 16V
Current drawn at U _b = 5V	approx. 2mA
Degree of protection	IP65
Operating temperature	-40°C ... +85°C
Storage temperature	-45°C ... +90°C
Weight in stainless steel housing with thread without cable	approx. 17Gramm
Weight in small housing without cable	approx. 7Gramm
Standard electrical connection	3 highly flexible, color-coded wires ø1mm length approx. 18 cm (special lengths on request)
Alternative electrical connection for sensors in stainless steel housing	0.5m strong, flexible, shielded cable, 2 wires + shield, ø2.1mm (special lengths on request)

on request: Special design for very low power consumption up to 30µA

Dimensions (in mm) and Connections



SEIKA Mikrosystemtechnik GmbH - Eilharter Str.10 - D-87435 Kempten - Tel: 0831-25532 Fax: 0831-25534
 Internet: <http://www.seika.de> - <http://www.seika.net> - Email: seika@seika.de

Figure 39: Data sheet accelerometer BDk 100
 (http://www.seika.de/english/pdf_e/BD_e.pdf, 2014.03.12)

PW22C3

Single point load cells

Data Sheet



Special features

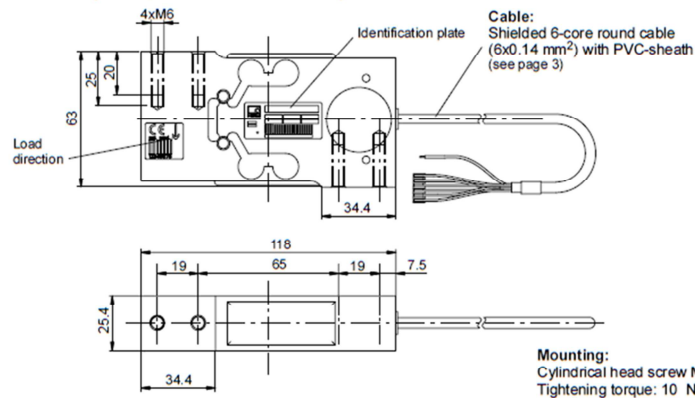
- High overload limits with integrated overload protection (Patent pending)
- High torsional and bending stiffness
- OIML-R60 certificate
- Degree of protection IP 67
- Fast Settling time
- optimized for dynamic weighing applications

Optional:

- Protection housing
- Different cable lengths



Dimensions (in mm; 1 mm= 0.03937 inches)



Specifications

Type	PW22...				
Accuracy class ¹⁾	C3MR				
Maximum number of load cell intervals (n _{LC})	3000				
Maximum capacity (E _{max})	kg	6	10	20	30
Minimum LC verification interval (v _{min})	g	0.5	1	2	2
Max. platform size	mm	400 x 400			
Sensitivity (C _n)	mV/V	1.9 ± 0.1			
Zero signal (without pre load)	mV/V	0 ± 0.1			
Temperature effect on zero balance (TK ₀)	% of C _n / 10 K	± 0.0117	± 0.0140	± 0.0140	± 0.0093
Temperature effect on sensitivity (TK _C) ²⁾ in the temperature range +20 ... +40 °C -10 ... +20 °C	% of C _n / 10 K	± 0.0175 ± 0.0117			
Relative reversibility error (d _{ry}) ²⁾		± 0.0166			
Linearity deviation (d _{lin}) ²⁾		± 0.0166			
Ratio of minimum dead load output return (DR)	% of C _n	± 0.0166			
Off-center load error ³⁾		± 0.0233			
Input resistance (R _{LC})	Ω	300...500			
Output resistance (R ₀)		300...500			
Reference excitation voltage (U _{ref})	V	5			
Nominal range of excitation voltage	V	1...12			
Max. excitation voltage (B _U)	V	15			
Isolation resistance (R _{is}) at 100 V _{DC}	GΩ	> 1			
Nominal (rated) range of ambient temperature (B _T)	°C [°F]	-10 ... +40 [14 ... 104]			
Operating temperature range (B _{tu})		-20 ... +50 [-4 ... 122]			
Storage temperature range (B _g)		-25 ... +70 [-13 ... 158]			
Limit load (E _L) at 120 mm eccentricity		150			
Lateral load limit (E _{lq}), static	% of E _{max}	> 300			
Permissible dyn. load (F _{adm}): with max. 50 mm eccentricity		70			
Breaking load (E _d) at 20 mm eccentricity		500			
Nominal (rated) displacement at E _{max} (s _{nom}), approx.	mm	< 0.15			
Resonance frequency, without load, approx.	Hz	280	380	540	660
Weight (G), approx.	kg	0.5			
Degree of protection acc. to EN 60 529 (IEC 529)		IP67			
Material:		Aluminum Silicone rubber PVC			

¹⁾ According to OIMLR60 with P_{LC} = 0.7
²⁾ The values for linearity deviation (d_{lin}), relative reversibility error (d_{ry}) and temperature effect on sensitivity (TK_C) are recommended values. The sum of these values remain within the cumulated error limit acc. to OIML R60.
³⁾ Loaded with 30 % of the max. capacity at 142 mm eccentricity (acc. to OIML R76).

B1558-1.0 en



Figure 40: Data sheet load cell PW22C3
 (<http://www.hbm.com/fileadmin/mediapool/hbmdoc/technical/b1558.pdf>, 2014.07.07)

10.4 LabVIEW Program

The *LabVIEW*® program is based on the principle of the queued message handler combined with an event handler which allows interaction with various devices over a front panel and observes the actions being taken. Figure 41 gives an overview over the program structure while in Figure 42 the interaction front panel is shown.

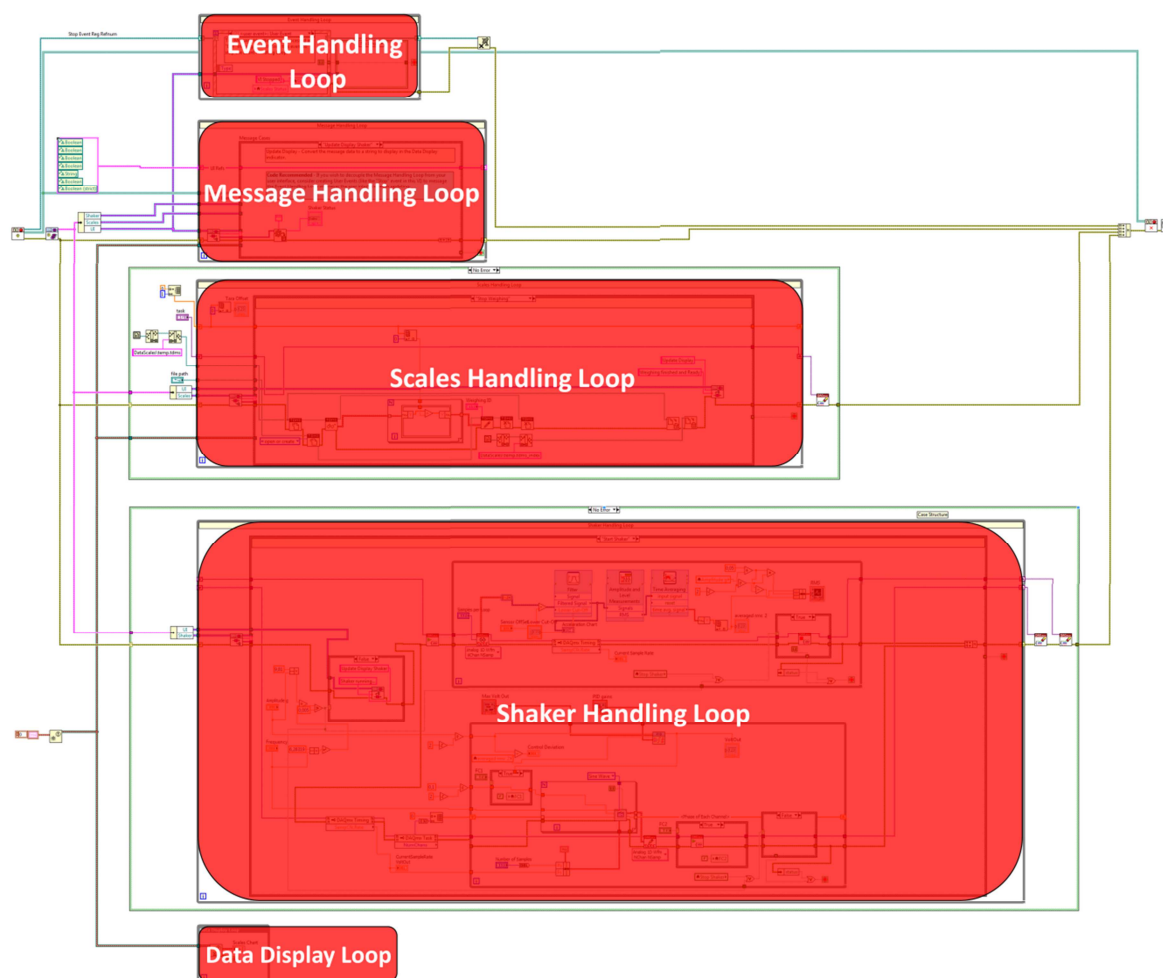


Figure 41: Block Diagram LabVIEW Program

If a button is pressed in the front panel, this causes a reaction in the event handling loop by sending a message to the message handling loop which directs then tasks to the different device loops. The message handling loop also sends status messages back to the front panel. Finally acquired data is sent back to the front panel via the data display loop.

The front or control terminal in Figure 42 allows adjusting settings and controlling the experiment. The load cell configuration (i.e. calibration, sample frequency...) is defined via *NIMAX* (Measurement and Automation Explorer) and can be selected at task in the scales tab. The sample frequency is set to a value of 2000 [Hz]. Via the selective file path, the logging

file can be named and its path set. With the weighing ID several data acquisitions can be recorded in one logging file and later easily distinguished. The data gets saved in a .tdms file which can be easily post processed with Matlab. In the scales chart the current acquired data can be viewed.

In the shaker control tab one can set beside the amplitude and the frequency also various settings of the excitation, the accelerometer and the control circuit. In the sensor settings the accelerometer's sensitivity and offset can be adjusted and the acceleration data can be saved as before in a .tdms file. The acceleration chart is showing the current acceleration data. In the excitation settings the PID controller elements can be defined. As it turned out a value of 0.1 to 0.4 for the P-element in combination with a value of 0.01 to 0.1 for the I-element and 0 for the D-element gives the best controlling results. The controller uses the root mean square (RMS) of the acceleration signal. The RMS chart shows the current RMS-signal and the accelerometers range of accuracy. The maximum voltage output should not exceed 2.5 [V] since it is the input limit of the amplifier. The lower cut off is a frequency value for applying a low bass filter during the experiment to get rid of noise and other disturbances. The sample rate is kept at 1000 [Hz] for the excitation and sensor giving accuracy and good performance of the data acquisition.

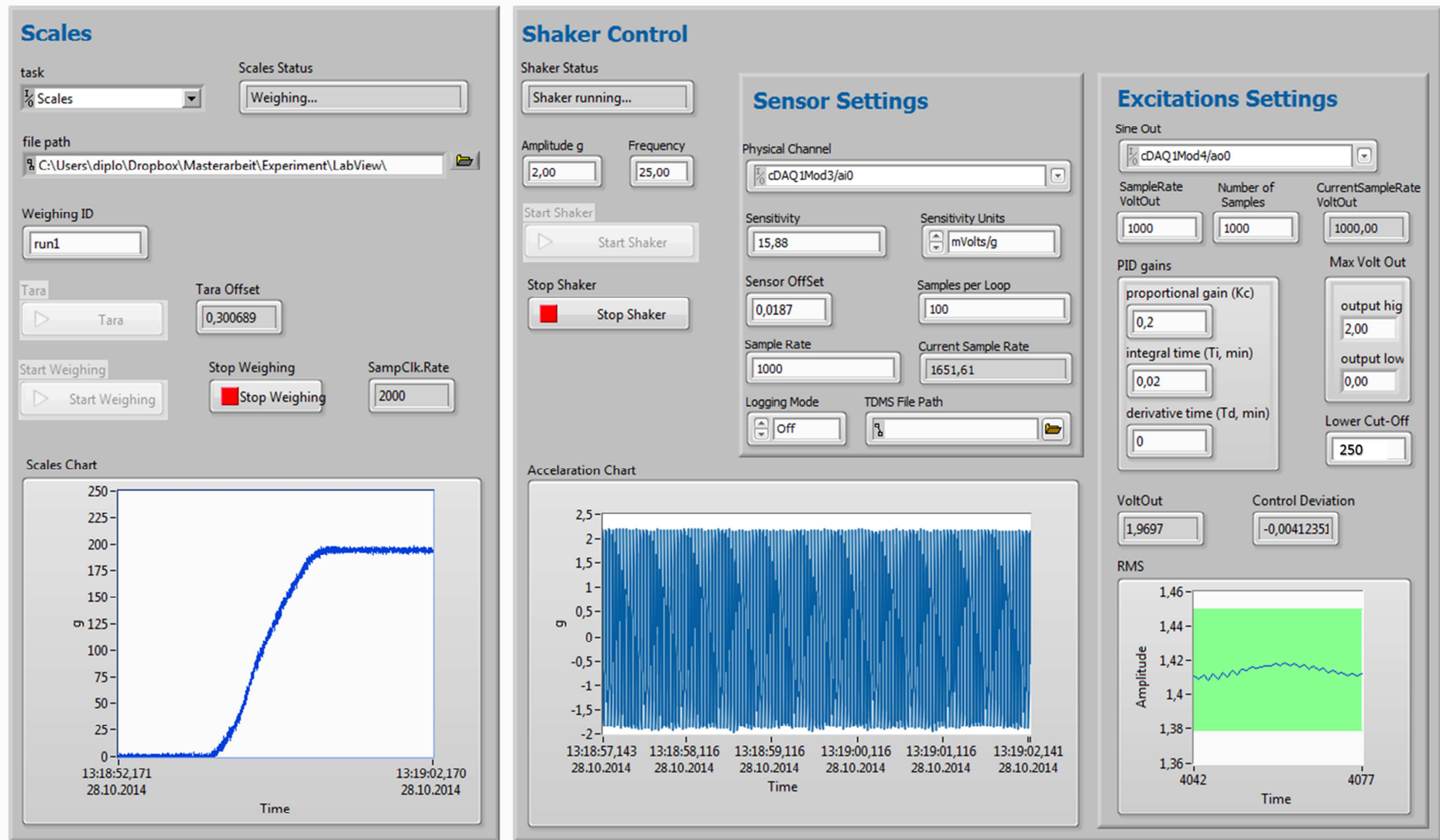


Figure 42: Control Terminal of LabVIEW Program for Controlling of the Experiment

10.5 Height Measurement

The high speed camera *MotionScope M3*® was used for the height measurement. For discharge analyses, meaning capturing the whole bin, a lens with a focal length of 35 [mm] was chosen. For the analyses of the bed expansions, where only the region of top layer was captured, a lens with a focal length of 50 [mm] was in usage. With the software *MotionStudio*® the camera was controlled and picture acquisition was setup and done. To have a good balance between amount of data and accuracy, a capture frequency of 60 [Hz] was applied for the discharge experiments and 200 [Hz] for bed expansion analyses. For the calibration a picture of a black stripe with a defined length of a withe section was taken. In the post processing a pixel to [m] ratio was calculated out of this calibration picture.

10.6 Setup and Performing Experiments

Pictures of the final setup with all devices can be seen in Figure 43.

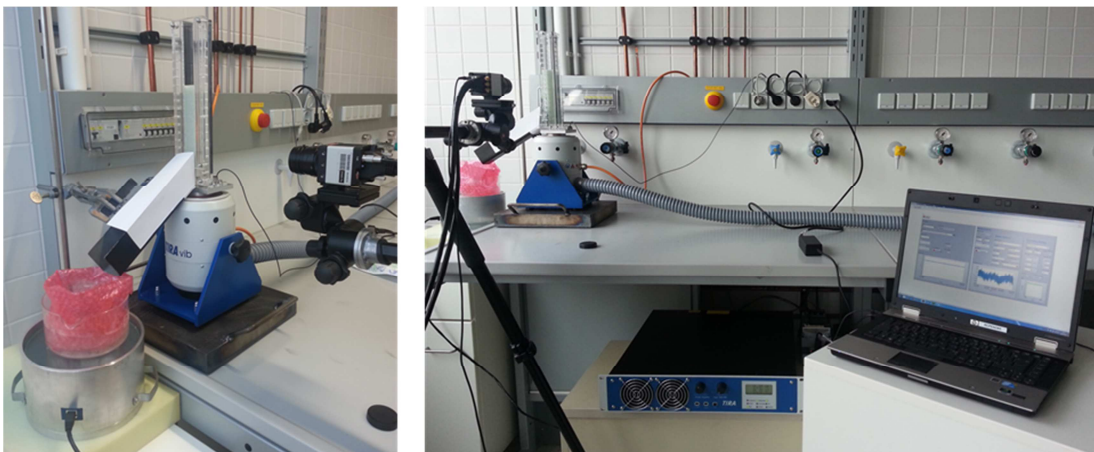


Figure 43: Experimental setup.

To move the particles from the bin outlet to the scales a narrow, smooth and steep chute is used with the attempt not to distort the particle flow too much.

The scales are put on a different desk to encapsulate it from the shaker's oscillations. However, even by using foam materials for active dampening the shaker's oscillation are still impressed on the scales' signal. Therefore later smoothing and filtering in the post processing is required.

The execution of the experiment works as follows:

- The bin gets closed with an stubble and filled with a certain amount of particles (for instance 250 [gr] for the usual experiment)
- The amplitude and frequency gets defined in the *LabVIEW*® program, the shaker started and with the gain potentiometer of the amplifier put to the required amplification to reach the sought amplitude
- Then start the scales (after taring) and camera data acquisition and remove the stubble of the shaking bin. The data of the different devices get aligned later in the post processing, so the acquisition has not to start simultaneously
- Take care that due to the decreasing mass on the shaker the shaking acceleration is kept in certain limits to get resembling results (otherwise adjust the PID controller elements)

10.7 Post Processing of Experimental Data

In a first step the scales data, stored in a .tdms file, and the pictures of the high speed camera are processed with a *Matlab*® program. First the scales data gets imported with the *Matlab*® function `convertTDMS.m`¹. Then a length/pixel ratio is calculated from the calibration picture and applied during the importing of the pictures, ending up in the height development data of each experiment. This raw data of mass and height gets filtered (i.e. to smooth out the signal of vibrations in balance data and to smooth out bed oscillations in height data), trimmed to the start of the experiment and finally aligned because of the different sampling frequencies to get one consistent set of data per run of each experiment. Finally an averaged data set is calculated and stored together with the data of each run in one *Matlab*® file for later investigations and comparisons. The *Matlab*® program is shown as follows.

```
% ***** Graz University of Technology *****
% copyright: Gerald Reif, 2014.8.21.

% DESCRIPTION: Imports scales data from tdms files, extract height data
of pictures and assembles them in one file
%
% Input: Hz.....frequency shaker
%        g.....amplitude shaker
%        capture_freque....frequency of capturing pictures
%        logging_freque....frequency of logging weighing data
%
% Output: structure of collected and transformed data
```

¹ <http://www.mathworks.com/matlabcentral/fileexchange/44206-converttdms--v10->, 2014.07.26

```

clear all
close all
clc

%input
capture_frequ=60;
logging_frequ=2000;
Hz=100;
g=16;

%% Creating and Import
experiment = [num2str(Hz) 'Hz_' num2str(g) 'g'];
tdms=convertTDMS(false); %read tdms
NoRuns=length(dir('run*'));

%% Mass Data
rawdata.ID=[];
rawdata.massdata=[];
rawdata.heightdata=[];

rawdata(1).ID='run1/Waage';
rawdata(2).ID='run2/Waage';
rawdata(3).ID='run3/Waage';

% write to rawdata
for j=1:length(rawdata)
for i=1:length(tdms.Data.MeasuredData)
    if strcmp(rawdata(j).ID,tdms.Data.MeasuredData(i).Name)
        rawdata(j).massdata.time=(0:1/logging_frequ:...
            (length(tdms.Data.MeasuredData(i).Data)-1)/logging_frequ).';
        rawdata(j).massdata.mass=tdms.Data.MeasuredData(i).Data;
    end
end
end

clear tdms

%% Height Data

for i=1:NoRuns
cd(['run' num2str(i)])
files=dir('*.tif');
n= length(files)-1; %number of pictures

%-----cm/Pixel Calibration-----
cal_stripe_length=0.05; %m
% files(end).name
A=imread(files(end).name); %read image
tresh_calc_cali=graythresh(A); %treshhold for particle indication
A=A(1:end,1:end,1:end); %Bildausschnitt
B=im2bw(A,tresh_calc_cali); %convert to black(0)/white(1) considering
threshold
B_mean=mean(B, 2); %calculate mean b/w value for each height
for k=1:length(B_mean)
    if B_mean(k)>0.5 %find calibrations stripe start
        cal_start=k;
        for l=k:1:length(B_mean)
            if B_mean(l)<0.5 %find filling height
                cal_end=l;
            end
        end
    end
end

```

```

        cal_pixel_length=cal_end-cal_start;
        rawdata(i).cal_ratio=cal_stripe_length/(cal_pixel_length);
        break
    end
end
break
end
end
end

%%check calibration
% figure
% imshow(B)
% hold on
% plot(0:100,cal_start,'r')
% plot(0:100,cal_end,'r')

clear cal_start cal_end cal_pixel_length cal_stripe_length

%-----Height Analysis-----
for j=1:n

A=imread(files(j).name); %read image
tresh_calc(j)=graythresh(A); %treshhold for particle indication
A=A(1:end,1:end,1:end); %Bildausschnitt
B=im2bw(A,tresh_calc(1)); %convert to black(0)/white(1) considering
threshold
B_mean=mean(B, 2); %calculate mean b/w value for each height
C{j}=B; %Save each pic for review reasons
temp_time{i}(j)=(j-1)*1/capture_frequ;
for k=length(B_mean):-1:1 %find bottom

    if B_mean(k)>0.5 %find first particle layer if more than half of the
pixels are white
        part_bottom(j)=k;
        for l=1:k
            if B_mean(1:l+5)>0.5 %if next five layers are also filled with
particles -> filling height
                temp_height{i}(j)=(k-l)*rawdata(i).cal_ratio;
                break
            end
        end
        break
    end
    temp_height{i}(j)=0;
end

end

rawdata(i).heightdata.time=temp_time{i}.'; %saving time and height
rawdata(i).heightdata.height=temp_height{i}.';
cd ../

end

clear A B B_mean i j k l n temp_time temp_height thresh files %C

%% Data processing

for i=1:NoRuns
% find discharge start of mass data

```

```

temp2{i}=smooth(smooth(rawdata(i).massdata.mass,0.01,'loess'),logging_frequ);
diff_mass{i}=diff(temp2{i});
for j=logging_frequ*2:length(diff_mass{i})-logging_frequ/20
    if diff_mass{i}(j:j+logging_frequ/20)>1E-6
        start_disch_m(i)=j;
        break
    end
end

% find discharge start of height data
temp_height2{i}=smooth(smooth(rawdata(i).heightdata.height,0.01,'loess'),capture_frequ);
diff_height{i}=diff(temp_height2{i});
for j=capture_frequ*2:length(diff_height{i})-capture_frequ
    start_disch(i)=1;
    if diff_height{i}(j:j+capture_frequ)<-5E-5 %Check start for each Exp.
        start_disch(i)=j;
        break
    end
end

% find discharge stop: stop=if height data drops below 30mm
for j=capture_frequ*2:length(temp_height2{i})
    if temp_height2{i}(j)<=0.03
        stop_disch(i)=j;
        break
    end
end

runtime_h(i)=stop_disch(i)-start_disch(i);

stop_disch_m(i)=ceil(start_disch_m(i)+runtime_h(i)/capture_frequ*logging_frequ);

runtime_m(i)=stop_disch_m(i)-start_disch_m(i);

%smoothe and write mass data to data_processed
data_processed(i).ID=rawdata(i).ID;
data_processed(i).time=rawdata(i).massdata.time(1:max(runtime_m(i))+1);
%cut data to discharge time
data_processed(i).mass=temp2{i}(start_disch_m(i):start_disch_m(i)+max(runtime_m(i)));
data_processed(i).runtime=(stop_disch_m(i)-start_disch_m(i))/logging_frequ;

% cut height rawdata
rawdata(i).cutheightdata.time=rawdata(i).heightdata.time(1:max(runtime_h(i))+1);
rawdata(i).cutheightdata.height=temp_height2{i}(start_disch(i):stop_disch(i));

k2=1;
%align height data to mass data
for j=1:length(rawdata(i).cutheightdata.time)
    for k=k2:length(data_processed(i).time)
        if rawdata(i).cutheightdata.time(j)<=data_processed(i).time(k)
            temp_height{i}(k,1)=rawdata(i).cutheightdata.height(j);

```

```

        k2=k;
        break
    end
end
end
end

%fill height data set
for j=1:length(temp_height{i})
    if temp_height{i}(j)==0
        point1=temp_height{i}(j-1);
        for k=j:length(temp_height{i})
            if temp_height{i}(k)>0
                point2=temp_height{i}(k);
                delta_height=(point1-point2)/(k-j+1);
                while temp_height{i}(j)==0
                    temp_height{i}(j)=temp_height{i}(j-1)-delta_height;
                    j=j+1;
                end
            end
        end
    end
end
end
end

data_processed(i).height=temp_height{i};
end

%% runtime and curve averaging

if NoRuns >= 2

    min_length=length(data_processed(1).time);

    for i=2:NoRuns
        if length(data_processed(i).time)<min_length
            min_length=length(data_processed(i).time);
        end
    end

    A=data_processed(1).mass(1:min_length);
    for i=2:NoRuns
        A=A+data_processed(i).mass(1:min_length);
    end
    A=A./(i);
    i=i+1;
    data_processed(i).ID='averaged_data';
    data_processed(i).time=data_processed(1).time(1:min_length);
    data_processed(i).mass=A;
    clear A

    rt_temp=data_processed(1).runtime;
    for i=2:NoRuns
        rt_temp=rt_temp+data_processed(i).runtime;
    end
    rt_temp=rt_temp/i;
    i=i+1;
    data_processed(i).runtime=rt_temp;

    A=data_processed(1).height(1:min_length);
    for i=2:NoRuns

```

```

        A=A+data_processed(i).height(1:min_length);
end
A=A./(i);
i=i+1;
data_processed(i).ID='averaged_data';
data_processed(i).time=data_processed(1).time(1:min_length);
data_processed(i).height=A;

clear A

end

%% Write to file
save(experiment,'data_processed')

%% Show acquired data for checking

plotprop=['b','r','c','k'];

i=1
figure (i)
hold on
plot(rawdata(1).massdata.time, rawdata(1).massdata.mass,'-c')
plot(data_processed(i).time+start_disch_m(i)/logging_freque,
(data_processed(i).mass),plotprop(i))
plot(rawdata(i).massdata.time(1:length(rawdata(i).massdata.time)-1),
diff_mass{i},plotprop(i))

i=2
figure (i)
hold on
plot(rawdata(2).massdata.time, rawdata(2).massdata.mass,'-m')
plot(data_processed(i).time+start_disch_m(i)/logging_freque,
(data_processed(i).mass),plotprop(i))
plot(rawdata(i).massdata.time(1:length(rawdata(i).massdata.time)-1),
diff_mass{i},plotprop(i))

i=3
figure (i)
hold on
plot(rawdata(3).massdata.time, rawdata(3).massdata.mass,'-b')
plot(data_processed(i).time+start_disch_m(i)/logging_freque,
(data_processed(i).mass),plotprop(i))
plot(rawdata(i).massdata.time(1:length(rawdata(i).massdata.time)-1),
diff_mass{i},plotprop(i))

i=4
figure (i)
hold on
for i=1:NoRuns
plot(rawdata(i).heightdata.time(1:length(rawdata(i).heightdata.time)-
1),diff_height{i},plotprop(i))
plot(rawdata(i).heightdata.time,rawdata(i).heightdata.height,plotprop(i))
plot(rawdata(i).heightdata.time,temp_height2{i},plotprop(i))
end

i=6
figure (i)
hold on

```

```

for i=1:NoRuns
plot(data_processed(i).time, data_processed(i).mass,plotprop(i))
end

i=7
figure (i)
hold on
for i=1:NoRuns
plot(data_processed(i).time(1:length(data_processed(i).height)),data_proc
essed(i).height,plotprop(i))
end

```

The raw data with their filtered curves of one of the experiments at 50 [Hz] and 8 [g] can be seen in Figure 44. Note that the fitted mass curve is already cut to the desired analyzing range.

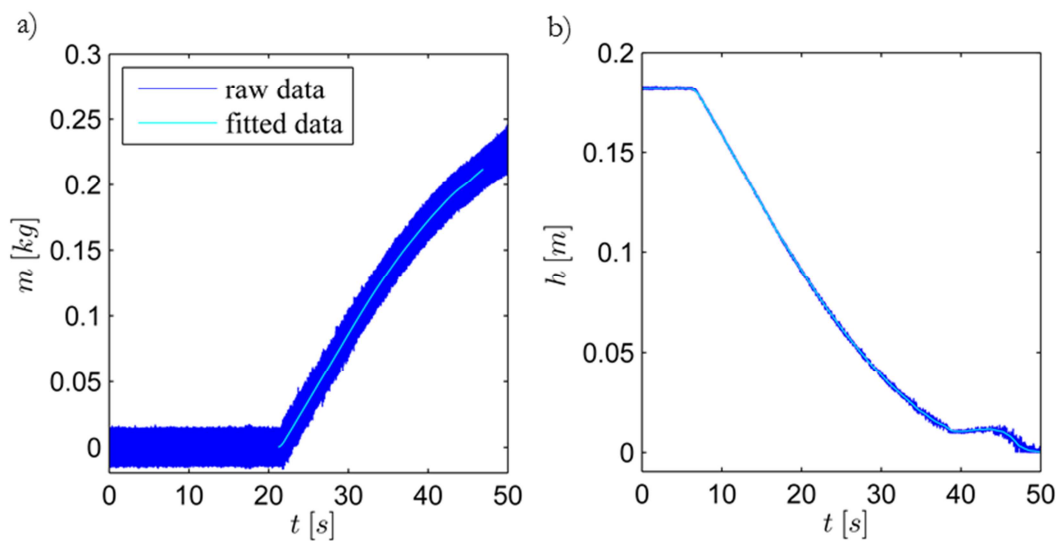


Figure 44: Raw data of experiment 8 [g] 50 [Hz]: a) mass data, b) height data

The data sets of the experiments are getting compared to one another in a different *Matlab*[®] program. For the mass and height data, confidence intervals are calculated. For the comparison of the discharge of the experiments the dimensionless discharge rate *Tor* as described in Section 3 is calculated. To quantify the value of fluidization and the stability of Torricelli behavior error calculations are performed and stored in a .txt file. The *Matlab*[®] code can be viewed in the following section.

```

% ***** Graz University of Technology *****
% copyright: Gerald Reif, 2014.8.29.

% DESCRIPTION: processes experimental dat
%
% Input: Matlab data files of experiments
% Output: graphs of mass, height and discharge rate development
%

```

```

clear all
close all
clc

exp_ids={'25Hz_4g','25Hz_5g','25Hz_6g','25Hz_7g','25Hz_8g'};
% exp_ids={'50Hz_6g','50Hz_8g','50Hz_10g','50Hz_12g','50Hz_14g'};
% exp_ids={'75Hz_8g','75Hz_10g','75Hz_12g','75Hz_14g','75Hz_16g'};
% exp_ids={'100Hz_8g','100Hz_10g','100Hz_12g','100Hz_14g','100Hz_16g'};

fig_str='25Hz';

plot_origin2=1; %!...plot dimensionles data
expo_fig=1; %!...export figures
write_data=1; %!...write Torricelli data to file

% Output string
for i=1:length(exp_ids)
list{i}=strrep(exp_ids{i},'_',' ');
export_data(i).ID=strrep(exp_ids{i},'_',' ');
end

%import data
for i=1:length(exp_ids)
exp{i}=load(exp_ids{i});
end

%% torrichelli fit
for i=1:length(exp_ids)
A=0.01.^2*pi/4; %outlet area
A_base=0.03.^2; %base area
h0(i)=exp{i}.data_processed(end).height(1); %starting height

rho(i)=0.25/(0.03*0.03*h0(i));

h=exp{i}.data_processed(end).height;
runtime_tor=(sqrt(h(end))-sqrt(h0(i)))./(-sqrt(9.81./2).*A./A_base);

t2=linspace(0,max(runtime_tor),length(exp{i}.data_processed(end).mass));
h2=(-sqrt(9.81./2).*A./A_base.*t2+sqrt(h0(i))).^2;
m2=h0(i).*A_base*rho(i)-h2.*A_base*rho(i);

torri_2{i}=(diff(exp{i}.data_processed(end).mass)./diff(exp{i}.data_proce
ssed(end).time))./(diff(m2)./diff(t2));

% check torri data via another approach
m_p_2_2{i}=(sqrt(2*9.81*exp{i}.data_processed(end).height)*0.01^2*pi()/4*
rho(i));
torri_2_2{i}=(diff(exp{i}.data_processed(end).mass)./diff(exp{i}.data_pro
cessed(end).time))./(m_p_2_2{i}(1:end-1));

%error calculation
for j=1:length(h2)
if h2(j)/h2(1)<=0.9
for k=j:length(h2)
if h2(k)/h2(1)<=0.2
lin_fit{i}=mean(torri_2{i}(j:k));
a=(torri_2{i}(j:k)-lin_fit{i}).^2;
absolut error
abs_error_tor{i}=mean(abs(torri_2{i}(j:k)-lin_fit{i})); %mean

```

```

        rel_lin_error{i}= abs_error_tor{i}/lin_fit{i}; %mean relative
linear error
        Tor_MaxMin{i}= (max(torri_2{i}(j:k))-min(torri_2{i}(j:k))); %
max min range
        break
        end
        end
        break
        end
end

export_data(i).meanTorricelli=lin_fit{i};
export_data(i).TorMinMax=Tor_MaxMin{i};
export_data(i).rellinError=rel_lin_error{i};
export_data(i).absError=abs_error_tor{i};
end

%% confidence intervalls

% t=4.303; %P=0,95 zweiseitig; =0.975 einseitig; n=2
t=6.965; %P=0,98 zweiseitig; =0.99 einseitig; n=2
n=3; %trails per experiment

% confidence intervall mass
for i=1:length(exp_ids)
n=length(exp{i}.data_processed)-1;
leng1=length(exp{i}.data_processed(end).mass);
sum1=0;
for j=1:n
sum1=sum1+(exp{i}.data_processed(j).mass(1:leng1)-
exp{i}.data_processed(end).mass).^2;
end
s{i}=sqrt(1/(n-1).*sum1);
Konf_m_high{i}=exp{i}.data_processed(end).mass+t.*s{i}/sqrt(n);
Konf_m_low{i}=exp{i}.data_processed(end).mass-t.*s{i}/sqrt(n);
Konf_m_e{i}=t.*s{i}/sqrt(n);
Konf_m_e2{i}=t.*s{i}/(sqrt(n)*exp{i}.data_processed(end).mass(end));
end

% confidence intervall height
for i=1:length(exp_ids)
n=length(exp{i}.data_processed)-1;
leng1=length(exp{i}.data_processed(end).height);
sum1=0;
for j=1:n
sum1=sum1+(exp{i}.data_processed(j).height(1:leng1)-
exp{i}.data_processed(end).height).^2;
end
s{i}=sqrt(1/(n-1).*sum1);
Konf_h_high{i}=exp{i}.data_processed(end).height+t.*s{i}/sqrt(n);
Konf_h_low{i}=exp{i}.data_processed(end).height-t.*s{i}/sqrt(n);
Konf_h_e{i}=t.*s{i}/sqrt(n);
Konf_h_e2{i}=t.*s{i}/(sqrt(n)*exp{i}.data_processed(end).height(1));
end

%% plotting
plotprop=[[1 0 0];[0 0 1];[0 0.25 0];[1 0 1];[0 1 1];[0 1 0];...
[1 0.1 0];[0.5 0.8 0.8];[0.5 1 0.6];[0.9 0.3 0.9];...
[0.6 0.1 0];[1 0.5 0];[0 0.2 0.5];[0.5 0.3 0];...]

```

```

        [0.6 1 1];[0.9 1 0.7];[0.8 0.4 0.6];[0.7 0.4 1];[0.8 0.4
0.6];[0.7 0.4 1]];
mark={'o','s','d','^','v','x','o','s','d','^','v','x','o','s','d','^','v'
,'x','o','s','d'};
fontSizeTitle=12;
fontSizeAxis=12;
fontSizeLeg=11;
fontSizeLabel=11;
markerSize = 9;
lineWidth=1;
mfc='w';
end_time=35;

%% plot: mass over time
if plot_origin2==1

i=1;
figure(i)
set(gcf,'Color',[1 1 1])
set(gcf, 'Units','centimeters', 'Position',[10 13 8 7])
box on
hold on

n=10 ; % number of total data markers in the curve graph

for i=1:length(exp_ids)
M_n = round(linspace(1,numel(exp{i}.data_processed(end).height),n)); %
indices of markers

norm_mass=exp{1, i}.data_processed(end).mass(end);

p1(i)=plot(exp{1, i}.data_processed(end).time,exp{1,
i}.data_processed(end).mass./norm_mass,'color',plotprop(i,:));
p1(i)=plot(exp{1, i}.data_processed(end).time(M_n),exp{1,
i}.data_processed(end).mass(M_n)./norm_mass,mark{i},'color',plotprop(i,:)
,'markersize',5,'MarkerFaceColor',mfc);
p1(i)=plot(exp{1, i}.data_processed(end).time(M_n(1)),exp{1,
i}.data_processed(end).mass(M_n(1))./norm_mass,'color',plotprop(i,:),'mar
ker',mark{i},'markersize',5,'MarkerFaceColor',mfc);

for j=1:n
    errorbar(exp{1, i}.data_processed(end).time(M_n(j)),exp{1,
i}.data_processed(end).mass(M_n(j))./norm_mass,Konf_m_e2{i}(M_n(j)),Konf_
m_e2{i}(M_n(j)),'color',plotprop(i,:))
end
end

xlabel('${t}
[s]','$','interpreter','latex','FontName','Times','fontsize',fontSizeLabel)
ylabel('${m} [-
]','$','interpreter','latex','FontName','Times','fontsize',fontSizeLabel)
% legend 'boxoff'
axis([0 35 0 220])
Ticks = 0:5:end_time;
set(gca, 'XTickMode', 'manual', 'XTick', Ticks);
Ticks = 0:0.1:1;
set(gca, 'XTickMode', 'manual', 'YTick', Ticks, 'ylim', [0,1.02]);
axis 'auto x'
pa=[0.220    0.160    0.730    0.780];

```

```

set(gca, 'position',pa)
xlabh = get(gca,'XLabel');
set(xlabh,'Position',get(xlabh,'Position') - [0 .003 0]);
if expo_fig==1
export_fig([ fig_str '_4mass_norm.tiff'],'-tif','-r600','-nocrop')
end
hold off

%% plot: height over time
i=2;
figure(i)
set(gcf,'Color',[1 1 1])
set(gcf, 'Units','centimeters', 'Position',[20 13 8 7])
box on
hold on

n=10 ; % number of total data markers in the curve graph

for i=1:length(exp_ids)
M_n = round(linspace(1,numel(exp{i}.data_processed(end).height),n));

p2(i)=plot(exp{1, i}.data_processed(end).time,exp{1,
i}.data_processed(end).height./exp{1,
i}.data_processed(end).height(1),'color',plotprop(i,:));
p2(i)=plot(exp{1, i}.data_processed(end).time(M_n),exp{1,
i}.data_processed(end).height(M_n)./exp{1,
i}.data_processed(end).height(1),mark{i},'color',plotprop(i,:),'markersize
e',5,'MarkerFaceColor',mfc);

p2(i)=plot(exp{1, i}.data_processed(end).time(M_n(1)),exp{1,
i}.data_processed(end).height(M_n(1))./exp{1,
i}.data_processed(end).height(1),'color',plotprop(i,:),'marker',mark{i},'
markersize',5,'MarkerFaceColor',mfc);

for j=1:n
errorbar(exp{1, i}.data_processed(end).time(M_n(j)),exp{1,
i}.data_processed(end).height(M_n(j))./exp{1,
i}.data_processed(end).height(1),Konf_h_e2{i}(M_n(j)),Konf_h_e2{i}(M_n(j)
),'color',plotprop(i,:))
end
end

xlabel('${t}
[s]$', 'interpreter','latex','FontName','Times','fontSize',fontSizeLabel)
ylabel('${h}
[-]$', 'interpreter','latex','FontName','Times','fontSize',fontSizeLabel)
Ticks = 0.1:0.1:1;
set(gca, 'XTickMode', 'manual', 'YTick', Ticks, 'ylim', [0.1,1.02]);
Ticks = 0:5:end_time;
set(gca, 'XTickMode', 'manual', 'XTick', Ticks);
axis 'auto x'
pa=[0.220 0.160 0.730 0.780];
set(gca, 'position',pa)
xlabh = get(gca,'XLabel');
set(xlabh,'Position',get(xlabh,'Position') - [0 .003 0]);
if expo_fig==1
export_fig([ fig_str '_5height_norm.tiff'],'-tif','-r600','-nocrop')
end
hold off

```

```

%% plot: torri vs height
i=3;
figure(i)
set(gcf, 'Color',[1 1 1])
set(gcf, 'Units','centimeters', 'Position',[10 4 8 7])
box on
hold on

n=10 ; % number of total data markers in the curve graph

for i=1:length(exp_ids)
M_n = round(linspace(1,numel(torri_2{i}),n));

p8(i)=plot(exp{1, i}.data_processed(end).height(1:end-1)./exp{1,
i}.data_processed(end).height(1),torri_2_2{i}, 'color',plotprop(i,:));
p8(i)=plot(exp{1, i}.data_processed(end).height(M_n)./exp{1,
i}.data_processed(end).height(1),torri_2_2{i}(M_n),mark{i}, 'color',plotpr
op(i,:), 'markersize',5, 'MarkerFaceColor',mfc);
p8(i)=plot(exp{1, i}.data_processed(end).height(M_n(1))./exp{1,
i}.data_processed(end).height(1),torri_2_2{i}(M_n(1)), 'color',plotprop(i,
:), 'marker',mark{i}, 'markersize',5, 'MarkerFaceColor',mfc);
end

xlabel('${h}
[-]$', 'interpreter', 'latex', 'FontName', 'Times', 'fontsize',fontSizeLabel)
ylabel('${Tor} \ \ \
[-]$', 'interpreter', 'latex', 'FontName', 'Times', 'fontsize',fontSizeLabel)
Ticks = 0.2:0.1:0.90;
set(gca, 'XTickMode', 'manual', 'XTick', Ticks, 'xlim', [0.2,0.9]);
Ticks = 0.055:0.005:0.12;
set(gca, 'YTickMode', 'manual', 'YTick', Ticks, 'ylim', [0.055,0.09]);
pa=[0.220    0.1600    0.73    0.7800];
set(gca, 'position',pa)
xlabh = get(gca, 'XLabel');
set(xlabh, 'Position',get(xlabh, 'Position') - [0 .0002 0]);
if expo_fig==1
export_fig([fig_str '_6TorriVsHeight_norm.tiff'], '-tif', '-r600', '-
nocrop')
end
hold off

%% 2: Extract Legend vertical
i=4;
figure(i)
set(gcf, 'Color',[1 1 1])
set(gcf, 'Units','centimeters', 'Position',[20 4 3.5 7])
box on
hold on

for i=1:length(exp_ids)
p10(i)=plot(exp{1, i}.data_processed(end).height(M_n(1))./exp{1,
i}.data_processed(end).height(1),torri_2{i}(M_n(1)));
end

leg6=legend(p10,list, 'FontName', 'Times', 'fontsize',fontSizeLeg, 'Location'
, 'Eastoutside');
Ticks = 0.2:0.1:0.9;
set(gca, 'XTickMode', 'manual', 'XTick', Ticks, 'xlim', [0.2,1]);
Ticks = 0.0:0.01:0.1;

```

```
set(gca, 'YTickMode', 'manual', 'YTick', Ticks, 'ylim', [0.04,0.09]);
pa=[-0.55  0.2  .5  .7000];
set(gca, 'position',pa)
xlabh = get(gca,'XLabel');
set(xlabh,'Position',get(xlabh,'Position') - [0 .0002 0]);
if expo_fig==1
export_fig([fig_str '_LegendV.tiff'],'-tif','-r600','-nocrop')
end
hold off
end

%% write error data to text file
if write_data==1

for i=1:length(exp_ids)
Case{i,:}=export_data(i).ID;
meanTorricelli(i,:)=(export_data(i).meanTorricelli);
rellinError(i,:)=(export_data(i).rellinError);
absError(i,:)=(export_data(i).absError);
TorMinMax(i,:)=(export_data(i).TorMinMax);
end

T=table(Case,meanTorricelli,rellinError,absError,TorMinMax);
writetable(T,'Torricelli_data.txt','Delimiter','\t')
end
```